

MASSIVE SINGLE STAR EVOLUTION WITH
MESA - END PRODUCTS IN DEPENDENCE
OF INITIAL CONDITIONS AND APPLIED
APPROXIMATIONS.

STERNENTWICKLUNG MASSEREICHER EINZELSTERNE
- ENDPRODUKTE IN ABHÄNGIGKEIT VON
ANFANGSBEDINGUNGEN UND VERWENDETEN
NÄHERUNGEN.

Masterarbeit

im Fachgebiet Astrophysik



vorgelegt von: Frederick Groth

Studienbereich: Astrophysik

Matrikelnummer: 12009193

Gutachter: Priv.-Doz. Dr. Joachim Puls

© 2020, München

Contents

List of Figures	v
1 Introduction	1
1.1 Outline	4
2 Physics of Massive Single Stars	5
2.1 Stellar Structure Equations	5
2.2 Convection	8
2.2.1 Mixing Length Theory	9
2.2.2 Semiconvection	11
2.2.3 Thermohaline Mixing	12
2.2.4 Overshooting	12
2.2.5 MLT++	14
2.3 Atmospheric Boundary Condition	15
2.4 Rotation	16
2.4.1 Changes of Structure Equations	17
2.4.2 Rotationally Induced Mixing	18
2.5 Magnetic Fields	23
2.6 Stellar Winds	25
2.6.1 Line Driven Mass Loss	25
2.6.2 Dust Driven Mass Loss	30
2.6.3 Mass Loss at Critical Rotation	31
2.6.4 Dutch Wind Scheme	32
3 Stellar Evolution and MESA	33
3.1 Main Sequence	33
3.2 Later Evolutionary Phases	35
3.2.1 Hertzsprung Gap	35

3.2.2	Helium Core Burning to Carbon Core Burning	35
3.2.3	Luminous Blue Variable Stars	36
3.2.4	Wolf-Rayet Stars	37
3.3	Important MESA Parameters	37
3.3.1	μ -Barrier	38
3.3.2	Undershooting Problem	39
3.3.3	Boundary Conditions	40
3.4	Comparison with Other Calculations	41
3.4.1	Comparison with Ekström et al. (2012)	42
3.4.2	Comparison with Brott et al. (2011)	46
3.4.3	Comparison between evolutionary tracks of Brott et al. (2011) and Ekström et al. (2011)	48
3.5	Remnant Linking	49
3.5.1	Explosion Types	49
3.5.2	Remnant Types	50
3.5.3	Woosley-Formalism	50
3.5.4	Belczynski-Formalism	52
3.5.5	Gravitational Mass	53
4	Evolutionary Model Grids	55
4.1	Physical Parameters	55
4.1.1	Standard Grid	55
4.1.2	Additional Grids	56
4.1.3	Abundances	56
4.2	Numerical Parameters	57
4.3	Technical Aspects	58
4.3.1	Runtime	58
4.3.2	RAM Usage	58
4.3.3	Final Storage	59
5	Evolutionary Tracks and Core Masses	61
5.1	Position of RSGs	61
5.2	Systematic Effects	63
5.2.1	Rotation and Magnetic Fields	64

5.2.2	Convective Boundary Criterion	69
5.3	Specific Effects	72
5.3.1	Metallicity	72
5.3.2	Overshooting	72
5.3.3	Mass loss	77
5.3.4	Mixing	79
6	Remnant Analysis	83
6.1	Remnant Masses	83
6.1.1	Remnant Masses at MW Metallicity	83
6.1.2	Comparison with Other Studies	85
6.1.3	Remnant Masses at Lower Metallicities	87
6.2	Remnant Types	89
6.3	Explosion types	93
6.4	Statistics for Microlensing	96
6.4.1	Constraining the IMF	98
6.4.2	Different Metallicities	100
7	Conclusion and Outlook	103
A	Massive Star Evolution with MESA – Set-Up and Technical Aspects	109
A.1	EOS, Opacities, Nuclear Reaction Rates	109
A.2	MESA setup	110
A.2.1	Installation and first steps	110
A.2.2	Starting our project	110
A.2.3	Visualisation and Troubleshooting	111
A.3	Settings for Our Calculations with MESA	111
A.3.1	Structure of Inlists	112
A.3.2	Setup and Execution	113
A.4	Inlists	114
A.4.1	Abundances	114
A.4.2	inlist_common	117
A.4.3	Phase-Specific	123

A.4.4	Different Grids	129
A.4.5	Adjustments for Avoiding Problems	131
A.5	Mass Loss	132
A.5.1	Hooks	132
A.5.2	Implicit Mass Loss at Critical Rotation	132
A.6	Runtime analysis	134
B	IDL	137
B.1	Analysis of a Single Model	137
B.2	Grid Analysis	138
	Bibliography	139
	Acknowledgements	155
	Eidesstattliche Erklärung	157

List of Figures

3.1	HRD μ barrier	38
3.2	Kippenhahn diagrams demonstrating the undershooting problem	40
3.3	HRD comparison boundary conditions	41
3.4	HRD comparison to Ekström et al. (2012)	43
3.5	HRD comparison to Ekström et al. (2012) including second bi-stability jump	44
3.6	HRD comparison to Ekström et al. (2012) with different timestep settings	44
3.7	Comparison of timesteps depending on the settings	45
3.8	HRD comparison of rotating models to Ekström et al. (2012)	46
3.9	HRD of non-rotating models, comparison to Brott et al. (2011)	47
3.10	HRD rotating models, comparison to Brott et al. (2011)	48
3.11	Woosley 2002 remnant linking	51
5.1	HRDs for models with MW abundance	62
5.2	HRDs for models with LMC abundance	63
5.3	HRDs for models with $Z = 10^{-5}$	64
5.4	Systematic differences in core and final masses at MW and LMC abundance	65
5.5	Systematic differences in core and final masses at $Z = 10^{-5}$	66
5.6	Surface Nitrogen Enrichment due to Rotation	67
5.7	Evolution of the angular velocity with and without magnetic fields	68
5.8	Internal run of rotation with and without magnetic fields	68
5.9	Evolution Ledoux vs Schwarzschild criterion	70
5.10	HRD for non-rotating $40M_{\odot}$ model with $Z = 10^{-5}$, comparison Ledoux vs Schwarzschild	71
5.11	Mass loss rates Ledoux vs Schwarzschild at $Z = 10^{-5}$	71
5.12	HRD for models with MW abundance	73
5.13	HRD for models with LMC abundance	74
5.14	HRD for models with $Z = 10^{-5}$	75
5.15	Differences in core and final masses between different overshooting values	76
5.16	Differences in core and final masses between different mass loss rates	78
5.17	HRDs for models with increased rotational mixing efficiency	80

5.18	Differences in core and final masses between different rotational mixing efficiencies	81
6.1	Remnant masses at MW metallicity	84
6.2	Remnant masses at MW metallicity, comparison rotation and mass loss	85
6.3	Comparison with Heger and Woosley (2002) with no overshooting .	86
6.4	Remnant masses at all metallicities	88
6.5	Remnant type depending on initial mass and metallicity by Heger et al. (2003)	90
6.6	Reproduction of Heger et al. (2003), Fig. 1	90
6.7	Reproduction of Heger et al. (2003) for current preferential model .	92
6.8	Explosion type depending on initial mass and metallicity by Heger et al. (2003)	94
6.9	Reproduction of Heger et al. (2003), Fig. 2	94
6.10	Reproduction of Heger et al. (2003) for current preferential model .	95
6.11	Ratio between mass included in compact remnants and visible mass, for single IMF	97
6.12	Ratio between mass included in compact remnants and visible mass, for different IMFs	99
6.13	As Fig. 6.12, but for different metallicities	101
A.1	Runtime analysis for a rotating ($\Omega = 0.4\Omega_{crit}$) $60M_{\odot}$ model	135

1 Introduction

Massive stars and their evolution are a highly discussed topic, relevant for many astrophysical fields. Characterised by strong radiation and stellar winds, they play a key role in the evolution of the interstellar medium. As a consequence of the recombination approximately 400,000 years after the big bang, the universe was opaque in a wide wavelength regime due to neutral hydrogen and helium. Very massive stars may have contributed to the re-ionisation of these elements some 100 Myr later, making it as transparent as it is today (Bromm, Kudritzki, and Loeb 2001, Tumlinson, Shull, and Venkatesan 2002). In addition, they are responsible for the enrichment with heavy elements. Elements up to iron are produced in their cores by nuclear reactions, brought up by mixing processes, and lost by their strong winds. Even heavier elements are produced and lost in the energetic supernova explosions at the end of their lifetimes. Only these elements allowed life on earth to come into existence. Finally, they can also trigger further star formation in their stellar neighbourhood (e.g., Esquivel and Raga 2007).

After the comparatively short time with pressure due to burning processes as a stabilizing agent, and the subsequent core collapse, only compact remnants are left over. As up to approximately 70% of the massive stars are located in binary systems (Sana et al. 2012), they may still cause further energetic events. In combination with a second, less evolved star, nova or supernova explosions can occur.

Different observational methods can be used to characterise the different evolutionary stages. As massive stars are very bright, their optical detection is possible even in other galaxies in our Local Group neighbourhood. Spectroscopy can reveal their surface properties and characteristics of their winds. Applying astroseismology, an insight into their inner structure is possible (Aerts 2019).

Their supernova explosions are so bright, that a detection in very far galaxies is possible. A new path for observations is gravitational wave analysis, which

might be used for a detection in even further galaxies. If two compact remnants are located closely together, they spiral inwards, merge together, and produce energetic gravitational waves. Recent observations have been able to reveal mergers of black holes (Abbott et al. 2016) and neutron stars (Abbott et al. 2017).

Finally, these compact remnants can lead to microlensing events, and thus are relevant in corresponding observations (Wambsganss 2006, Riffeser et al. 2006). For interpreting the number of observed events, reliable statistics of the compact final remnants is essential. Constraints on the initial mass function can be gained, when a trustworthy relation between initial and final masses is known. Such a formalism, though based on simplifying assumptions, has been provided by Renzini and Ciotti (1993). A more advanced description based on stellar evolution models was found by Heger and Woosley (2002) and Woosley, Heger, and Weaver (2002) for different metallicities.

Another path towards an improved understanding of massive stars, their structure, and evolution is to utilize theoretical models.

However, the physics of massive stars is affected by a variety of complex processes, which, until to date, are only partly understood. This includes internal processes, such as the treatment of convection, rotational instabilities, and angular momentum transport. Also the role of magnetic fields and the required precision of adopted mass loss rates (Puls, Vink, and Najarro 2008) is still unclear.

In mathematical terms, several coupled, linear and non linear differential equations have to be solved. Only a few estimates for typical variables have been found, but no complete solutions.

There exists a multitude of different stellar evolution codes aimed at solving structural processes and computing end states. As it is necessary to reduce computational costs, different simplifications have to be adopted, the most salient one being that the calculations are performed in one dimension.

For massive stars, the most commonly used stellar evolution codes are STERN (Brott et al. 2011), GENEC (Ekström et al. 2012), and MESA (Modules for Experiments in Stellar Astrophysics). The latter has been developed by Paxton et al. (2011, 2013, 2015, 2018, 2019). It is mainly designed to calculate stellar evolution for a wide range of masses, from very low up to very high mass stars, and through all evolutionary stages, from the pre main-sequence up to white dwarfs or to phases just before core collapse. However, it can also be used for a wide range of other problems such as stellar pulsations or the evolution of (irradiated) gas

planets.

A computation in three dimensions would require less approximations. Nevertheless, this is very time consuming, and there are only few multi-dimensional codes that only cover the short last phases or the explosion of stars (Fields and Couch 2020, Chen, Heger, and Almgren 2013, Chatzopoulos and Wheeler 2012). A currently used alternative is the 2d ESTER code (Gagnier et al. 2019)¹. It is intrinsically designed as a stellar structure code, but can mimic the evolution on the main sequence by consecutively increasing the central helium content. The second dimension is advantageous for the treatment of effects such as gravity darkening or rotation. However, turbulent motions still cannot be treated correctly. Due to the limited ability of following the evolution with this code, no study of the later phases is possible.

The aim of this thesis is to provide a relation for the end products in dependence of initial mass and metallicity, based on state-of-the-art physical assumptions and stellar models. As already described, such a relation can be utilized to interpret microlensing observations.

One major aspect of this study is to evaluate the impact of the above mentioned uncertainties, with respect to both evolution and progenitor structure. Following this philosophy, we want to investigate the possible range of remnant properties.

While single stars potentially undergo interactions with companions at earlier stages in their lives, the accompanying binary evolution entails even more parameters and considerations. To this end, we will focus on the evolution of single stars that evolve without any external influence and interaction. In the parallel thesis of Ferraro (2020), a more detailed analysis of the earlier evolution of binary stars on the main sequence (**MS**) is performed.

To obtain evolutionary paths and progenitor properties, we calculate stellar evolution models using MESA, because of several reasons discussed in the following.

As MESA is open source², and has a large number of contributors, there exists a wide range of state-of-the-art routines for numerics and physics. It provides a fully coupled solution of the set of differential equations calculated by the module `star`. Depending on the problem, different solvers are used, as described in Paxton et al. (2011). These are mainly Runge-Kutta integrators for differential equations and

¹Available online under <http://ester-project.github.io/ester/>

²Source-code online under <http://mesa.sourceforge.net/>

a Newton-Raphson solver for finding roots. A variety of settings can be used to adjust the numerical methods.

As for the numerics, also the assumptions about physics can be varied. Since MESA is open source, we can deduce all assumptions made directly from the code. Concluding, MESA is well suited for our study analysing the uncertainties.

We use MESA version 12115, together with the MESA software development kit (**SDK**) version 20190830, and calculate the evolution of massive stars in the range of $10 \dots 60 M_{\odot}$ with three different metallicities until central carbon exhaustion. From this point, the timescales are short, and the remnant properties can be concluded from the progenitor that has been calculated. We vary different parameters, in order to study the resulting uncertainties.

1.1 Outline

In Chpt. 2, we start with a summary of the most important physical processes within massive stars, the corresponding equations, and the uncertainties.

Subsequently, we present the main features of stellar evolution in Chpt. 3. Together with the physical theory, we discuss the impact of specific physical and numerical parameters in more detail. In addition, we compare the calculations carried out with different stellar evolution codes with analogous MESA calculations. Finally, the most important physical aspects of the explosions and remnants are summarised. Especially, two formalisms are provided that can be used to link the progenitor properties to the remnant.

In Chpt. 4, we discuss our grid of models in more detail. We present the relevant physical parameters chosen. The key technical aspects, such as runtime and required memory to run MESA simulations are provided.

The results of these calculations are analysed in Chpts. 5 and 6. In the former, we analyse the evolutionary tracks and core and final masses of the progenitor. The impact of various parameters is studied. In the latter, we discuss the corresponding remnant masses. We provide diagrams displaying the remnant and explosion type in dependence of initial mass and metallicity. Finally, specific diagrams required for the analysis of microlensing events are presented.

A summary of our main findings, and an outlook for possible future work are given in Chpt. 7.

In Apps. A and B we describe some of the MESA routines, our settings, and our analysis routines in more detail.

2 Physics of Massive Single Stars

A star is a massive, self-luminous, gravitationally bound object of ionised gas that emits radiation derived from internal fusion processes.

Already from this short description one can see that there are different processes that need to be understood to describe stars. This includes gravity, fusion processes, (magneto-)hydrodynamics, an equation of state as well as different transport processes.

As many stars are not separated objects but are located closely together in clusters or binary systems, even an interaction should be considered. However, dealing with these systems is beyond the scope of this thesis. We will focus on the physics and evolution of single stars. A more detailed discussion on binary stars with MESA has been provided by, e.g., Ferraro (2020).

In the following we want to give a short overview about the different physics required to describe stars. As argued in the previous chapter, different simplifications need to be applied to keep the computational effort in a reasonable range.

We start with a description of non-rotating stars. In a first order approximation, non-rotating stars can be assumed to have spherical shape and symmetry. In addition, we can assume that they are in a static situation. This is valid during all their life except some rapid phases of expansion or some unstable phases where dynamical terms have to be included.

2.1 Stellar Structure Equations

The most important physics can be condensed in five stellar structure equations. All these equations can be written in two different ways, depending on the independent variables chosen. In the Eulerian description, variables depend on the radius r , whereas they depend on the mass coordinate m in the Lagrangian

description. Conversion between these two forms can be obtained via

$$\partial m = 4\pi r^2 \rho \partial r, \quad (2.1)$$

$$\left. \frac{\partial}{\partial t} \right|_m = \frac{\partial}{\partial r} \left. \frac{\partial r}{\partial t} \right|_m + \left. \frac{\partial}{\partial t} \right|_r, \quad (2.2)$$

where ρ is the density and t the time.

The two basic equations for any fluid are the equation of continuity and the Navier-Stokes equation. A derivation of the equation of continuity can be found in Landau and Lifshitz (1987). It describes the mass conservation and can be written as

$$\frac{\partial \rho}{\partial t} + \nabla \cdot (\rho v) = 0 \quad (2.3)$$

with velocity v .

However, stars change only on long timescales. We can assume that they are in a static situation (see above). In combination with spherical symmetry, Eqn. (2.3) reduces to

$$\frac{dm}{dr} = 4\pi r^2 \rho, \quad (2.4a) \quad \frac{dr}{dm} = \frac{1}{4\pi r^2 \rho}. \quad (2.4b)$$

The momentum equation for a fluid was first formulated by Euler (1757).¹ The general form is

$$\frac{\partial v}{\partial t} + (v \cdot \nabla) v = -\frac{1}{\rho} \nabla P + g \quad (2.5)$$

where the first term on the rhs is the acceleration due to the gradient of the pressure P , and the second term g includes other accelerations, such as gravity. Again neglecting time dependencies, we obtain the condition for hydrostatic equilibrium

$$\frac{\partial P}{\partial r} = -\frac{Gm}{r^2} \rho, \quad (2.6a) \quad \frac{\partial P}{\partial m} = -\frac{Gm}{4\pi r^4}, \quad (2.6b)$$

with gravitational constant G . The pressure P includes all individual contributions such as gas and radiation pressure and also for instance neutrinos. For phases of rapid changes deviations from hydrostatic equilibrium can be considered, including

¹An alternative including viscous terms is the Navier-Stokes equation. As these can be neglected in stars, we only provide the simpler Euler equation.

an additional term for the acceleration a

$$\frac{\partial P}{\partial r} = -\frac{Gm}{r^2}\rho - a, \quad (2.7a) \quad \frac{\partial P}{\partial m} = -\frac{Gm}{4\pi r^4} - \frac{a}{4\pi r^2}. \quad (2.7b)$$

In addition to the mass also the energy has to be conserved. Different processes i with a power produced per gram ϵ_i combine to the total power l such that the energy conservation requires

$$\frac{\partial l}{\partial r} = 4\pi r^2 \rho \sum_i \epsilon_i, \quad (2.8a) \quad \frac{\partial l}{\partial m} = \sum_i \epsilon_i. \quad (2.8b)$$

There can be sources ($\epsilon > 0$) such as nuclear fusion reactions (ϵ_n) as well as sinks ($\epsilon < 0$) like neutrino losses (ϵ_ν). Gravitational work can act both as a source or sink depending on the situation.

Finally, there are different possibilities how the energy is transported. One alternative is that the energy is purely transported by photons. This is discussed further by Kippenhahn, Weigert, and Weiss (2012). Writing the transport equation as a diffusive process results in the flux

$$F = -\frac{4acT^3}{3} \frac{\partial T}{\kappa \rho \partial r} \quad (2.9)$$

where a is the radiation constant, c the speed of light, T the temperature and κ the local Rosseland mass absorption coefficient. The flux can also be written using the local luminosity $l = 4\pi r^2 F$. We can thus solve for the temperature gradient

$$\frac{\partial T}{\partial r} = -\frac{3}{16\pi ac} \frac{\kappa \rho}{r^2 T^3} l \quad (2.10a) \quad \frac{\partial T}{\partial m} = \frac{3}{64\pi^2 ac} \frac{\kappa}{r^4 T^3} l. \quad (2.10b)$$

The transport via convection and the condition(s) for when it needs to be considered will be discussed further in the next section. Anyhow, the temperature distribution can be found in a similar way

$$\frac{\partial T}{\partial r} = -\frac{T}{P} \frac{Gm\rho}{\pi r^2} \nabla_{ad}, \quad (2.11a) \quad \frac{\partial T}{\partial m} = -\frac{T}{P} \frac{Gm}{4\pi r^4} \nabla_{ad}, \quad (2.11b)$$

where $\nabla_{ad} = \left. \frac{\partial \ln T}{\partial \ln P} \right|_{ad}$ is the adiabatic temperature gradient. Actually, this is only an approximation as we will explain in the next section.

2.2 Convection

When boiling water in a water heater or on a hotplate, bubbles start to rise at some point. This effect is known as convection. But under which conditions does it occur?

Every part of the fluid undergoes small random displacements. As it immediately adjusts to the ambient pressure, the density changes. If the density of the rising bubble is larger than that of the surrounding medium, it sinks back. This situation is stable against convection. However, for a steeper ambient gradient, the bubble can have a lower density and thus continues to rise even faster.

For a quantitative analysis we have to compare the temperature gradient

$$\nabla = \frac{\partial \ln T}{\partial \ln P} \quad (2.12)$$

of the ambient medium to that of the perturbed bubble ∇_{int} . For chemically homogeneous situations this condition can be described by the Schwarzschild criterion

$$\nabla < \nabla_{int} \quad (2.13)$$

for stability.

If the medium has an inherent composition gradient, this can have a stabilising² effect. The condition for stability can be written as

$$\nabla < \nabla_L = \nabla_{int} + \frac{\phi}{\delta} \nabla_\mu \quad (2.14)$$

²For an ideal gas, $p_{gas} \sim \rho T / \mu$, such that $\delta > 0$, $\phi > 0$, only from the equation of state (**EOS**)! However, the total pressure includes radiation pressure, and a general EOS is more complicated. Looking at the composition term, this is indeed stabilising as for stars in most situations ρ , T , μ and P decrease outwards, such that $\frac{\phi}{\delta} \nabla_\mu > 0$

which is known as the Ledoux criterion. δ and ϕ are thermodynamic derivatives and ∇_μ the composition gradient

$$\delta = - \left(\frac{\partial \ln \rho}{\partial \ln T} \right)_{P, \mu} \quad (2.15)$$

$$\phi = \left(\frac{\partial \ln \rho}{\partial \ln \mu} \right)_{P, T} \quad (2.16)$$

$$\nabla_\mu = \left(\frac{\partial \ln \mu}{\partial \ln P} \right) \quad (2.17)$$

An alternative approach for deriving a stability criterion is by calculating the Brunt-Väisälä frequency N ,

$$N^2 = \frac{g}{\rho} (\nabla_T - \nabla), \quad (2.18)$$

the frequency of oscillations of a perturbed element being exposed to a gravitational acceleration g . If this is imaginary, the situation is unstable against convection. ∇_T is either ∇_{int} (Schwarzschild) or $\nabla_L = \nabla_{int} + \frac{\phi}{\delta} \nabla_\mu$ (Ledoux).

Both, the Ledoux and the Schwarzschild criterion, are used in various codes and calculations. In general we would prefer including the composition gradient. However, as both criteria are just approximations, it is unclear, which is the better description. The question could be answered only by full 3d hydrodynamic simulations.

If the medium is optically thick, no radiative losses are present, and the convection is called “efficient”. In this case, the internal gradient ∇_{int} of the bubble becomes the adiabatic one

$$\nabla_{ad} = \frac{P\delta}{C_P \rho T}, \quad (2.19)$$

where C_P is the specific heat at constant pressure, as stated, e.g., in Maeder (2009). The treatment of radiative losses will be discussed further in the next section.

In case efficient convection occurs, also the ambient gradient adjusts to the adiabatic one, $\nabla \rightarrow \nabla_{ad}$.

2.2.1 Mixing Length Theory

The mixing-length theory (**MLT**) was first formulated by Prandtl (1925). He suggests a simplified method to calculate convective mixing and energy transport.

A good summary of the assumptions is given by Mihalas (1978) and Salaris and Cassisi (2017).

Each convective bubble moves a typical distance λ before it releases its energy excess. This distance is expressed in terms of the local pressure scale height H_P as

$$\lambda = \alpha_{MLT} \cdot H_P, \quad (2.20)$$

$$H_P = P \left/ \frac{dP}{dr} \right. . \quad (2.21)$$

Typical values for α_{MLT} are on the order $\mathcal{O}(1)^3$. The MLT-Parameter has a huge impact on the evolution. In our calculations we use the calibrated value by Brott et al. (2011) of 1.5.

The convective flux can be calculated from the average velocity v_{conv} and the temperature excess $\overline{\Delta T}$

$$F_{conv} = C_P \overline{\Delta T} \rho v_{conv} \quad (2.22)$$

$$= \rho C_P T \left(\frac{g H_P}{32} \right)^{1/2} (\nabla - \nabla_{int})^{3/2} \alpha_{MLT}^2. \quad (2.23)$$

As the numerical factors (here $32^{-1/2}$) depend on the shape of the convective bubble, and specific averaging procedures applied in the calculation, they can be different from derivation to derivation.

The process of convection can be reformulated as a diffusion equation with diffusion coefficient

$$D_{conv} = \frac{\lambda}{3} \cdot v_{conv} \quad (2.24)$$

$$= \frac{\alpha_{MLT} H_P}{3} \cdot v_{conv} \quad (2.25)$$

As the timescale of convection $\tau = \frac{\lambda}{v_{conv}}$ is very short compared to the evolutionary timescales of the star⁴, convective mixing can be considered as instantaneous. The standard description MESA uses was formulated by Böhm-Vitense (1958)⁵. We choose a more recent alternative based on Mihalas (1978) including radiative losses.

These are important in outer stellar layers where the convective bubbles are not

³Calibrations using observations and stellar evolution codes range from $\alpha_{MLT} \approx 1 \dots 2$.

⁴ $\lambda \approx 0.1 R_\odot$, $v_{conv} \approx 4 \cdot 10^2$ cm/s during the main sequence, such that $\tau_{conv} \approx 0.5$ yr. This is short compared to the main sequence lifetime $\tau_{MS} \approx 10^6$ yr

⁵MESA parameter `MLT_option = 'ML1'`

optically thick.⁶ They lose some amount of their internal energy excess before dissolving into the ambient medium. The efficiency of convection is given by

$$\gamma = \frac{E_{transport}}{E_{lost}} \quad (2.26)$$

$$= \frac{K_{conv}}{2K_{rad}} \quad (2.27)$$

where the convective and radiative conductivity are

$$K_{conv} = \frac{4}{9} C_P \rho v_{conv} \lambda \quad (2.28)$$

$$K_{rad} = \frac{4acT^3}{3\kappa\rho}. \quad (2.29)$$

The implementation of inefficient convection in MESA is described in Paxton et al. (2013).

2.2.2 Semiconvection

During the main sequence, only the core becomes enriched by the produced helium such that the composition gradient $\nabla_\mu > 0$. In this case, every Schwarzschild stable region is also Ledoux stable. If a region is stable according to the Ledoux criterion but unstable according to Schwarzschild

$$\nabla_{int} < \nabla < \nabla_{int} + \frac{\phi}{\delta} \nabla_\mu, \quad (2.30)$$

semiconvection occurs.

The process of semiconvection can be understood in the following way: An upwards perturbed cell is denser (Ledoux stable) and sinks down again. In addition it is hotter (Schwarzschild unstable) and thus cools down due to radiative losses. It becomes denser and sinks down even further, oscillating around the initial position with increasing amplitude. The corresponding mixing efficiency is determined by the timescale of radiative cooling and less efficient than convection.

In MESA, semiconvection is implemented as a diffusive process as formulated by Langer, Fricke, and Sugimoto (1983) and Langer, El Eid, and Fricke (1985),

⁶Massive stars do not have a convective envelope on the main sequence. However, during later evolutionary phases, such an envelope can be present.

with diffusion coefficient

$$D_{semi} = \alpha_{semi} \cdot \frac{K_{rad}}{6C_p\rho} \cdot \frac{\nabla - \nabla_{ad}}{\nabla_L - \nabla}. \quad (2.31)$$

The coefficient α_{semi} is usually chosen as $\mathcal{O}(0.1 - 1)$ ⁷. In the limit $\alpha_{semi} = 0$ semiconvection recovers the pure Ledoux case. For very high values $\alpha_{semi} \gg 0$ we retain the Schwarzschild case.

2.2.3 Thermohaline Mixing

In more evolved stars shell burning can lead to an increase of heavier elements in outer regions and thus to a negative μ gradient. Another situation where negative μ gradients can occur are accreting binaries where processed material is deposited at the surface.

This μ gradient has a stabilising effect in the Ledoux case. The situation can be stable according to the Ledoux criterion but unstable according to Schwarzschild

$$\nabla_{int} > \nabla > \nabla_{int} + \frac{\phi}{\delta} \nabla_{\mu}. \quad (2.32)$$

Let us consider a downwards perturbed bubble. This should rise up again as it has a lower density. However, it is hotter and can sink down while cooling. The efficiency is again given by the cooling timescale. MESA uses the diffusion coefficient from Kippenhahn, Ruschenplatt, and Thomas (1980)

$$D_{thermo} = \alpha_{thermo} \frac{3K_{rad}}{2\rho C_p} \frac{\frac{\phi}{\delta} \nabla_{\mu}}{\nabla - \nabla_{ad}}. \quad (2.33)$$

2.2.4 Overshooting

A convective bubble does not stop immediately when reaching a stable region, but it still has a finite velocity. This phenomenon is known as overshooting.

A simple implementation is the “step overshooting”, expanding the convective region by a given fraction α_{over} of a pressure scale height. In this region the same diffusion coefficient as at the boundary of the convective zone is applied⁸.

⁷ $\alpha_{semi} = 0.1$ from Higgins and Vink (2020) $\alpha_{semi} = 1$ for Brott et al. (2011)

⁸As the diffusion coefficient $D_{conv} \rightarrow 0$ at the boundary of the convective zone, we cannot choose the coefficient at exactly this position. Instead, the value inside the convective zone, offset by a small amount $f_0 H_P$, has to be chosen. f_0 is typically on the order of $\mathcal{O}(0.01)$. The specific choice has no strong impact on the model.

An alternative and probably more physical approach is to apply an exponential decay of the diffusion coefficient D_0 at the boundary⁹

$$D = D_0 \exp\left(-\frac{2\Delta r}{f_{over} H_P}\right). \quad (2.34)$$

These two schemes give very similar results for $f_{over}^{(exp)} = \alpha_{over}^{(step)}/10$. However, for rotational effects included, there can be deviations between these two schemes.

The values for f_{over} or α_{over} have to be calibrated to match observations. Depending on the mass range and the calibration method, different authors find different values. In table 2.1 we give a summary of some values.

α_{over}	f_{over}	M_i/M_\odot (usage)	author
0		< 1.25	Ekström et al. (2012)
0.05		1.25 ... 1.5	
0.1		1.7 ... 120	
0.1		20 ... 60	Higgins and Vink (2020)
0.1 ... 0.2		7 ... 60	Martins and Palacios (2013)
	0.0175 ... 0.02	6.15 ... 6.27	Wu and Li (2019)
	0.01/0.03 0/0.002#	9 ... 40	Yoshida et al. (2019)
0.15*		30	Li, Chen, and Chen (2019)
0.2		0.8 ... 120	Schaller et al. (1992)
0.2*	0.016+	0.1 ... 300	Choi et al. (2016)
	0.02 ... 0.05	13	Wagle et al. (2019)
0.2 ... 0.35		9 ... 100	Schootemeijer et al. (2019)
0.335		5 ... 60	Brott et al. (2011)

* Equivalent step value, exponential scheme applied.

+ Envelope overshooting included with $f_{over} = 0.0174$.

Later evolutionary phases.

Table 2.1: Summary of different overshooting values

Claret and Torres (2019) and Castro et al. (2014) show that the overshooting value depends on the initial mass for low mass stars and high mass stars, respectively.

For us, particularly the result for high mass stars is important. While we adopt a value of $\alpha_{over} = 0.335$ for all stars, Castro et al. (2014) suggest, that the overshooting value should be even higher than that for stars more massive than $15M_\odot$.

⁹Again the value D_0 is taken at an offset f_0 inside the convective zone.

As most values are calibrated to fit the main sequence, there is only vague information for shell overshooting or later burning phases. In general, overshooting should be included in all regions, as shown by Li, Chen, and Chen (2019).

Implementation in MESA

MESA allows to set different overshooting parameters for different regions. The first distinction is made between core-overshooting, shell-overshooting, and shell-undershooting, meaning the extent of a convective shell below it in the same way as overshooting is calculated. A second subdivision is based on the burning process dominating inside these regions. Which type of burning a convective region is referred to is purely decided from the corresponding temperature range. Since the burning also depends on the density, this can only be understood as a first estimate.

As described above, overshooting should be present both in the core and the shell(s). As we will show in Sec. 3.3.2, MESA has difficulties when using all overshooting parameters with a value of 0.335 (Brott et al. 2011).

2.2.5 MLT++

As argued in Sec. 2.2.1, radiative losses are able to decrease the convection efficiency. In this case, the energy transport becomes mostly radiative. The star can get very close to the classical Eddington limit as $\Gamma_e \sim L_{rad}$.¹⁰ The proximity to the Eddington limit leads to an inflated envelope and density inversions for massive stars that evolve to a WR phase or a pseudo-WR phase (Poniatowski et al. 2012). However, since this process enforces very small timesteps, the model cannot converge within reasonable time.

The MESA module MLT++ allows to artificially reduce the superadiabaticity of the convective zone, thus increasing the convective efficiency. It thus decreases the energy transported by radiation, reduces the Eddington factor and avoids inflation. In this case, only the compact core of the WR star is calculated. As discussed by Paxton et al. (2013), and also obvious from our tests, MLT++ does not change the final results for the stellar structure.

An alternative to using MLT++ is either to calculate the full WR structure including the wind, which would be very time-consuming, or to use a consistent

¹⁰As discussed by Sundqvist (2020, priv. comm.) , this becomes important at the iron opacity bump at $T \approx 200$ kK.

hydrodynamic boundary condition instead of the hydrostatic one implemented in MESA.

2.3 Atmospheric Boundary Condition

The pressure at the atmospheric boundary does not vanish but has a finite value. As we will show in Sec. 3.3.3, the specific choice of this boundary condition can drastically affect the evolution. In the following, we want to give a short overview about the theory it is based on.

The atmospheric pressure in MESA is calculated using the approximations described in Cox and Giuli (1968), their Sec. 20.1. Unfortunately, there are two errors in their original calculation. Pavlovskii (2014)¹¹ was the first to identify these errors, and implemented a corrected formulation in MESA. In the following, we want to give a brief overview about the involved approximations and the corrected result.

In general, we can write the radiative pressure p_{rad} at optical depth τ as

$$p_{rad}(\tau) = \frac{F}{c}\tau + p_{rad}(\tau = 0) \quad (2.35)$$

where the flux F and p_{rad} are calculated using the intensity I ,

$$F \stackrel{\text{flux conservation}}{=} F(0) = 2\pi \int_0^1 I(0)\mu \, d\mu = \pi I(0), \quad (2.36)$$

$$p_{rad}(0) = \frac{2\pi}{c} \int_0^1 I(0)\mu^2 \, d\mu = \frac{2\pi}{3c} I(0). \quad (2.37)$$

Substituting these into Eqn. (2.35) yields

$$p_{rad} = \frac{F}{c}\tau + \frac{2}{3} \frac{F}{c}. \quad (2.38)$$

In addition, the integrated hydrostatic equilibrium yields, within their approximations

$$P = \tau \frac{g}{\kappa}. \quad (2.39)$$

¹¹MESA mailing-list archive, online under <https://lists.mesastar.org/pipermail/mesa-users/2014-May/003663.html>

Nevertheless, as Cox and Giuli (1968) already argue, this expression is missing the boundary contribution $p_{rad}(\tau = 0)$. Including the boundary contribution results in the total pressure in the outer stellar layers

$$P = \frac{\tau g}{\kappa} \left(1 + \frac{\kappa}{\tau g} \frac{2F}{3c} \right) \quad (2.40)$$

$$= \frac{\tau g}{\kappa} \left(1 + \frac{\kappa}{\tau} \frac{L}{6\pi cGM} \right). \quad (2.41)$$

At this point, Cox and Giuli (1968) obtained a different result, by evaluating only at $\tau = \frac{2}{3}$.¹² The second term inside the brackets corresponds to the radiation pressure at the boundary $\tau = 0$, which is often neglected.

In MESA, Eqn. (2.41) is implemented with an additional forefactor¹³. This can account for the uncertainty due to the approximations used, especially the assumption that the radiation field is isotropic even at $\tau = 0$.

In principle, a second correction term should be included, taking into account the pressure contribution of the wind. This can be neglected in almost all phases except if the wind is very thick.

2.4 Rotation

Rotation plays an important role in stellar evolution and corresponding calculations (Heger, Langer, and Woosley 2000, Maeder 2009, Meynet and Maeder 2017, Ekström et al. 2020). Stars do not need to rotate as a solid body, but show differential rotation and their rotation pattern can be quite complex. A reasonable assumption is the so-called “shellular rotation”: the angular frequency Ω is constant on isobars. This is ensured by strong horizontal turbulence (Zahn 1992).

There are various effects of rotation. At first, it changes the shape of the star and its symmetry. The assumption of spherical symmetry has to be replaced by a more advanced description. How this effects the stellar structure equations from

¹²In addition, their numerical expression in their footnote on p. 591 includes a wrong numerical factor. The correct expression is

$$P = \frac{\tau g}{\kappa} \left(1 + 7.64 \cdot 10^{-5} \frac{\kappa[\text{cgs}]}{\tau} \frac{2}{3} \frac{L/L_{\odot}}{M/M_{\odot}} \right). \quad (2.42)$$

¹³MESA parameter `Pextra_factor`, for `Pextra_factor < 0` the old, erroneous result is used.

Sec. 2.1 is discussed in Sec. 2.4.1. Moreover, it can drive several instabilities that are described in Sec. 2.4.2.

2.4.1 Changes of Structure Equations

The equations of stellar structure have to be adjusted, as first done by Meynet and Maeder (1997) based on the method of Kippenhahn and Thomas (1970). In the following we will provide this correction only in the Lagrangian formulation.

Rotation changes the shape of massive stars. The radius has to be replaced by $r_P = \sqrt[3]{\frac{3}{4\pi}V_P}$, where V_P is the volume inside an isobar. Scalar values are replaced by mean values on an isobar, i.e. $\bar{\rho}$. The independent variable m_P is the mass enclosed by an isobar.

With these definitions, the equation of continuity becomes

$$\frac{\partial r_P}{\partial m_P} = \frac{1}{4\pi r_P^2 \bar{\rho}}. \quad (2.43)$$

To replace the equation of hydrostatic equilibrium, we have to calculate averages over the surface of an isobar S_P

$$\langle q \rangle = \frac{1}{S_P} \int_{\Psi=const} q \, d\sigma. \quad (2.44)$$

The gravitational acceleration has to be replaced by the effective gravity g_{eff} . Rotation manifests itself in a pressure distortion f_P

$$\frac{\partial P}{\partial m_P} = - \frac{Gm_P}{4\pi r_P^4} f_P, \quad (2.45)$$

$$f_P = \frac{4\pi r_P^4}{Gm_P S_P} \frac{1}{\langle g_{eff}^{-1} \rangle}. \quad (2.46)$$

As an approximation, the energy conservation can be written as

$$\frac{dl_P}{dm_P} = \sum_i \epsilon_i. \quad (2.47)$$

Finally, the energy transport includes either the pressure distortion or another correction factor f_T for the temperature distortion, depending on the transport

process

$$\frac{\partial \ln T}{\partial m_P} = - \frac{Gm_P}{4\pi r_P^4} f_P \min \left\{ \nabla_{ad}, \nabla_{rad} \frac{f_T}{f_P} \right\} \quad (2.48)$$

$$f_T = \left(\frac{4\pi r_P^2}{S_P} \right)^2 \frac{1}{\langle g_{eff} \rangle \langle g_{eff}^{-1} \rangle} \quad (2.49)$$

2.4.2 Rotationally Induced Mixing

In a differentially rotating star, a variety of instabilities can occur. These can cause mixing as well as angular momentum transport (in the following denoted by the subscript “*am*”). As convection and the other mixing processes described in Sec. 2.2, also all rotational instabilities, and the angular momentum transport are treated as diffusive processes. In MESA, the total diffusion coefficient resulting from all processes X is calculated via

$$D_{mix,rot} = f \cdot \alpha_{mix} \sum_X \beta_{mix,X} \cdot D_X \quad (2.50)$$

$$D_{am,rot} = \alpha_{am} \sum_X \beta_{am,X} \cdot D_X. \quad (2.51)$$

Each individual contribution can be scaled by β_X ¹⁴. The prefactor for chemical mixing is typically set to $\alpha_{mix} = 1/30$,¹⁵ based on theoretical considerations by Chaboyer and Zahn (1992). The angular momentum transport is calculated using the full influence of all contributions, $\alpha_{am} = 1$.¹⁶ In MESA, it is treated as fully diffusive process. However, there can be advective contributions in other codes, as we will discuss later.

For all instabilities, first the corresponding instability criterion is calculated. If the region is unstable, the diffusion coefficient is calculated, otherwise it is set to zero.

In the following, we will give a short overview about the physics behind the processes as well as the relevant relations. A more comprehensive summary is given by Maeder (2009) and Heger, Langer, and Woosley (2000).

¹⁴MESA parameter `D_X_factor`

¹⁵MESA parameter `am_D_mix_factor`

¹⁶ MESA parameter `am_nu_factor`

Dynamical Shear Instability

This instability was derived by Chandrasekhar (1961). An illustrative analysis was also performed by Hirschi, Maeder, and Meynet (2004).

Let us consider two cells at z , $z + \delta z$ with velocities V , $V + \delta V$. If these two cells are exchanged, work has to be done against gravity. The energy available is the kinetic one. As the cells are assumed to have the same (average) velocity after the exchange, the criterion for stability (Richardson criterion) follows from the Richardson number $\mathcal{R}i$ as

$$\mathcal{R}i = \frac{N^2}{(\partial V / \partial z)^2} > \frac{1}{4} = \mathcal{R}i_{crit}. \quad (2.52)$$

Already for $\mathcal{R}i < 1$ instabilities can occur, however the instability becomes more important for lower numbers. The Brunt-Väisälä frequency is split into the different contributions

$$N^2 = N_T^2 + N_\mu^2, \quad (2.53)$$

$$N_T^2 = \frac{g}{\rho} (\nabla_{ad} - \nabla), \quad (2.54)$$

$$N_\mu^2 = -\frac{g}{\rho} \frac{\phi}{\delta} f_\mu \nabla_\mu. \quad (2.55)$$

Heger, Langer, and Woosley (2000) suggest that the influence of the composition term ∇_μ should be reduced by a factor f_μ ¹⁷ for all instabilities, since the μ -gradients do not fully enter the rotational instabilities. From calibrations of nitrogen surface enrichment, Heger, Langer, and Woosley find $f_\mu = 0.05$.

The diffusion coefficient follows as

$$D_{DSI} = \frac{1}{3} vl = \frac{1}{3} r \Delta \Omega \Delta r. \quad (2.56)$$

However, as discussed by Maeder (2009) and Kippenhahn, Weigert, and Weiss (2012), this effect only occurs in late pre-SN phases.

Secular Shear Instability

Thermal losses can weaken the stability predicted by the Richardson criterion (2.52), resulting in a secular instability. The stability is described

¹⁷MESA parameter `am_gradmu_factor`

by two Richardson-criteria,

$$\mathcal{R}i_1 = \frac{1}{8} \text{Re}_{crit} \mathcal{P} \mathcal{R}i_T > 0 \quad (2.57)$$

$$\text{and } \mathcal{R}i_2 = \mathcal{R}i_\mu > 0, \quad (2.58)$$

splitting the effect of temperature and composition gradients

$$\mathcal{R}i_{T,\mu} = \frac{N_{T,\mu}^2}{(\partial V / \partial z)^2}. \quad (2.59)$$

The Prandtl number \mathcal{P} is given by the ratio of the thermal diffusion timescale to the timescale of angular momentum diffusion, and the critical Reynolds number Re_{crit} is set to 2500 in MESA.

The diffusion coefficient follows from the velocity

$$v_{SSI} = \sqrt{\frac{\nu}{\text{Re}_{crit}} \frac{d\Omega}{d \ln r}} \quad (2.60)$$

$$D_{SSI} = \min \{H_{SSI}, H_P\} \min \{v_{SSI}, c_s\} \left(1 - \frac{\max \{\mathcal{R}i_1, \mathcal{R}i_2\}}{\mathcal{R}i_{crit}} \right), \quad (2.61)$$

where ν is the kinematic viscosity, c_s the sound speed, and the typical length scale $H_{SSI} = \left| \frac{dr}{d \ln v_{SSI}} \right|$.

Solberg-Hoiland Instability

For rotating stars, the Ledoux criterion of stability from Eqn. (2.18) can be generalised including an additional term N_Ω

$$N^2 = N_{ad}^2 + N_\mu^2 + N_\Omega^2 \sin^2 \theta > 0, \quad (2.62)$$

$$N_\Omega^2 = \frac{1}{\bar{\omega}^3} \frac{d(\Omega^2 \bar{\omega}^4)}{d\bar{\omega}} \quad (2.63)$$

where $\bar{\omega}$ and θ are the cylindrical coordinates. Rotation can make a region stable against convection. The diffusion coefficient is given by

$$D = \frac{g}{\rho} \left(\frac{d\rho}{dr} \Big|_{ad} - \frac{d\rho}{dr} \right) + \frac{d(r^2 \Omega)^2}{dr} \frac{1}{r^3} \quad (2.64)$$

$$D_{SH} = \left(\min \{H_{SH}, H_P\} D \frac{r}{g H_P} \right)^2 / \tau_{dyn}, \quad (2.65)$$

where H_{SH} is the extend of the unstable region and $\tau_{dyn} = \sqrt{r^3/(Gm)}$ the dynamical timescale.

Eddington-Sweet Circulation

The Eddington-Sweet or meridional circulation and its treatment is still under discussion. It was fist studied by Eddington (1926), and a more quantitative analysis was performed by Sweet (1950). Zahn (1992) found an improved solution, taking into account momentum conservation.

The general idea is based on the van Zeipel theorem

$$F \sim g_{eff}. \quad (2.66)$$

The flux along the polar axis is larger than in other locations, especially at the equator. A resulting thermal imbalance drives global circulations.

In general, this is an advective transport effect. As argued by Maeder (2009), however, in combination with horizontal turbulence D_h , it might behave the same as a diffusive process for chemical transport. This is not true for angular momentum transport, where, even in combination with horizontal turbulence, there remains an advective term. Some stellar evolution codes, such as GENEC, include the advective treatment for angular momentum transport, while other codes, such as MESA or STERN, treat it as a diffusive effect. This can lead to huge differences, as we will see in Sec. 3.4.1.

An expression for the circulation velocity was found by Kippenhahn (1974)

$$v_e = \frac{\nabla_{ad}}{\delta(\nabla_{ad} - \nabla)} \frac{\Omega^2 r^3 l}{(Gm)^2} \left(\frac{2(\epsilon_n + \epsilon_\nu) r^2}{l} - \frac{2r^2}{m} - \frac{3}{4\pi\rho r} \right). \quad (2.67)$$

Composition gradients can have a stabilising effect

$$v_{ES} = |v_e| - |v_\mu|, \quad (2.68)$$

$$v_\mu = \frac{H_p}{\tau_{KH}^*} \frac{\rho \nabla_\mu}{\delta(\nabla - \nabla_{ad})}, \quad (2.69)$$

where the Kelvin-Helmholtz timescale is

$$\tau_{KH}^* = \frac{Gm^2}{r(l - m\epsilon_\nu)}. \quad (2.70)$$

The situation is unstable if $\nu > 0$. In this case the diffusion coefficient is calculated from the circulation velocity

$$D = \min \{H_{ES}, H_P\} \min \{v_{ES}, c_s\}. \quad (2.71)$$

The typical length scale of this instability is $H_{ES} = \left| \frac{dr}{d \ln v_{ES}} \right|$.

Goldreich-Schubert-Fricke Instability

This secular instability was described by Goldreich and Schubert (1967) and Fricke (1968).

First Goldreich and Schubert only analysed the destabilisation by highly negative $N_\Omega^2 < 0$, later Fricke included a finite viscosity ν and thermal diffusivity K_{therm} such that the condition for instability becomes

$$\frac{\nu}{K_{therm}} N_{ad}^2 + N_\Omega^2 < 0 \quad (2.72)$$

$$\text{or } \frac{\nu}{K_{therm}} N_{ad}^2 - \left| \bar{\omega} \frac{\partial \Omega^2}{\partial z} \right| < 0. \quad (2.73)$$

The diffusion coefficient depends on the characteristic velocity

$$v_{GSF} = \left| v_e \frac{2H_{Tr}}{H_j^2} \frac{1}{1 + 2\Omega \frac{d \ln r}{d \Omega}} \right| - |v_\mu|, \quad (2.74)$$

$$D_{GSF} = \min \{H_{GSF}, H_P\} \min \{v_{GSF}, c_s\}, \quad (2.75)$$

where $H_{T/j} = \left| \frac{dr}{d \ln(T/j)} \right|$ is the scale height of the temperature/angular momentum distribution, and H_{GSF} is the minimum of the extent of the unstable region and the typical length scale $\left| \frac{dr}{d \ln v_{GSF}} \right|$.

Viscosity

Small scale motions of atoms or ions can transport angular momentum. We follow the description of Kippenhahn, Weigert, and Weiss (2012). The viscosity coefficient due to this microscopic motion is given by

$$\eta = \rho l v_{therm}, \quad (2.76)$$

where l is the mean free path. Using the Navier-Stokes equation including viscosity, the timescale follows as

$$\tau_{visc} \approx \frac{d^2 \rho}{\eta} \quad (2.77)$$

where d is the typical length-scale of changes in the rotation Ω . As η is typically $\mathcal{O}(1)$ in cgs units, d is $\mathcal{O}(R_\odot)$ and ρ is $\mathcal{O}(1)$ in cgs units, the typical timescale is $\tau_{visc} \approx 10^{22} \text{s} \approx 3 \cdot 10^5 \text{ Gyr}$ which is much larger than the lifetime of stars and even than the universe. Thus the influence of viscosity can be neglected.

2.5 Magnetic Fields

Magnetic fields in the sun have already been measured by Hale (1908). Further evidence for the presence of magnetic fields in massive stars was the observation of strongly magnetic neutron stars (magnetars). Duncan and Thompson (1992) and Thompson and Duncan (1995) developed the theory of magnetic neutron stars which requires magnetic fields in the progenitor.

Meanwhile, magnetic fields have been detected in a variety of stars. Depending on the stellar mass, different methods can be used to observe magnetic fields. A large survey of magnetic fields in massive stars is the **MiMeS** survey by Wade et al. (2009, 2011, 2016).

While for low mass stars the Zeeman-effect in a single spectral line is sufficient to derive the magnetic field strength, for massive stars the noise is too high. Instead, a cross correlation of the variation in polarisation across spectral lines all over the spectrum has to be performed to increase the signal-to-noise ratio.

Different observations agree that the total number of massive stars hosting magnetic fields is $\approx 10\%$ (Hubrig 2008, Grunhut, Wade, and MiMeS Collaboration 2012, Bagnulo et al. 2020).

Typical magnetic field strengths have been summarised by Petit et al. (2012) and range from some 100 G for so-called dynamical magnetospheres to very high field strengths of some 1000 G for “centrifugal magnetospheres”. Magnetic fields play a role for all stages of stellar evolution. From fragmentation of molecular clouds (Palau et al. 2020), over star formation (Liu et al. 2020, Girart et al. 2009, Zhang 2020) to remnants (Schneider et al. 2020, Tremblay et al. 2015) and all stages in between, which we are particularly interested in.

There are two main effects of magnetic fields. The first is its impact on the

stellar wind. A dipole field significantly changes the structure of the wind (ud-Doula and Owocki 2002, ud-Doula, Owocki, and Townsend 2008). Material can get trapped by closed field lines and falls back to the surface. The total mass loss thus is reduced. Petit et al. (2017) show that this effectively mimics a star with lower metallicity. The reduced mass loss might explain the existence of more massive black holes and gamma-ray bursts (**GRB**) also at higher metallicity.

Keszthelyi et al. (2020) show, based on the idea of ud-Doula, Owocki, and Townsend (2009), that the coupling of the surface to the wind can slow down the rotation drastically. In addition, internal magnetic fields cause efficient angular momentum transport and solid body rotation (Maeder and Meynet 2003, 2004, 2005).

The source of magnetic fields is still under discussion. For low mass stars, a dynamo effect in the convective envelope can explain the observed magnetic fields. However, for massive stars this mechanism does not work as they do not have a convective envelope but a convective core where the magnetic field is well confined due to the high density and composition gradients (MacDonald and Mullan 2004).

Spruit (1999, 2006) found an alternative dynamo mechanism maintaining the magnetic field acting in the radiative envelope. The dynamo needs some fossil field and consists of two steps: A poloidal magnetic field B (with radial component B_r important in this context) is generated by the displacement of the toroidal field. Differential rotation twists this poloidal field into a toroidal one. The mathematical description is complicated, and a comprehensive summary is given by Maeder and Meynet (2004).

Soon after the formulation, this description has been implemented into various stellar evolution codes (MESA: Paxton et al. 2013, STERN: Petrovic et al. 2005, Brott et al. 2011). It can reproduce the rotation rates of remnants (Heger, Woosley, and Spruit 2005 and Suijs et al. 2008) as well as the solar rotation rates as Eggenberger, Maeder, and Meynet (2005) show¹⁸. Nevertheless, the treatment is inconsistent as only angular momentum transport is included. If chemical mixing would be calculated, the effect would be much too large.

The validity of the Spruit-Taylor dynamo is still under discussion (Zahn, Brun, and Mathis 2007, Denissenkov and Pinsonneault 2007, Braithwaite and Spruit 2017) and most likely cannot explain the observed magnetic fields (Cantiello and Braithwaite 2019). One currently used alternative are fossil fields. These can survive the main sequence for massive stars as Alecian et al. (2019) discuss. It is

¹⁸Charbonnel and Talon (2005) show that this could also be explained by gravity waves.

not clear, if they decay until the B supergiant phase or are just too weak to be observed.

Another option are that magnetic fields originate from mergers (Ferrario and Wickramasinghe 2005, Ferrario et al. 2009, Schneider et al. 2019). This has the advantage that it can explain, why only 10% of the massive stars host magnetic fields.

2.6 Stellar Winds

The winds of massive stars are important for the evolution of the stars as well as their neighbourhood. Massive stars can enrich the interstellar medium with processed elements and also trigger star formation. For the star itself the mass loss is a decisive parameter to determine the evolution, since massive stars can loose a significant fraction of their initial mass.

Exact mass loss rates are still under debate, and a still valid review has been presented by Puls, Vink, and Najarro (2008).

Depending on the evolutionary state, as well as the temperature of the star, different mechanisms can be responsible for the mass loss. The main mechanisms for massive stars are line driven and dust driven winds. For very massive stars, $M \gg 80M_{\odot}$, even a continuum driven wind, which is independent of metallicity Z , might be present, changing the behaviour of stars at low metallicity.

A huge uncertainty comes from the mass loss rate of luminous blue variable stars, which is very high but, in MESA, missing an adequate description, as discussed in Sec. 3.2.3.

Typical mass loss rates for massive main sequence stars at solar metallicity are on the order of $\mathcal{O}(10^{-7 \dots -5}) M_{\odot}/\text{yr}$ on the main sequence. During later phases the mass loss rates can be higher, up to $\approx 10^{-3.8} M_{\odot}/\text{yr}$.

2.6.1 Line Driven Mass Loss

The theory of line driven winds has been pioneered by several authors (Lucy and Solomon 1970, Castor 1974, Castor, Abbott, and Klein 1975 (**CAK**)). In the following we will give a short overview about this theory.

The wind can be described by the equation of continuity (2.3) and the Euler equation (2.5). An expression for the line acceleration has to be included. A comprehensive summary of the derivation is given by Maeder (2009), and Puls,

Springmann, and Lennon (2000). In this thesis we only want to give the most important steps and relations.

The CAK line acceleration is written as acceleration resulting from the most important continuum processes in massive hot stars, Thomson scattering (scattering at free electrons), corrected by a so-called force multiplier $M(t)$. The latter is a function of the depth parameter t^{19} , that takes into account the contribution of line-processes relative to Thomson-scattering,

$$g_t = \frac{\sigma_e F}{c} M(t), \quad (2.78)$$

where σ_e is the electron-scattering cross section σ_{Th} divided by the density, $\sigma_e = \frac{\sigma_{Th}}{\rho}$. Summing up over many lines, CAK find

$$M(t) = kt^{-\alpha} \quad (2.79)$$

where k and α are force multipliers. α is the ratio of the contribution of line acceleration from only optically thin and all lines. Typical values range from $\alpha = \frac{1}{2} \dots \frac{2}{3}$. The optical depth parameter is calculated following the approximation by Sobolev (1947),

$$t = \frac{\sigma_e \rho v_{th}}{dv/dr}, \quad (2.80)$$

where v_{th} is the thermal velocity. Inserting the force from Eqn. (2.78) in the equation of motion, setting $\alpha = \frac{1}{2}$, applying specific approximations and integrating yields the velocity law

$$v = v_\infty \left(1 - \frac{R}{r}\right)^{\frac{1}{2}}. \quad (2.81)$$

The exponent $\frac{1}{2}$ can be generalised to β . Pauldrach, Puls, and Kudritzki (1986) find $\beta = 0.8$ taking into account the finite disk the star covers. The terminal velocity v_∞ is typically on the order of $\mathcal{O}(3v_{esc})$.

From the equation of motion, when the escape speed v_{esc} accounts for the effective gravity corrected for Thomson scattering, the mass loss rate follows as

$$\dot{M} \sim L^{1/\alpha} (GM(1 - \Gamma_e))^{\frac{\alpha-1}{\alpha}}. \quad (2.82)$$

¹⁹ t is an approximation (in the limit of steep velocity gradients) for a line optical depth, with a line strength corresponding to electron scattering.

Line driven wind strongly depends on metallicity. A scaling

$$\dot{M} = Z^{\frac{1-\alpha}{\alpha-\delta}} \quad (2.83)$$

can be found (Puls, Springmann, and Lennon 2000). An important relation is the wind-momentum luminosity relation (**WLR**). It connects the mass loss rate, the terminal velocity and the stellar radius to the luminosity, and can be derived from the above results by approximating $\alpha \approx 2/3$,

$$\dot{M} v_{\infty} R^{1/2} \sim L^{1/\alpha}. \quad (2.84)$$

This relation allows precise distance determinations. The mass loss rate and the terminal velocity can be measured from H α emission lines and UV P-Cygni profiles, respectively.

One huge source for uncertainties in the measurement of mass loss rates is clumping (wind inhomogeneities) in the mass outflow. The effect of clumping has been suggested in various simulations (Owocki, Castor, and Rybicki 1988, Feldmeier 1993), and confirmed in various observations (e.g., Najarro et al. 2008, and the review by Puls, Vink, and Najarro 2008). If neglected in corresponding analyses, clumping would mimic higher mass-loss rates than actually present. Though the precise clumping degree is still unknown, new measurements and simulations (Sundqvist et al. 2019, Björklund et al. 2020) indicate that the currently used mass-loss rates should be reduced by a factor of 2...3.

Vink Mass Loss Rates and the Bi-Stability Jump

A widely used recipe to predict line driven mass loss rates has been developed by Vink, de Koter, and Lamers (2001).

One of their important results (consistent with earlier findings by Pauldrach and Puls 1990) is that the mass loss rates are not smooth but have jumps at certain (effective) temperatures. At these temperatures, the force multipliers change drastically due to ionisation effects, finally affecting v_{∞} and \dot{M} .

The exact positions of these jumps are metallicity dependent. According to Vink, de Koter, and Lamers, their position should be related to a density

$$\log(\rho) = -13.636 + 0.889 \log\left(\frac{Z}{Z_{\odot}}\right) \quad (2.85)$$

which leads, for galactic conditions, to the following “jump temperatures”:

$$T_{eff}^{jump} = 192 + 10.4 \log(\rho) \approx 35 \text{ kK} \quad (2.86)$$

$$T_{eff}^{jump} = 61.2 + 2.59 \log(\rho) \approx 25 \text{ kK} \quad (2.87)$$

$$T_{eff}^{jump} = 43 + 1.9 \log(\rho) \approx 15 \text{ kK}. \quad (2.88)$$

The jump at 35 kK is due to carbon recombination and only plays a role in low metallicity environments. As the mass loss rates decrease with decreasing metallicity, it does not play a crucial role at all. The other two jumps are a result of changes of the ionisation state of iron.

Models by Petrov, Vink, and Gräfener (2014, 2016), as well as observations (Lamers, Snow, and Lindholm 1995, Markova and Puls 2008) revise the above jump temperatures. The jump predicted by Vink, de Koter, and Lamers to be located around 25 kK (usually called the first jump) is most likely around 20 kK. The “second jump” predicted at ≈ 15 kK is thought to be actually located below 9 kK and thus below the range where the Vink mass loss scheme is typically applied. Furthermore, de Koter (2008) argue that the jump has observational problems, and different observations disagree on its impact.

Because of these arguments, MESA only includes the jump calculated following Eqn. (2.87) at $T_{eff} \approx 25$ kK where Fe IV recombines into Fe III. Other codes such as GENEC also include the second jump at ≈ 15 kK.

Accounting for the above jump temperatures, Vink, de Koter, and Lamers provide mass loss rates that are applicable for $T_{eff} \approx 12.5 \dots 50$ kK.

On the hot side of the first jump they find

$$\begin{aligned} \log\left(\frac{\dot{M}}{M_{\odot}/\text{yr}}\right) = & -6.697 + 2.194 \log\left(\frac{L}{10^5 L_{\odot}}\right) \\ & - 1.313 \log\left(\frac{M}{30 M_{\odot}}\right) - 1.226 \log\left(\frac{v_{\infty}}{2v_{esc}}\right) \\ & + 0.933 \log\left(\frac{T}{4 \cdot 10^4 \text{ K}}\right) - 10.92 \left(\log\left(\frac{T}{4 \cdot 10^4 \text{ K}}\right)\right)^2 \\ & + 0.85 \log\left(\frac{Z}{Z_{\odot}}\right). \end{aligned} \quad (2.89)$$

The ratio of terminal to escape velocity is a result by Pauldrach, Puls, and Kudritzki (1986), including empirical metallicity scaling following Leitherer,

Robert, and Drissen (1992)

$$\frac{v_{\infty}}{v_{esc}} = 2.6 \left(\frac{Z}{Z_{\odot}} \right)^{0.13} \quad (2.90)$$

When crossing the jump, the mass loss increases by a factor of 5 or more. On the cool side Vink, de Koter, and Lamers predict

$$\frac{v_{\infty}}{v_{esc}} = 1.3 \left(\frac{Z}{Z_{\odot}} \right)^{0.13}, \quad (2.91)$$

$$\begin{aligned} \log \left(\frac{\dot{M}}{M_{\odot}/\text{yr}} \right) = & -6.688 + 2.21 \log \left(\frac{L}{10^5 L_{\odot}} \right) \\ & - 1.339 \log \left(\frac{M}{30 M_{\odot}} \right) - 1.601 \log \left(\frac{v_{\infty}}{2 v_{esc}} \right) \\ & + 1.07 \log \left(\frac{T}{4 \cdot 10^4 \text{ K}} \right) \\ & + 0.85 \log \left(\frac{Z}{Z_{\odot}} \right). \end{aligned} \quad (2.92)$$

According to Vink, de Koter, and Lamers (2001), this recipe only covers the metallicity range $3Z_{\odot} \dots \frac{1}{30}Z_{\odot}$. Since the wind is very weak for very low Z , basically no mass is lost for a non rotating model. In our investigations, we also apply this scheme for lower metallicities than $\frac{1}{30}Z_{\odot}$.

Alternative mass loss descriptions are given by Nieuwenhuijzen and de Jager (1990) and van Loon et al. (2005).

An important observational finding is that the mass-loss rates change only weakly over the jump (if at all), contrasted to the theoretical predictions from above (Markova and Puls 2008). In connection with the erroneous position of the jump temperatures, this leads to large overestimates of the mass-loss rates in the jump regimes and particularly in the region below 15 kK, where the Vink, de Koter, and Lamers mass-loss rates might overestimate the actual values much more than the factor 2...3 discussed above.

Wolf-Rayet Mass Loss

Nugis and Lamers (2000) observed 44 WN and WC stars²⁰ to derive mass loss rates. The mass loss in this phase is much higher than during earlier phases. They find that the mass loss rates depend not only on metallicity Z and luminosity

²⁰Compare Sec. 3.2.4 for an explanation of the Wolf-Rayet classification.

L , but also on the surface helium content Y ,

$$\frac{\dot{M}}{M_{\odot}/\text{yr}} = 10^{-11} \cdot \left(\frac{L}{L_{\odot}} \right)^{1.29} Y^{1.7} Z^{0.5}. \quad (2.93)$$

This is already smaller than previously thought, by about 0.2...0.6 dex. Because of clumping, the real rates might be even lower.

2.6.2 Dust Driven Mass Loss

As an alternative to the absorption and scattering in spectral lines, also dust grains can act as a driver. Dominik (1990) provides an extensive overview about the formation of dust and how it drives the mass loss. For red giants, molecules can form in the cooler outer photosphere. For even lower temperatures, the molecules can form dust grains. The dust can absorb high energy photons while radiating away infrared radiation. Observations have proven the infrared excess of such giants (Sakon et al. 2010). In addition, the photon momentum is redistributed from the dust to the gas by collisions. This way dust can drive a very strong mass loss.

While this process works for asymptotic-giant-branch stars, it is not proven if it also works for red supergiants, i.e. massive stars. The major problem is the wind close to the star, where the dust forms. In evolved red giants, strong pulsations accelerate the lower wind and compress the plasma, such that dust can form. In red supergiants, there are no such pulsations. It is speculated, that the lower wind of these stars might be accelerated by molecular lines (Josselin and Plez 2007).

De Jager, Nieuwenhuijzen, and van der Hucht (1988) found an empirical formula for the mass loss rates of supergiants,

$$\log \left(\frac{\dot{M}}{M_{\odot}/\text{yr}} \right) = 1.769 \log \left(\frac{L}{L_{\odot}} \right) - 1.676 \log \left(\frac{T}{1 \text{ K}} \right) - 8.158. \quad (2.94)$$

This equation was developed for roughly solar metallicities, it does not contain any metallicity dependence, which can be a problem for very low metallicity.

The scaling of the de Jager, Nieuwenhuijzen, and van der Hucht (1988) mass loss rates with metallicity is still under discussion. Van Loon (2006) discuss different possibilities. The absorption by dust may reach saturation, such that also in reality there is no metallicity dependence, at least in the range $0.2Z_{\odot} < Z < 3Z_{\odot}$. However, for lower metallicities the molecules may contain more oxygen compared

to carbon and thus be a less efficient driver. For very low metallicities, no dust may form at all.

As an alternative, very metal poor stars may have a chromosphere driven mass loss. This idea is described by Schröder and Cuntz (2005). The chromosphere is highly turbulent. Alfvén waves transport energy to outer layers and deposit it in the chromosphere. They can drive a mass loss rate

$$\dot{M} = \eta \frac{L_* R_*}{M_*} \left(\frac{T_{eff}}{4000\text{K}} \right)^{3.5} \left(1 + \frac{g_\odot}{4300g_*} \right), \quad (2.95)$$

which is similar to Reimers' law (Reimers 1975, 1977). From a fit to the red-giant-branch they find $\eta = 8 \cdot 10^{-14} M_\odot/\text{yr}$. Thus, the mass loss may be even higher for metal poor stars, as pointed out by van Loon (2006).

However, this high mass loss has one problem, and thus most likely is not realistic. The Alfvén point, where the mass loss originates, is far outside. The mass in this region is too low to explain high mass loss rates.

An alternative was provided by Maeron and Josselin (2011). They add an additional term $\alpha \log\left(\frac{Z}{Z_\odot}\right)$, $\alpha = 0.7$ to the de Jager, Nieuwenhuijzen, and van der Hucht (1988) rates from Eqn. (2.94). This is similar to the scaling of other mass loss rates such as from Vink, de Koter, and Lamers (2001).

Until to date it is not clear, which of these assumptions is the most physical one.

2.6.3 Mass Loss at Critical Rotation

If the star gets closer to critical rotation, the outer layers can become unstable and finally unbound.

In general, there are some requirements a mass loss scheme for rotating stars has to fulfil. According to the van Zeipel theorem, the flux is higher at the poles, such that also the mass loss is higher. The total mass loss should not change as long the star is not too close to criticality. In contrast to that, when the star gets closer to critical rotation,²¹

$$\Omega_{crit} = \sqrt{(1 - \Gamma_e) \frac{GM}{R^3}}, \quad (2.96)$$

²¹The following is only a 1d approximation, neglecting gravity darkening. The reality is more complex, see, e.g., Puls, Vink, and Najarro (2008).

the centrifugal forces at the equator approach the gravitational force and the material can become unbound²². Thus the mass loss increases drastically. To cover all effects, full 3d simulations, and, even more important, calculations of the occupation numbers in Non-Local Thermodynamic Equilibrium (**NLTE**), would be necessary.

MESA has different possibilities how the increase in mass loss is approximated. The first option is a correction factor

$$\frac{\dot{M}(\Omega)}{\dot{M}(0)} = \left(1 - \frac{\Omega}{\Omega_{crit}}\right)^{-\alpha}, \quad (2.97)$$

which was derived by Bjorkman and Cassinelli (1993) based on results by Friend and Abbott (1986). Langer (1998) found $\alpha = 0.43$.

However, the validity of this form has been questioned by Owocki, Cranmer, and Gayley (1996). A better description is the generalised $\Omega\Gamma$ limit, which was derived by Maeder and Meynet (2000).

As an alternative, MESA can calculate an “implicit mass loss rate”, such that the rotation is kept just below the critical value. If the rotation is too high, $\Omega > \Omega_{limit}$ ²³, then the mass loss is increased, until the rotation is subcritical again, and the mass loss rate within a given tolerance. We choose an upper limit $\Omega_{limit} = 0.96$ consistent with Ferraro (2020). A more detailed description on how this is evaluated in MESA is given in the App. A.5.2.

2.6.4 Dutch Wind Scheme

In this work we use the description of Glebbeek et al. (2009) that combines different mass loss rates for different regimes where they are applicable. For stars at high temperatures (> 10 kK) that still have their envelope, the Vink, de Koter, and Lamers (2001) rates are applied.

Wolf-Rayet stars are identified by a maximum surface hydrogen content $X < 0.4$ (Eldridge and Vink 2006). In this case the rates by Nugis and Lamers (2000) are used.

For lower temperatures (below 8 kK), so mainly for Red Supergiants, the de Jager, Nieuwenhuijzen, and van der Hucht (1988) rates are utilised.

²²As we can see, another alternative to increase Ω/Ω_{crit} is to have $\Gamma_e \rightarrow 1$

²³MESA parameter `surf_w_div_w_crit_limit`

3 Stellar Evolution and MESA

The evolution of stars is strongly mass dependent. More massive stars are more luminous and thus evolve faster, but can also reach later burning phases. In addition to mass, there is a metallicity dependence of the evolution. Metal poor stars are more compact and have less mass loss. Finally, the evolution depends on the rotation rates.

An illustrative summary about stellar evolution is given by Kippenhahn, Weigert, and Weiss (2012). In the following, we want to provide a short overview about the different phases of evolution, and the dependencies of the evolutionary pathways on the most important parameters.

Stars can be characterised depending on their initial mass or, more precisely, on some characteristic properties of their evolution. While low mass stars ($M_i \lesssim 2M_\odot$) and intermediate mass stars ($M_i \approx 2 \dots 8M_\odot$) can have degenerate burning phases already in their earlier evolution, high mass stars ($M_i \gtrsim 8M_\odot$) ignite all burning processes until carbon in a non degenerate core. Thus their evolution is smooth, they do not produce any flashes.

In addition, high mass stars end their lives with a core collapse, and produce massive remnants such as black holes, or neutron stars which we will discuss later in more detail. As the aim of this thesis is to provide initial stellar mass ranges for these compact remnants to form, and use the remnant masses for statistics useful for microlensing observations, as discussed in Chpt. 1, we are particularly interested in the evolution of massive stars.

3.1 Main Sequence

A star is born, when a contracting cloud ignites hydrogen burning in its center. This is when the star reaches the zero-age main sequence (**ZAMS**) and starts the evolution that we consider. The following phase, while the star transforms

hydrogen into helium in its center, is called main sequence (**MS**), as it lasts more than 85% of its total lifetime.

There are different processes, that can convert hydrogen into helium. In general, four protons (hydrogen nuclei) are needed to combine into one helium nucleus. The simplest way to imagine is the p-p chain. Protons build up into a helium nucleus in several steps. Especially the weak interactions, that convert protons into neutrons, determine the timescale of this process.

An alternative is the CNO cycle. It uses carbon, nitrogen and oxygen as catalyst, and thus can change their individual number fractions while the total number is unchanged. Especially the increase of carbon at the expense of nitrogen can be an observational tracer, if it is mixed to the surface. The CNO cycle is much more efficient than the p-p chain for stars more massive than $M_i \geq 1.2M_\odot$ (Maeder 2009).

Because of the steep temperature gradient due to efficient burning, massive stars have a convective core and a huge radiative envelope. This provides very efficient mixing in the core, as argued in Sec. 2.2.

The burning processes adjust to the outer properties of the star. In the other direction, there is only some feedback, such as ionisation. As massive stars are mainly radiative during the main-sequence, the total luminosity scales with $L \sim M^\alpha \mu^4 / \kappa$, where $\alpha \approx 2.3 \dots 3$, and μ is a mean value averaged over the whole stellar radius. We can use this relation to obtain an estimate of the MS lifetime. The material available for fusion processes is $\sim M$, typically $\mathcal{O}(0.1) M_i$. Thus, a simple scaling relation for the lifetime is $\tau_{MS} \sim \frac{M_i}{L} \sim M^{1-\alpha}$. Massive stars live shorter than lower mass stars, typically $\mathcal{O}(10^{6 \dots 7})$ yr.

In addition, the fact that $L \sim \mu^4$ predicts that the luminosity increases on the main sequence as more hydrogen is transformed into helium. In parallel, the star expands, but with a very weak dependence of R on μ , such that the temperature T_{eff} decreases.

Different parameters such as rotation rates and overshooting values can influence the evolution. In general, all effects that allow more efficient mixing and increase the core mass during the main sequence also increase the luminosity.¹ They also increase the lifetime as more material is available to be burned.

A special case is when the mixing is so efficient that it causes the star to evolve quasi chemically homogeneously (**QCHE**). These stars evolve on different ZAMSs

¹Analytical relations connecting core and envelope masses to observables can be found in Farrell et al. (2020).

(in dependence of composition) to higher temperatures and higher luminosities.

3.2 Later Evolutionary Phases

3.2.1 Hertzsprung Gap

When hydrogen is depleted in the core, the star contracts as no internal energy source, and thus no stabilising pressure is present. The effective temperature increases, appearing as “hook” after the MS in a HRD.

As soon as shell burning sets in, the core continues to contract, but the envelope expands in a quasi-static way. This is known as “mirror effect”, and is found in many simulations. This expansion happens on short thermal timescales, making observations of stars in this phase very unlikely. The region where the stars evolve rapidly is known as Hertzsprung-gap.

As its radius is increasing, the star evolves to lower effective temperatures. Consequently, the opacity in its envelope is increasing and finally allows for convection. The star forms a huge convective envelope, and the evolution continues close to the Hayashi line with almost constant temperature. The Hayashi line is the (mass and metallicity dependent) region of stars that are fully convective. It marks a lowest effective temperature, where stars can exist.

If the convective envelope extends deep enough, processed material can be mixed upwards, and change the surface abundances, known as “dredge up”.

3.2.2 Helium Core Burning to Carbon Core Burning

As soon as central helium burning is ignited, the evolution continues on the longer nuclear timescale τ_{nuc} . Stars more massive than $2M_{\odot}$ ignite helium in a non-degenerate core, defined as the limit for intermediate mass stars.

As intermediate mass stars evolve along the Hayashi line, they form a radiative envelope at the tip of the red giant branch. After core helium ignition, intermediate mass stars can perform one or more blue loops, again found from stellar evolution calculations. On that way, stars up to $20M_{\odot}$ can cross the Cepheid-instability region several times (Turner 1996).

Unlike low and intermediate mass stars, higher mass stars can continue the bluewards evolution if they lost enough mass and become blue supergiants or even Wolf-Rayet stars.

As the energy released by burning helium is lower than for hydrogen burning, and also the amount of available material is smaller, the timescales of these later phases become shorter.

Massive stars even ignite carbon burning in a non degenerate core. This burning phase has a convective core for stars up to $19M_{\odot}$, and a radiative one for higher masses, because of neutrino losses (Timmes, Woosley, and Weaver 1996). The timescale is on the order of $\mathcal{O}(10^3)$ yr and even shorter for later burning phases.

The evolutionary paths discussed depend strongly on the initial mass, overshooting and mass loss rates. While stars up to $25M_{\odot}$ end their life as red supergiants, higher mass stars have more mass loss, and thus end their life as blue supergiants or even as Wolf-Rayet stars. Massive stars can also evolve through the luminous blue variable phase, that will be discussed in the next section.

3.2.3 Luminous Blue Variable Stars

Luminous blue variable (**LBV**) stars are discussed, e.g., in a review paper by Humphreys and Davidson (1994). They are unstable massive stars, that are located characteristically in the blue, but do not need to be there always. The region of instability is specified by the observational Humphrey-Davidson limit, a temperature dependent maximum luminosity. Typically, LBV stars are located close to the Eddington limit $\Gamma_e = \frac{\kappa L}{4\pi cGM}$ within a factor of 2, such that their stability is reduced. Nevertheless, the mechanism of the instability is still under discussion. There may be even a combination of several.

One idea was the ϵ mechanism, which is no longer a leading explanation. Modern ideas include a modified Eddington limit, turbulent pressure, or some subphotospheric instability. Some LBVs may be a result of binary interactions, as suggested by their bipolar structure.

The instability manifests itself on different scales. There can be small variations up to giant eruptions as observed for η Car (van Genderen and The 1984). Changes in the observed properties are mainly connected to a variability in temperature, not luminosity. This is related to an optically thick, expanding atmosphere, that we observe as “pseudo-photosphere”. As the surface and thus the radius is hard to define, an apparent temperature T_{app} , defined from the energy distribution, has to be employed. Two states can be observed. An eruptive one at $T_{app} \approx 7 \dots 8$ kK and a quiescent one at $T_{app} \approx 12 \dots 30$ kK. During the eruptive state the mass loss is drastically increased, up to $\dot{M} = 10^{-5 \dots -4} M_{\odot}/\text{yr}$. However, this value is model

dependent and highly uncertain. There can be single eruptions where $2 \dots 3M_{\odot}$ are lost within a few years, as observed for η Car.

The star stays in the LBV phase for some 10000 yr, when it finally lost enough mass to become a Wolf-Rayet star.

3.2.4 Wolf-Rayet Stars

Wolf-Rayet (**WR**) stars have been reviewed by Crowther (2008). (Classical) WR stars are “naked cores”, meaning massive stars that completely lost their hydrogen rich envelope.

Similar to LBV stars, WR stars are characterised by a very dense wind, such that the temperature definition is challenging. Differences, depending on the temperature-definition, can be seen, e.g., in the work by Groh et al. (2014). To compare MESA calculations with observations, they should be coupled to a stellar atmosphere code.

The classification of WR stars is based on the spectrum. Surface abundances and ionisation stages act as discriminant between different types. If the ionisation is high, they are called “early type”, for low ionisation “late type”. If they still show helium in their spectra, they are classified as WN. Helium poor, but carbon rich stars are classified as WC, where there exists a transition WN/C type. If they show primarily oxygen on their surface, they are called WO stars. This distinction is connected to an evolutionary scenario. Stars first loose their hydrogen envelope, and become WN stars. If they loose their helium envelope, they become WC and, for even more mass lost, WO stars.

An exception are the mid-type WNH stars which still show hydrogen in their spectra. These are believed to still be on the main sequence. Massive stars can develop a pseudo-photosphere for very strong mass loss and thus show a WR like appearance.

Also the mass loss rates of classical WR stars are very high, as described in Sec. 2.6. However, many values derived from observations need to be reduced, when accounting for clumping effects.

3.3 Important MESA Parameters

As discussed already, MESA contains a variety of different options for the treatment of physical processes. While working with MESA, we found some of

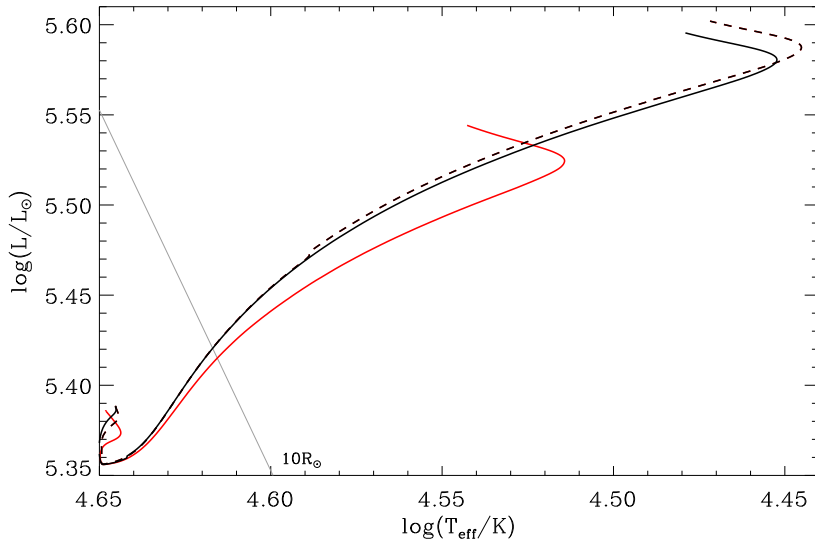


Figure 3.1: Comparison between a $40M_{\odot}$ model calculated using the Ledoux criterion (solid) and the Schwarzschild criterion (dashed), without overshooting and rotation. The smoothing parameter is varied between 0 and 3, and affects the evolution drastically if the Ledoux criterion is applied. Without smoothing, the track calculated with the Schwarzschild criterion separates from the one with Ledoux criterion.

them to be of great importance for the evolution, while others have only small effects. In the following we want to summarise the impact of some important parameters.

3.3.1 μ -Barrier

Theoretical considerations predict a μ -barrier at the boundary of the convective core, if it is treated with the Ledoux criterion.

The Ledoux and Schwarzschild criterion are the same, until a composition gradient has build up. From this moment on, the convective core predicted by the Ledoux criterion is limited to the region inside this “ μ -barrier”, and thus is smaller compared to calculations with the Schwarzschild criterion. As argued already, a smaller core mass leads to a lower luminosity. We see this as separation on the main sequence shown in Fig. 3.1 for the black tracks.

Rotation produces two opposite effects. Rotational instabilities can mix material through the convective envelope, reducing the effect of the composition gradient. In contrast, also these processes are affected by the μ -barrier, and may not allow mixing beyond it, as described in Sec. 2.4.2. In most cases, mixing beyond the

μ -barrier is still shielded. Finally, this leads to lower luminosities in the Ledoux case, compared to the Schwarzschild one, where processed helium is still mixed to the surface.

However, MESA smooths the composition gradient by default. The parameter `num_cells_for_smooth_gradL_composition_term` is set to 3. The impact can be seen in the red curve. The track calculated using the Schwarzschild criterion is unchanged, while in the Ledoux case it changes drastically and produces unphysical results. If overshooting is applied, the differences on the main sequence are removed, as overshooting allows mixing beyond the μ barrier. One case, where the impact of the μ -barrier can still be seen, are rotating models at very low metallicity. The smoothing parameter is decisive for the existence of this barrier. If smoothing is applied, more models show QCHE compared to calculations without smoothing.

We conclude that the smoothing parameter should only be set, when the Schwarzschild criterion is applied, or, even better, turned completely off!

3.3.2 Undershooting Problem

As described in Sec. 2.2.4, MESA has the possibility to set different overshooting values for different regions. During our analysis we found that requiring a too high value for undershooting below a shell can be problematic and causes the program to terminate.

An explanation for this problem can be found by looking at a Kippenhahn diagram, which is shown in Fig. 3.2. Strong undershooting mixes unprocessed material down into the core. Thus the burning shell moves down, and can finally cause the He burning in the core to stop. This behaviour is most likely not physical.

The undershooting problem does not occur in all cases. The limiting undershooting value seems to depend mainly on the initial mass as well as metallicity. Especially, we can see a huge difference between the models with Milky Way (**MW**) and Large Magellanic Cloud (**LMC**) metallicities. While with MW abundances the shell moves down slightly until it becomes radiative, for LMC abundances it moves further down and thus is more unstable.

This difference finally goes back to differences in mass loss. Reducing the mass loss value of the MW model by a factor of 0.4 gives similar results as for the LMC. The more mass is lost, the shorter the H burning shell is convective. Thus high mass loss can prevent this instability.

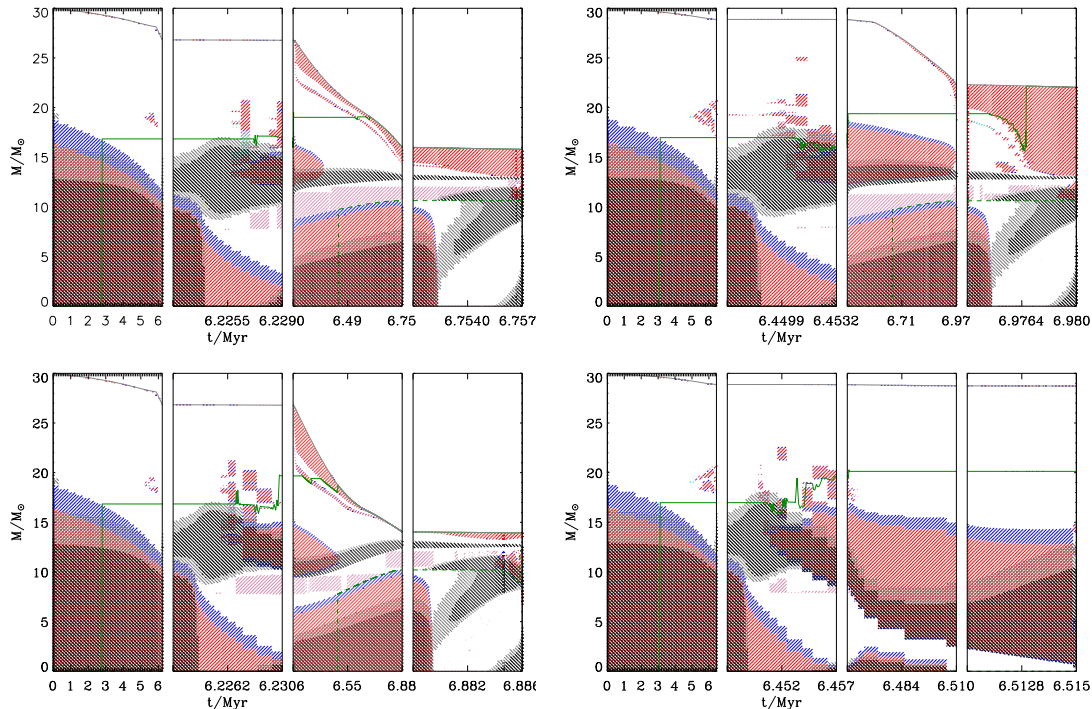


Figure 3.2: Kippenhahn diagrams to demonstrate the undershooting problem. Comparison of a non rotating $30M_{\odot}$ model with core and shell-overshooting parameter set to $\alpha_{over,core} = \alpha_{over,shell} = 0.335$, at MW (left), and LMC (right) metallicity. The shell-undershooting parameter is varied between $\alpha_{under} = 0.09$ (top), and $\alpha_{under} = 0.335$ (bottom). Different processes are indicated by different colors: **convection**, **overshooting**, **semiconvection**, **thermohaline**. burning ($> 10\text{erg/s}$), and burning ($> 100\text{erg/s}$). Lines indicate the total mass (**solid**), the He-core mass (**solid**), and the C-core mass (**dashed**). High undershooting at LMC metallicity causes the convective shell to move down, and the calculation to terminate.

Even though there is some difference in final masses, $\Delta M_f \approx 5M_{\odot}$ for the $30M_{\odot}$ model with MW abundances discussed, we completely neglect shell undershooting and also shell overshooting to avoid this problem.

3.3.3 Boundary Conditions

The atmospheric pressure applied in MESA is discussed in Sec. 2.3. As many approximations enter the derivation, MESA includes the parameter `Pextra_factor` to “manually” modify this quantity. Typical values should be on the order of $\mathcal{O}(1)$.

We found, that the choice of this parameter can affect the evolution already on the main sequence, depending on the MLT++ setting `gradT_excess_max_change`.

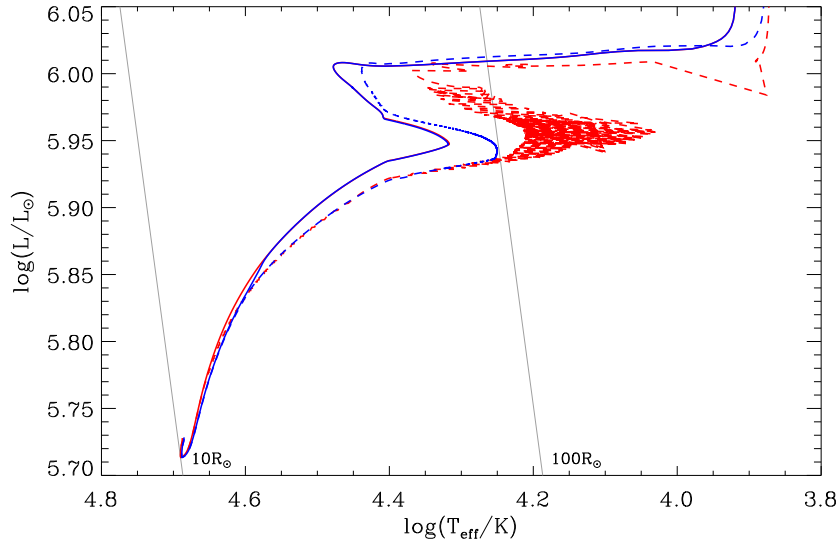


Figure 3.3: Comparison between different boundary conditions. Value of `Pextra_value` varied between 1 (dashed) and 2 (solid), and `gradT_max_change` varied between `-1` (meaning no limitation) and `0.001`. Depending on the choice of these parameters, the calculation can become unstable.

A default value is not set, whereas Keszthelyi (2015)² limit the changes `MLT++` can do, and set a value of `0.001`.

In Fig. 3.3 we compare these different possibilities. We start with a comparison of the calculations without `MLT++` limitations (dashed curves). Depending on the `Pextra_factor` setting, the curves separate. Already on the MS a critical Γ_e can be reached when we set a value for `Pextra_factor` of 1 which we see as instability close to the hook. This can be avoided by a higher value of 2. In addition, it slightly shifts the position of the hook by $\Delta \log T_{eff} \approx 0.1$.

Another way to avoid such an instability is setting `gradT_excess_max_change` to `0.001`. This also diminishes the differences between different `Pextra_factor` values.

In order to increase the stability of our calculations, we choose `Pextra_factor=2` and `gradT_excess_max_change=0.001`.

3.4 Comparison with Other Calculations

Various authors have calculated model grids consisting of massive stars, utilising different stellar evolution codes. Besides MESA, two very popular codes used for

²MESA inlist available at <https://doi.org/10.5281/zenodo.3250412>

such calculations are STERN and GENEC. In the following, we want to compare grids calculated with these two codes, and similar calculations we have performed with MESA.

3.4.1 Comparison with Ekström et al. (2012)

Physics

Ekström et al. (2012) use the GENEC code for their calculations, covering the evolution until late pre-supernova phases. The main difference to the MESA code is the advective treatment of the Eddington-Sweet circulations for angular momentum transport, and the second bi-stability jump that is missing in MESA. We use the parameters described in their original paper. In their calculations, an overshooting value of $\alpha_{over} = 0.1$ is adopted, where observations typically imply a higher overshooting value (Castro et al. 2014, see Sec. 2.2.4).

Groh et al. (2014) analyse a non rotating $60M_{\odot}$ model out of this grid in more detail, such that we can use this model as a reasonable reference point. A huge mass loss originates from crossing the second bi-stability jump at $T_{eff} \approx 15$ kK at the end of the main sequence. The mass loss increases by a factor of 10.

In addition, all of their published evolutionary track³ are based on a temperature definition corrected for the optical depth of the wind, as stated by Groh et al. (2014). The track is shifted towards lower temperatures, especially for the later phases. Thus we can only reproduce general trends for these later phases.

Results

The main sequence evolution has been discussed by Ferraro (2020). We can see that the main sequence for our non rotating models, shown in Fig. 3.4, is very similar to that of the Ekström et al. (2012) models. Also the hook is at a similar position.

The evolution after the hook seems to be similar for smaller masses. The bump after the hook is too small to be observed. Its origin might be related to slight differences in the treatment of the convective boundary.

For higher initial masses, the differences get bigger. The stars calculated using GENEC lose more mass than predicted by MESA. In order to get closer to the solution, we have to include the second bi-stability jump with an increase in mass loss by a factor of 10 when crossing the jump. The resulting tracks are presented

³All tracks are available at <http://obswww.unige.ch/~mowlavi/evol/denseGrids/>

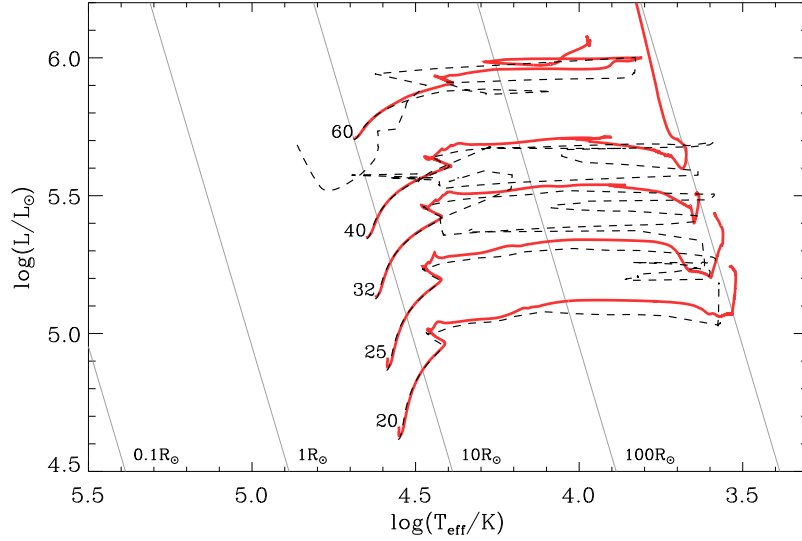


Figure 3.4: Comparison between non-rotating models calculated by Ekström et al. (2012) (dashed) and similar MESA calculations (solid). The initial mass is indicated at each track. Huge differences, especially for the $60M_{\odot}$ model, can be seen.

in Fig. 3.5. For the $60M_{\odot}$ model the mass loss is still too low. While our model ends as RSG, the model calculated by Ekström et al. continues to the blue and ends its life as WR star.

As already discussed, for the GENEC models a very high mass loss occurs when crossing the second bi-stability jump on the main sequence. However, the main sequence for our model does not reach the corresponding temperature of $\log T_{eff} = 4.2$ ($T_{eff} \approx 15$ kK).

A longer extent of the main sequence was observed for models set up and calculated by Ferraro (2020), such that we should be able to reproduce this feature in MESA. Two parameters can account for that difference. The first is `Pextra_factor`, which was 2 in our models. A value of 1 can prolong the main sequence by $\Delta \log T_{eff} \approx 0.1$ as discussed in Sec. 3.3.3, which is, however, not sufficient. The timestep setting based on the error in energy conservation made by the solver⁴, has an even larger impact. This purely numerical parameter had been set for our calculations, whereas it was not set by Ferraro (2020).

Removing it from our settings, we can get close to the solution found by Ekström et al. (2012) for non-rotating models, as shown in Fig. 3.6. For the major part of

⁴MESA parameter `limit_for_rel_error_in_energy_conservation`. In our calculation, it has been set to 10^{-4} .

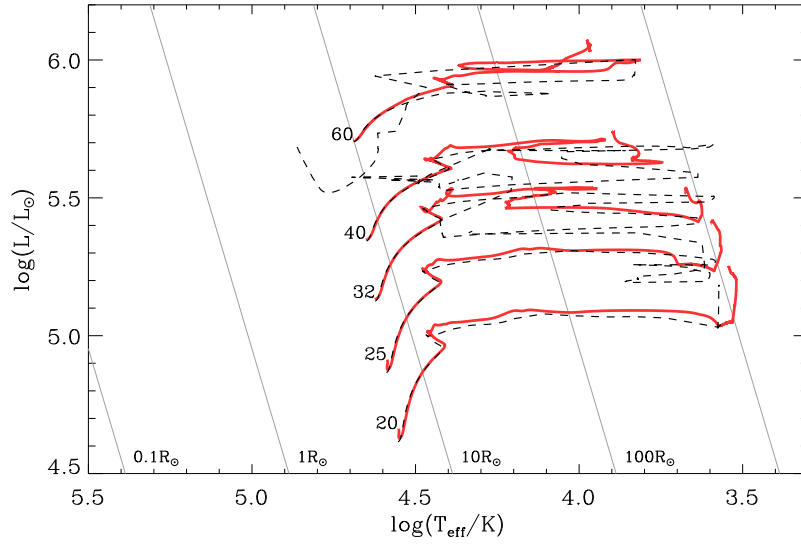


Figure 3.5: As Fig. 3.4, but with the second bi-stability jump included. Especially the $60M_{\odot}$ model is still different.

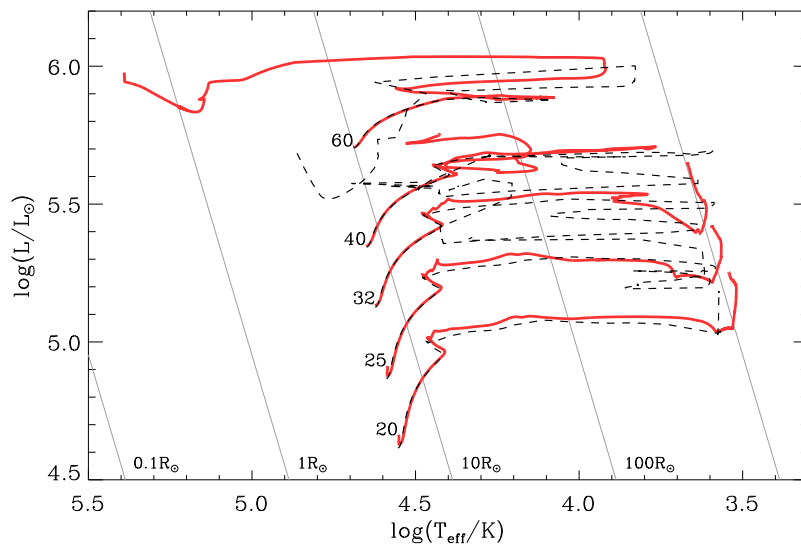


Figure 3.6: As Fig. 3.5, but with timestep setting relaxed. This way, the MS of the $60M_{\odot}$ model has a longer extent and crosses the second bi-stability jump.

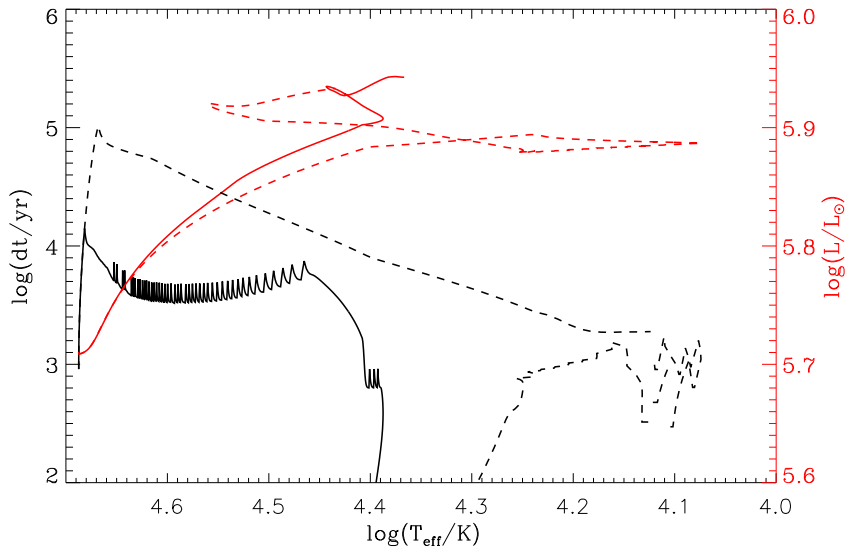


Figure 3.7: Comparison between the timestep (black curves) on the MS of our non-rotating $60M_{\odot}$ model with the timestep constraint described in the text (solid), and without it (dashed). As a reference point, the MS track is shown (red curves). Depending on the timestep setting, there can be a huge difference in the actual timesteps used for the calculation.

the MS, the timestep is limited by this setting, as can be inferred from Fig. 3.7, and is up to one order of magnitude lower. This leads to a separation of the MS which grows linearly. The difference finally results in a different position of the hook. For the hook itself, the timestep is similar in both cases, indicating that it is not influenced directly by this timestep, but rather by the different starting point.

In general, we would expect that tighter timestep constraints result in a higher precision. At least for this comparison though, relaxing this condition seems to be the better choice (nevertheless it is not clear which is the more physical solution).

We can summarise, that the behaviour of the $60M_{\odot}$ model is highly parameter dependent. In addition, the second bi-stability jump on the main sequence is most likely not physical, at least with respect to its position, and the enormous increase of mass loss rate (see Sec. 2.6.1). In this case Ekström et al. (2012) would overestimate the total mass being lost by a factor of ≈ 2 .

For rotating models the transport of angular momentum by the Eddington-Sweet-circulations plays a major role. It can change the rotational structure, and thus can affect indirectly also the transport of elements by rotational instabilities. As the treatment is different for the two codes, we can see huge differences

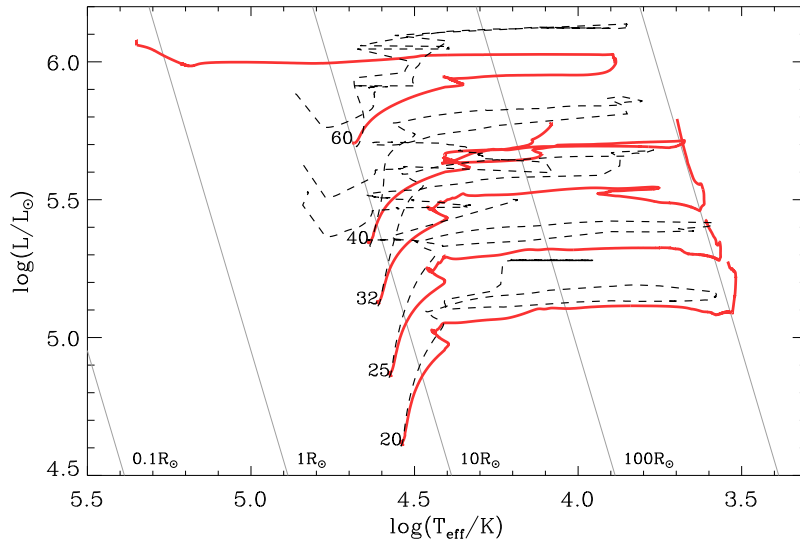


Figure 3.8: Comparison between models calculated by Ekström et al. (2012) (dashed) and similar MESA calculations (solid), rotating with $\omega = 0.4\omega_{crit}$. The initial mass is indicated at each track. Already the MS evolution shows huge differences.

in Fig. 3.8. Already the main sequence evolution is different for our models, as discussed by Keszthelyi (2015). Ferraro (2020) showed that increasing the efficiency by a factor of 10 allows to reproduce the post-main sequence. However, he increased the efficiency both for angular momentum, and chemical transport. In his calculation, the main sequence is different in all cases, indicating that differences between advective and diffusive angular momentum transport can not be expressed in a simple scaling factor. This is consistent with the result of Groh et al. (2019), who also attribute the differences of rotating models in GENEC and MESA in terms of meridional circulations.

3.4.2 Comparison with Brott et al. (2011)

Physics

This grid of stellar models has been calculated with the STERN code. The calculation covers the main sequence evolution and central helium burning.

The treatment of the physical processes is very similar to the descriptions used by MESA. Especially, both mixing and angular momentum transport are treated as diffusive processes.

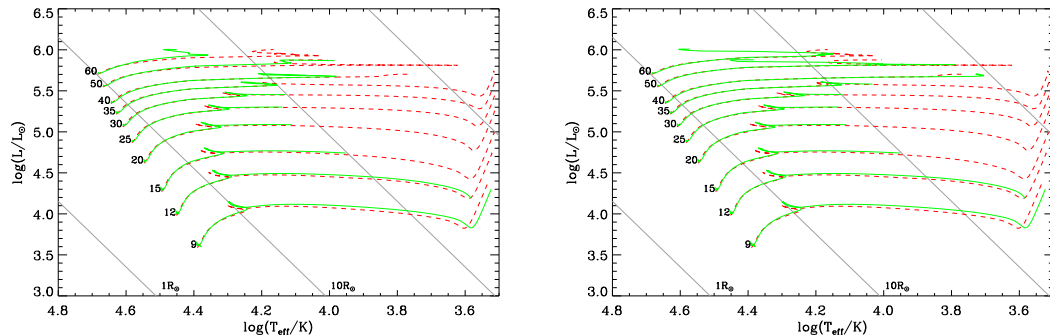


Figure 3.9: Comparison between non-rotating models calculated by Brott et al. (2011) (dashed) and similar MESA calculations (solid). The initial mass is indicated at each track. Two different setups are compared, one with our default parameters (left), and one with the timestep setting `limit_for_rel_error_in_energy_conservation` deactivated (right). Differences between the models are small. However, the hook of the $60M_{\odot}$ model is highly parameter dependent.

The parameters can be found in Brott et al. (2011). As the mass loss rates are calculated based on the iron abundances, we have to set the metallicity used for opacity calculations, Z_{base}^5 , to 0.014 while setting $Z = 0.0088$. We apply the Dutch mass loss scheme. However, Brott et al. include a change from the de Jager, Nieuwenhuijzen, and van der Hucht (1988) rates to the rates by Nieuwenhuijzen and de Jager (1990) if the latter are higher. They argue that this naturally includes the second bi-stability jump at $T_{\text{eff}} \approx 12.5$ kK.

Results

Comparing the main sequence of non-rotating models shown in Fig. 3.9, we see an overall excellent agreement. For lower masses, changes are below what would be measurable. For the higher masses, we again observe a shift in the position of the hook. As in the comparison to the results of Ekström et al. (2012) in Sec. 3.4.1, this disagreement can be reduced by changing the timestep settings. The position of this hook for high masses is again highly parameter dependent!

The post-MS evolution shows further differences, which might be related to the different treatment of mass loss. At first, Brott et al. use the iron abundances for wind scaling, while we use the total metallicity. The correction by setting Z_{base} can not fully compensate for the differences. In addition, Brott et al. include a

⁵This parameter is used for opacity calculations only until the metallicity Z exceeds this value.

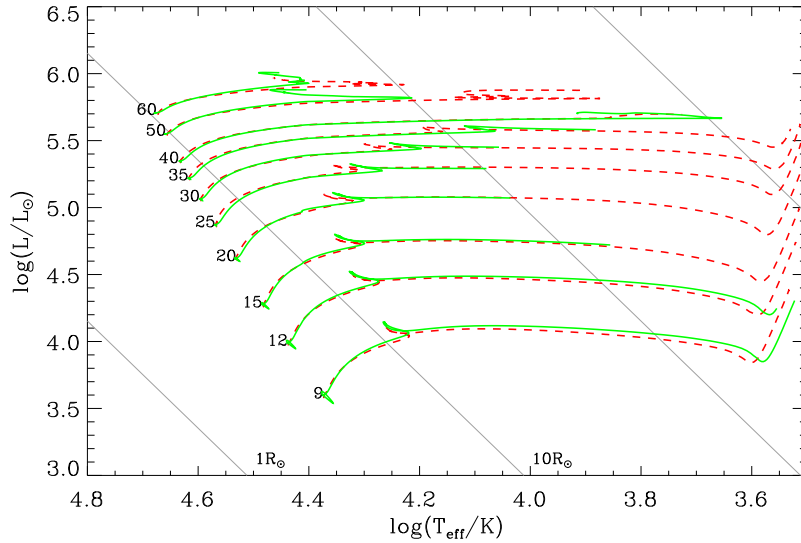


Figure 3.10: Comparison between rotating models calculated by Brott et al. (2011) (dashed) and similar MESA calculations (solid) with $v_{init} \approx 300\text{km/s}$. The initial mass is indicated at each track. As expected, the differences are similar to the non-rotating models.

description of the second bi-stability jump. As argued in the previous section, this most likely overestimates the mass loss.

The rotating models presented in Fig. 3.10 do not show other differences than the non-rotating ones, which is to be expected, since the treatment of rotation and the rotational instabilities in the STERN code is very similar to the implementation in MESA.

3.4.3 Comparison between evolutionary tracks of Brott et al. (2011) and Ekström et al. (2012)

There are significant differences between the tracks calculated by Brott et al. (2011) with the STERN code and Ekström et al. (2012) with GENEC. The tracks calculated by Brott et al. mostly look simpler than the ones by Ekström et al., as they have less blue loops. The differences can be attributed to four main reasons.

At first, Brott et al. utilise the Ledoux criterion for calculations of the convective boundary, while Ekström et al. apply the Schwarzschild criterion. This leads to a μ -barrier for the Brott et al. models, which thus have a lower luminosity. In addition, the treatment of angular momentum transport by meridional circulations is different, as described in the previous sections. The evolution of the surface

rotational velocity is drastically influenced by the presence of magnetic fields, which are only used in the models calculated by Brott et al. Finally, the overshooting value is drastically different.

An enlightening summary of the differences between stellar evolution codes has been provided by Keszthelyi (2015).

3.5 Remnant Linking

Our calculations include the evolution from the ZAMS up to central carbon-exhaustion. From then on, the timescales are very short, the internal structure and especially the helium- and carbon-core masses do not change. Thus, the final model of our calculation is sufficient to make predictions for the final remnant.

We assume the remnant properties are purely based on the final helium and carbon core masses M_{He} and M_{CO} as well as the final mass M_f before the explosion. The explosion type is mainly based on the mass of the hydrogen-envelope M_H . In the following we will give a short overview about explosion and remnant types. Finally, we will provide the two formalisms used to link the final structure to a remnant mass.

3.5.1 Explosion Types

Massive stars end their life with a supernova (**SN**) explosion. The SN is characterised by its spectral appearance. Especially, the H and He lines are important, as these elements are lost at first by stellar winds. If hydrogen lines are present in the spectrum, we define the SN as type II. If no H is present, the star explodes as type I SN.

Depending on the spectral evolution and exact shape of the spectrum, further distinctions can be made. We use the limits presented in table 3.1, taken from Heger et al. (2003). Further information about SN classification can be found in the book by Maeder (2009).

For very massive stars, there exist other types of SNe, such as the so-called pair instability SN (**PISN**). As we only calculate models up to $M_i = 60M_\odot$, they are not important for our work. Other possible mechanisms that lead to a SN explosion can occur in binary systems that host at least one white dwarf (SN type Ia).

M_H/M_\odot	SN type
≥ 2	IIP
≤ 2	IIL/b
0	Ib/c

Table 3.1: Supernova type depending on the mass of the hydrogen-rich envelope M_H , following Heger et al. (2003).

3.5.2 Remnant Types

While low and intermediate mass stars end their life as white dwarfs (**WDs**), electron degeneracy is not sufficient to stabilise the remnant produced by high mass stars. The upper mass limit for WDs is known as Chandrasekhar mass as it was first derived by Chandrasekhar (1931). If the mass (of a massive star) is not too high, neutron degeneracy can stabilise the object and a neutron-star (**NS**) forms. If the mass is even higher, a black hole (**BH**) is produced. This can contain either only a part of the progenitor mass (fallback BH), or the total mass of it (direct BH), if the iron core mass is sufficiently high. While there is no theoretical upper mass limit for their stability, stellar evolution calculations (for single stars) predict an upper mass limit for black holes of $\mathcal{O}(50) M_\odot$, at least at solar metallicity (Heger et al. 2003, Belczynski et al. 2010, Spera, Mapelli, and Bressan 2015). Very massive stars in a certain mass range end their life with a pair-instability SN, disrupt completely, and thus leave no remnant behind.

The exact limiting masses are still under discussion and may depend on the final rotation rates (Chamel et al. 2013, Rezzolla, Most, and Weih 2018). However, the uncertainty is negligible for our simulations. In our work we use the limits described by Belczynski et al. (2008) to distinguish between different remnants.

Remnants with masses lower than $M_{rem} = 1.4M_\odot$ form white dwarfs. For masses in the range $1.4 \dots 2.5M_\odot$, the remnant collapses into a neutron star. Even higher masses lead to black holes.

As discussed already, these remnant masses can be calculated from the final mass and the core masses. In the following, we describe the different options, how to link the progenitor-properties to the final remnant mass.

3.5.3 Woosley-Formalism

The first scheme is based on the work by Woosley, Heger, and Weaver (2002). They state that the remnant properties depend solely on the final helium-core

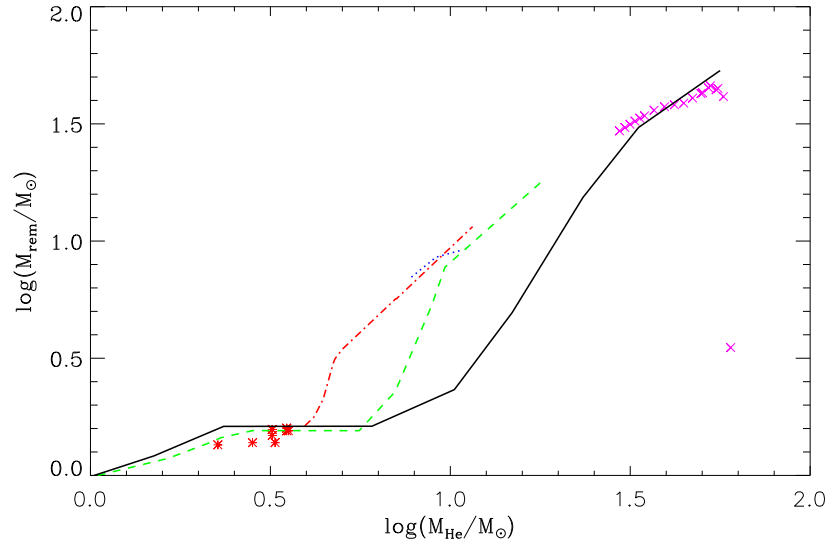


Figure 3.11: Helium-core to remnant-mass relation obtained from Woosley, Heger, and Weaver (2002). We differentiate as follows: zero-metallicity (solid) and solar metallicity, where we further differentiate between RSGs (dashed) and WR stars within the high mass loss scenario (dashed-dotted) and the low mass loss scenario (dotted). Additional data-points from Woosley, Langer, and Weaver (1995) (asterisks) and Woosley (2019) (x-symbols) are shown.

mass.

We use Figs. 12 and 16 from Woosley, Heger, and Weaver (2002) to read out the data, and find the helium-core to final mass relation shown in Fig. 3.11. There are different relations depending on metallicity and the internal structure.

The green curve follows the relation for stars at solar metallicity which end their life as supergiants. For stars that end their life as WR stars, the red and blue lines need to be considered. These are the two different scenarios described by Woosley, Heger, and Weaver (2002), depending on the assumptions for Wolf-Rayet mass loss rates. The higher mass loss scenario (red) provides data for lower helium core masses than the scenario assuming lower mass loss rates. Nevertheless, in the range of helium core masses where both relations can be used they coincide very well. For all Wolf-Rayet stars that lost their hydrogen-rich envelope, we use the mean value of the two relations for all helium core masses where both can be applied, and only the relation provided by the high mass loss rate scenario otherwise. The difference to the relation for RSGs can be explained by changes of the internal structure by mass loss.

As the evolution of stars with LMC abundances is more similar to those with

MW abundances compared to the zero metallicity case, we use these relations for both metallicities.

The black curve is valid for zero metallicity⁶. The difference to the solar metallicity environment can be explained by strong differences in the internal structure as no mass loss is present, and by the fact that stars at lower metallicity are more compact. Another explanation could be the lack of catalysts (at least in the early phases of evolution).

Woosley, Langer, and Weaver (1995) and Woosley (2019) calculated more detailed explosion models, shown as asterisks in this plot. They overlap very well with the relations we found from Woosley, Heger, and Weaver (2002). The highest mass model of Woosley (2019) has a very low remnant mass which can be explained by complete disruption due to a PISN. However, none of our models reached such a high helium core mass.

As we use, regarding specific aspects, somewhat different physics for the evolution, stars might have higher He core masses than the maximum masses presented by Woosley, Heger, and Weaver (2002). In this case we assume that the whole helium core mass is included in the remnant.

3.5.4 Belczynski-Formalism

As already Woosley, Heger, and Weaver (2002) argue, the carbon core should be an even better indicator of the remnant properties than the helium core mass. A linking-scheme based on the carbon core mass is described by Belczynski et al. (2008).

To find the remnant mass one has to follow two steps. The first is to find the iron core mass. In general, one could continue the stellar evolution calculation to a state just before core collapse to obtain it directly. Nevertheless, as the final timescales get very short, and thus the time needed for the calculations would increase drastically, we use the simple idea described by Belczynski et al. (2008), who performed fits for models calculated by Timmes, Woosley, and Weaver (1996).

⁶Woosley, Heger, and Weaver (2002) assume that zero metallicity models evolve without mass loss.

The iron core mass can be calculated via

$$M_{FeNi} = \begin{cases} 1.5M_{\odot} & M_{CO} < 4.82M_{\odot} \\ 2.11M_{\odot} & 4.82M_{\odot} \leq M_{CO} < 6.31M_{\odot} \\ 0.69M_{CO} - 2.26M_{\odot} & 6.31M_{\odot} \leq M_{CO} < 6.75M_{\odot} \\ 0.37M_{CO} - 0.07M_{\odot} & 6.75M_{\odot} \leq M_{CO}. \end{cases} \quad (3.1)$$

Even though this description was obtained for solar metallicity, Belczynski et al. argue that it can be used for a wide range of metallicities $Z \approx 10^{-4} \dots 0.3$ and even is a good approximation at zero metallicity. We use this scheme not only for MW and LMC abundances but also for a very low metallicity $Z = 10^{-5}$.

Timmes, Woosley, and Weaver (1996) explain the jump from $1.5M_{\odot}$ to $2.11M_{\odot}$ by a differences in core C burning. While smaller mass stars have convective energy transport during central carbon burning, the core becomes radiative for higher mass stars as discussed in Sec. 3.2.2.

In a second step, we can calculate the baryonic remnant mass by using the iron core mass:

$$M_{rem} = \begin{cases} M_{FeNi} & M_{CO} \leq 5M_{\odot} \\ M_{FeNi} + \frac{M_{CO} - 5M_{\odot}}{(7.6 - 5)M_{\odot}} (M_f - M_{FeNi}) & 5M_{\odot} < M_{CO} < 7.6M_{\odot} \\ M_f & 7.6M_{\odot} \leq M_{CO}. \end{cases} \quad (3.2)$$

The pre-factor in the second case describes partial fallback. For higher masses we have a direct collapse, and, as above, the full progenitor mass is included in the final remnant.

The models calculated by Timmes, Woosley, and Weaver cover initial masses $M_i = 10M_{\odot} \dots 40M_{\odot}$. As for higher masses the iron core mass increases further, and the remnant mass is determined by the final mass, the formalism can be extended to higher masses. The only upper mass limit is given by the mass where a pair instability occurs, which we do not reach in our models.

3.5.5 Gravitational Mass

The mass given by the previous relations is the baryonic mass of the remnant. As neutron stars and black holes are very compact, their gravitational remnant mass is smaller.

For micro-lensing observations (see Chpt.1) the gravitational mass, and not the baryonic one is important. We use the relations provided by Belczynski et al. (2008, their Eqn. 3 and 4).

For NSs the gravitational mass can be calculated via

$$M_{rem,grav} = \sqrt{\left(\frac{M_{\odot}}{2 \cdot 0.075}\right)^2 + M_{rem,bar} \frac{M_{\odot}}{0.075}} - \frac{M_{\odot}}{2 \cdot 0.075}. \quad (3.3)$$

For BHs a simple reduction by a factor of 0.9,

$$M_{rem,grav} = 0.9M_{rem,bar}, \quad (3.4)$$

describes the conversion.

4 Evolutionary Model Grids

4.1 Physical Parameters

Our grid of models consist of eight different masses ranging from $10M_{\odot}$ to $60M_{\odot}$, as well as different rotational velocities. We chose a tighter mass spacing for stars $10M_{\odot} \leq M \leq 30M_{\odot}$ in order to have a better resolution in logarithmic space and as we expect many transitions between different remnant types to occur in this region.

4.1.1 Standard Grid

Our standard grid includes the following values:

- Masses: $M_i/M_{\odot} = 10, 15, 20, 25, 30, 40, 50, 60$,
- Rotational velocities: $\Omega/\Omega_{crit} = 0, 0.2, 0.4$.

As discussed in Sec. 2.2, the best choice for the convective boundary criterion is still under discussion. In order to study the uncertainties resulting from this choice, we include both, the Ledoux and the Schwarzschild criterion, in our grid. If the Ledoux criterion is employed for the calculations of the convective boundary, we adopt semiconvection with $\alpha_{semi} = 1.0$. Overshooting above the convective core is included with $\alpha_{over} = 0.335$ for all central burning phases.

Rotational mixing is implemented with an efficiency $\alpha_{mix} = 1/30$, and effects of the composition gradient are reduced by $f_{\mu} = 0.05$. Out of the instabilities described in section 2.4.2, we include the secular shear instability, the Solberg-Hoiland instability, Eddington-Sweet circulations, and the Goldreich-Schubert-Fricke instability. Effects of the viscosity as well as dynamical shear are neglected.

As not all massive stars host magnetic fields, and as the implementation is highly uncertain, we include models with and without a Spruit-Tayler dynamo being active.

Mass loss is implemented following Sec. 2.6.4 in the Dutch scheme.

4.1.2 Additional Grids

For most of the above parameters, in particular the mass loss rates, the corresponding values are still under debate. In order to study their influence and the uncertainties originating from them, we calculate different grids where these parameters are varied.

We assign the following numbers to these grids:

1. Standard grid.
2. Increased core overshooting following Castro et al. (2014), $\alpha_{over} = 0.5$.
3. Wind corrected towards a probably more realistic description, in several steps. Position of the bi-stability jump $T_{eff,jump}$ and corrected wind scaling:
 - (a) total mass loss scaled down by factor 0.4¹, $T_{eff,jump} = 25$ kK
 - (b) total mass loss scaled down by factor 0.4, $T_{eff,jump} = 20$ kK
 - (c) only Vink mass loss scaled down by 0.4², $T_{eff,jump} = 20$ kK
 - (d) as before, but including metallicity scaling for de Jager mass loss rates (late type supergiants)
4. Mixing coefficients f_c, f_μ varied drastically according to Keszthelyi et al. (2020, in prep.). The changes are more important, when the mixing efficiency is increased, as it favours quasi chemically homogeneous evolution for more models. Thus, we increased f_c by a factor of 10, and decreased f_μ by a factor of 5.

4.1.3 Abundances

Our analysis includes calculations in three different environments. In order to reproduce other grids, and because of rich observational data, calculations with Milky Way (**MW**) and Large Magellanic Cloud (**LMC**) abundances are performed. In addition, grids at very low metallicity $Z = 10^{-5}$ (**lowZ**) are

¹MESA parameter `Dutch_scaling_factor`

²MESA parameter `Vink_scaling_factor`. By default, this is not used when the Dutch scheme is applied. However, we made this setting accessible in our `run_star_extras.f` (see App. A.5.1)

evaluated. All metallicities Z including the initial Helium abundances Y are summarised in table 4.1.

The initial abundances of individual elements vary depending on the environment. For MW metallicity, we use the values provided by Asplund et al. (2009), and corrected by Nieva and Przybilla (2012) and Przybilla et al. (2013). At low Z , the exact abundances play a minor role, as they are very small in any case. We apply the same composition as for MW metallicity, scaled down according to the metallicity difference. For the LMC we follow the approach of Brott et al. (2011): The Asplund, Grevesse, and Sauval (2005) abundances are reduced by 0.4 dex except for C, N, O, Mg, Si, and Fe where we use the values from Brott et al. (2011), their table 1.

	X	Y	Z
MW	0.715	0.271	0.014
LMC	0.7391	0.2562	0.0047
low Z	0.75229	0.2477	10^{-5}

Table 4.1: Initial hydrogen abundances, helium abundances, and metallicities of our models. For references, see text.

4.2 Numerical Parameters

Some critical parameters have already been discussed in Sec. 3.3. The full set of numerical parameters can be found in our inlists³ attached in Sec. A.4.

However, we sometimes changed these settings, when models ran into timestep issues with the default parameters. A major problem were density inversions, as described in Sec. 2.2.5. We tried varying different parameters, where the following was the best compromise between a physical choice of the parameters and avoiding problems. As a first step, the timestep settings that force a better resolution of the burning phase were relaxed. This often helped, as the calculation just “jumped” over the problematic moment (compare also Sec. 3.4.1).

If the calculation still reached very small timesteps, we changed the `MLT_option` to the scheme described by Böhm-Vitense (1958) or adjusted the `MLT++` options. Both could help to increase the convective efficiency in the envelope and thus also avoid the density inversion.

³The inlists are the files containing the data necessary for a MESA run. Physical and numerical parameters can be varied, as already described.

Different checks clarified that these changes do not alter the results drastically, the differences are much smaller than differences between the grids.

4.3 Technical Aspects

Our basic grid consists of 96 models, as described in the previous section. In the following, we provide a short overview about typical run-times, and the memory usage. The exact numbers depend on the exact timestep and grid settings, as well as on the assumptions about the physics of the model.

4.3.1 Runtime

MESA is designed to make efficient use of a multi-core architecture. At first, it is programmed in a thread save way, such that it can use parallelisation inside a single run. On our machine, we used 16 threads⁴, which we found as an optimum number, as discussed in App. A.6. A single program takes an average wall-clock runtime of ≈ 50 min to calculate from the pre-MS until carbon exhaustion.

In addition to executing a single run with multiple threads, several instances of MESA can be run in parallel. Our machine had a total of 160 CPUs available. We had to keep the maximum number of threads below this number, as virtual threading drastically slows down the run. In order to keep some threads free for our analysis, we executed a maximum of nine models in parallel. As our program execution is split into different parts depending on the evolutionary phase, and rotation is only set from the ZAMS on, we can reduce the number of pre-MS models that has to be calculated. However, these calculations only make up a small fraction of the runtime. It took $\mathcal{O}(10)$ hours for the calculation of a single grid to finish.

4.3.2 RAM Usage

In addition to the CPUs, the number of models that can be calculated in parallel is limited by the available RAM. A single run requires $\lesssim 7$ GB. If the available RAM is exceeded, MESA can run into timestep problems, and the program terminates. As we had 200 GB of RAM available, this was not a problem for us. However, for earlier tries on other machines this was a limiting factor.

⁴Linux bash variable `OMP_NUM_THREADS`

4.3.3 Final Storage

Besides the MESA program, that already occupies 36 GB⁵, there is also the memory space for our mesa program and the inlists, which is only 54 MB. Also the output of the run has to be saved. The default way, how this is done in MESA, is to save the output into a history file for core and surface data, and profile files, which contain data at a single timestep along the radial coordinate. We chose to save the core and surface data at every timestep⁶, and a profile every tenth step⁷. These data occupy $\approx 1.5 \dots 2$ GB for a single model. In order to analyse the data, we read them into IDL⁸ binary files, which have an average size of only $\approx 200 \dots 300$ MB. To reduce the necessary space even further, we saved the most important core and surface data, as well as a final profile, into an ASCII file of only $\mathcal{O}(1)$ MB.

⁵Split into 1.8 GB for the MESAsdk, and 34 GB for the main program.

⁶MESA parameter `history_interval` set to 1

⁷MESA parameter `profile_interval` set to 10

⁸Interactive Data Language (**IDL**) is a programming language, used mainly for data analysis. We used it to analyse the output. How we analyse the data is described further in App. B.

5 Evolutionary Tracks and Core Masses

In the following, we analyse the outcome of our stellar evolution calculations. As the core and final masses are most relevant to link from the progenitor to the remnant, we will focus on their analysis. In addition, a deeper understanding can be gained from analysing the evolutionary tracks in the Hertzsprung-Russel diagram. These can also be used to compare our results to observations of RSGs, which are a reliable tracer of the quality of the models. Subsequently, we study the systematic effects of rotation, magnetic fields, and the choice of the convective boundary criterion.

The HRDs comparing all models from our calculations are shown in Figs. 5.12 to 5.14. Enlarged versions of our plots for the standard grids are shown in Figs. 5.1 to 5.3. The core and final masses are compared more quantitatively in Figs. 5.4 and 5.5.

5.1 Position of RSGs

As explained already in Sec. 3.2.2, stars with smaller masses tend to explode as RSGs. There exist various observations of RSGs at different metallicities. A large survey has been carried out by P. Massey in various publications. We compare the RSGs from Massey and Olsen (2003) at LMC abundances to our corresponding calculations. In addition, we compare with observations by Levesque et al. (2005) of RSGs at MW metallicity.

RSGs are located at a metallicity dependent, and approximately constant effective temperature, as they evolve along the Hayashi line. Indeed, in Figs. 5.1, and 5.2 we can see that this is true both for the observed RSGs, and for our calculations. In addition, we find an overall excellent agreement at LMC metallicity, while at MW abundances, we note a small difference, potentially

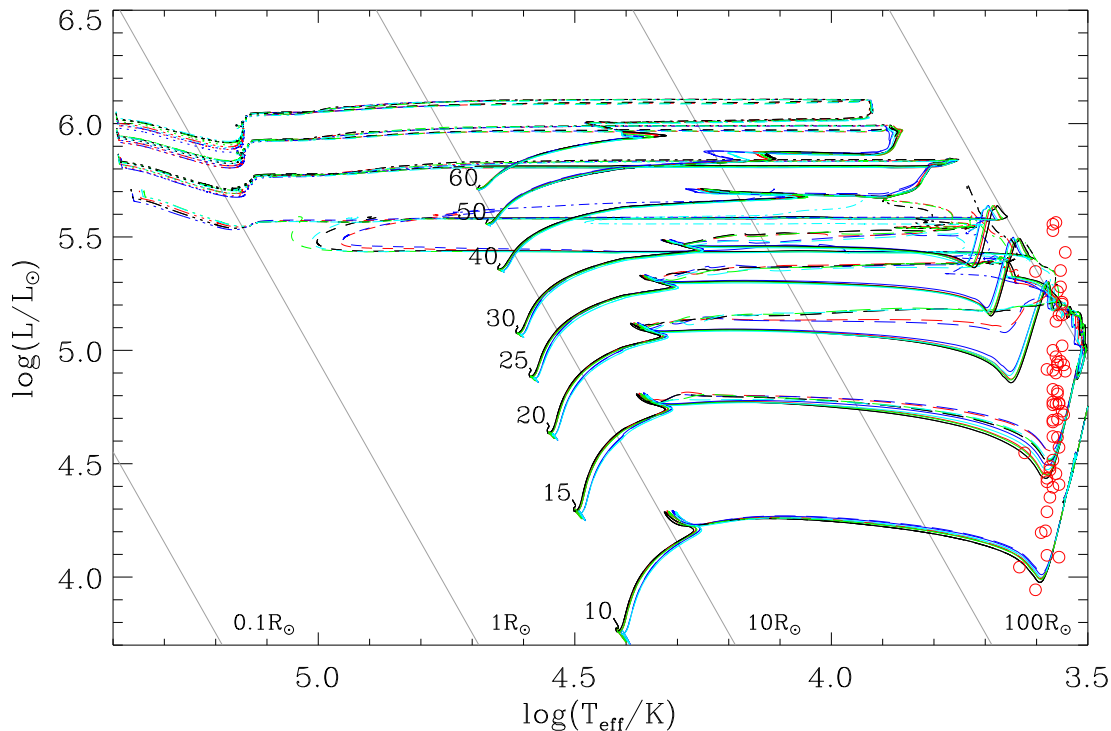


Figure 5.1: Hertzsprung-Russell diagrams of all models with MW metallicity in the standard grid. Different colors indicate a combination of rotation rates, and if the Spruit-Tayler dynamo (ST) is applied or not. The H surface abundances, and the convective boundary criterion are indicated by the choice of the linestyle.

Ω/Ω_{crit}	ST on	off	H surface abundance	Ledoux	Schwarzschild
0		black	> 60%	solid	long dashed
0.2	red	green	10% – 60%	dashed	dashed dotted
0.4	blue	turquoise	< 10%	dashed dotdot	dotted

RSGs from the MW (Levesque et al. 2005) are indicated as red circles. See text for further discussion.

related to the metallicity. Levesque et al. (2005) find an excellent agreement with the tracks calculated by Meynet and Maeder (2003), where they adopt $Z_{\odot} = 0.02^1$. In contrast, we assume $Z_{\odot} = 0.014$, and thus observe a shift of the RSGs to lower effective temperatures, consistent with the findings by Levesque et al. (2006).

Also for higher masses, $M_i \geq 25M_{\odot}$, there are some differences, mainly noticeable for LMC metallicity. These models do not reach the corresponding temperature, but evolve back to the blue already at higher effective temperatures and become BSGs or WR stars. Massey and Olsen (2003) suggest that this

¹Even though this value seems to be correct for the sample of RSGs observed by Levesque et al. (2005), the solar metallicity is most likely smaller.

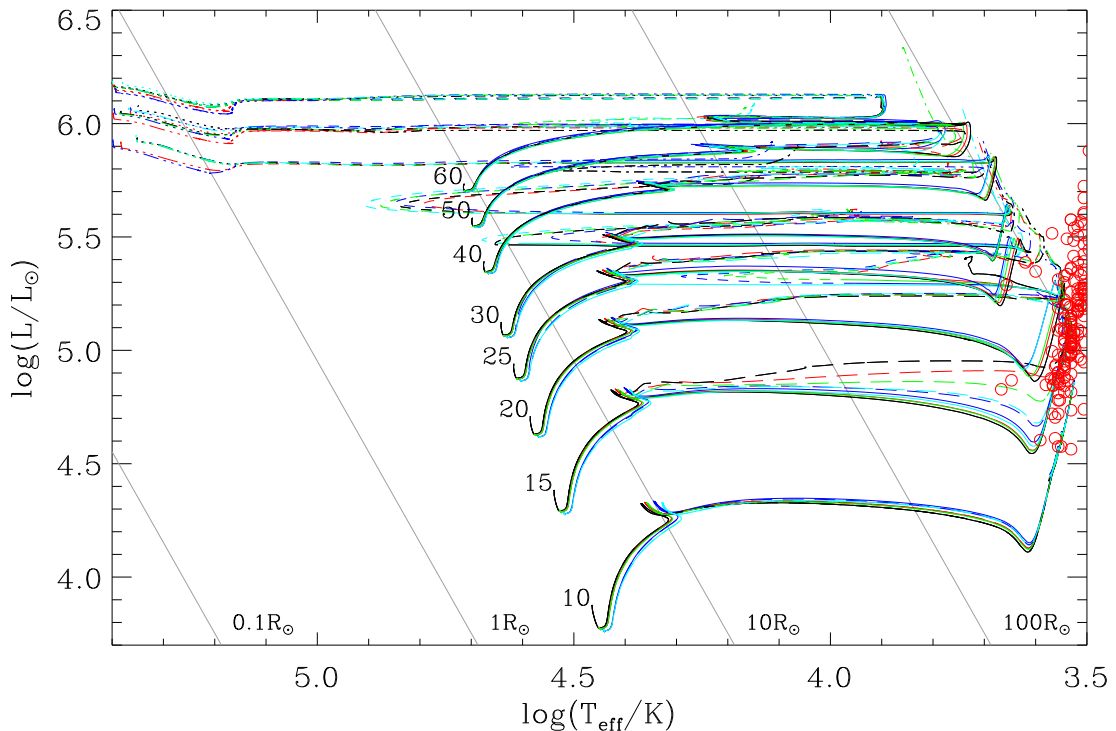


Figure 5.2: As Fig. 5.1, but for LMC metallicity. RSGs from the LMC (Massey and Olsen 2003) are indicated as red circles.

difference might be reduced by decreasing the mass loss. We could not verify this from our tests; the tracks calculated assuming an overall reduced mass loss and corrected jump temperature (grid 3b), decreasing the mass loss even further, did not show a strong effect (compare Figs. 5.12d and 5.13d). However, there is only a small number of such stars at higher luminosity, and a more detailed analysis of them, similar to the work of Massey and Evans (2016), could reveal an explanation.

5.2 Systematic Effects

Already within a single grid we include uncertainties about the convective boundary criterion, magnetic fields, and different rotational velocities. In the following, we want to discuss the systematic effects of these parameters. In Figs. 5.4 and 5.5, we show the differences in final masses, ΔM_f , and core masses, ΔM_{He} and ΔM_{CO} , for these three parameters.

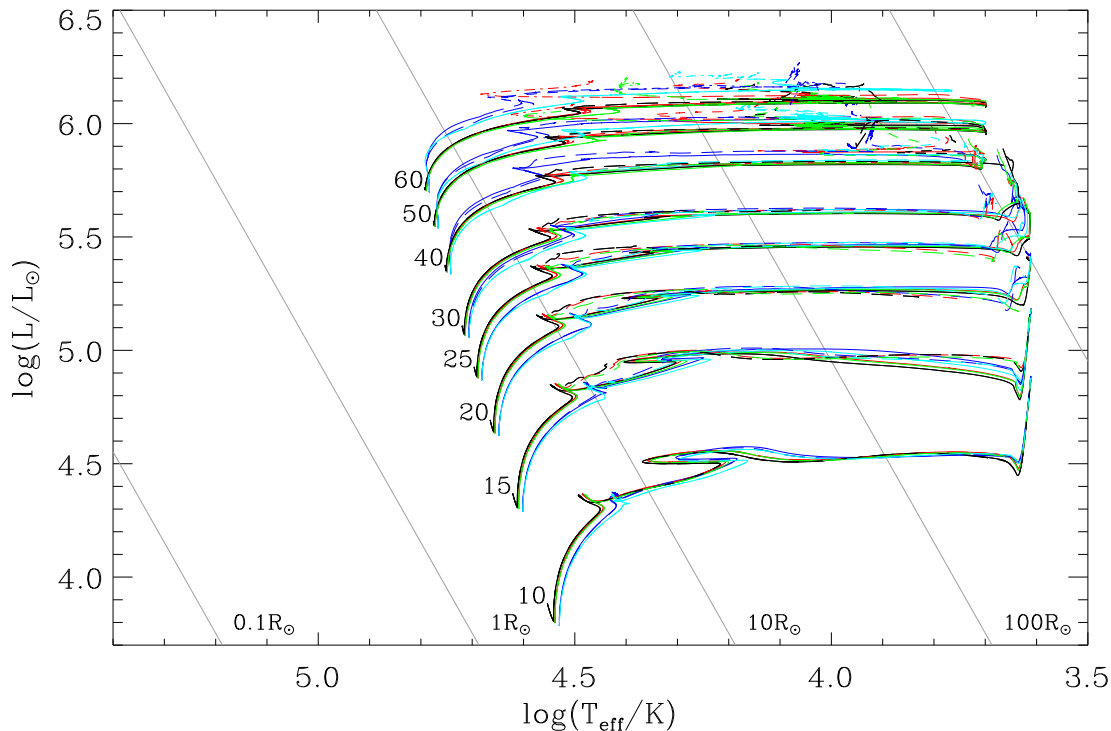
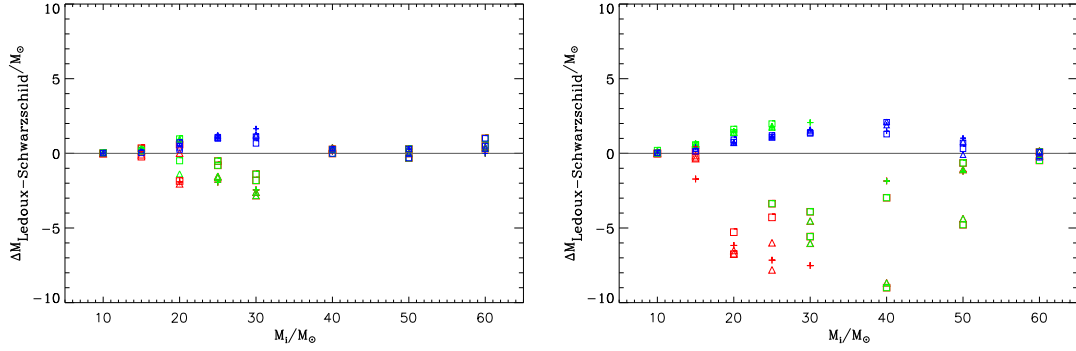


Figure 5.3: As Fig. 5.1, but for low Z .

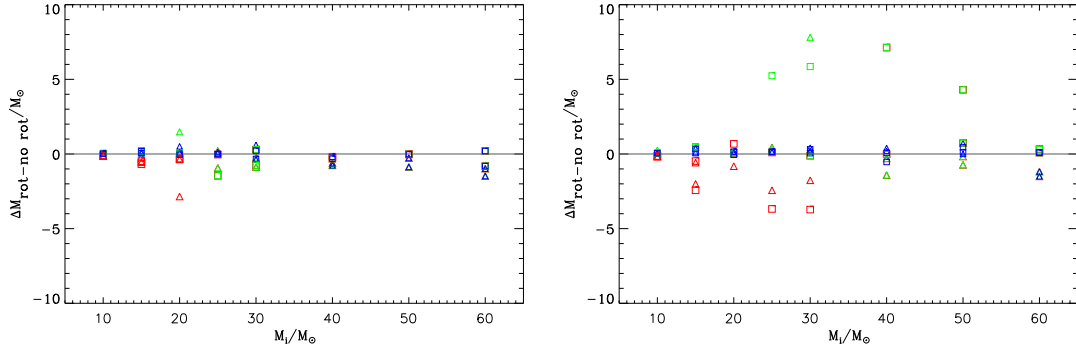
5.2.1 Rotation and Magnetic Fields

Rotation can lead to two opposite effects on the MS concerning the luminosity (Brott et al. 2011). Typically, it is assumed that rotation increases the luminosity by more efficient mixing, and thus increased core masses. For our models, this only occurs for some of the highest mass stars considered, in combination with strong rotation, and especially for grids where mixing is increased, either directly by an increase in overshooting or rotational mixing efficiency (grids 2 and 4), or indirectly by applying reduced mass loss rates (grids 3a-3c/d) and thus higher rotational velocities. At lower metallicity, the increase in luminosity is much more prominent, as the rotation rates are in general higher.

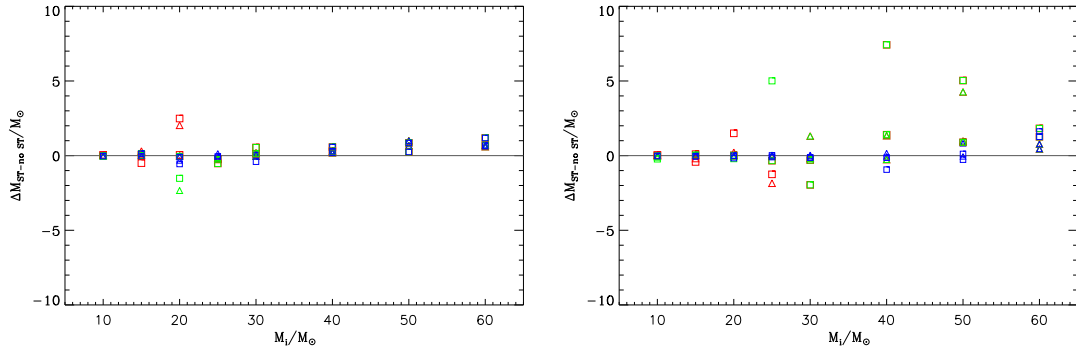
We can see an increase in surface abundances for all rotating models. In Fig. 5.6, we compare the surface nitrogen enrichment in our calculations to those of Brott et al. (2011). Non-rotating models do not mix any processed material to the surface on the MS, while rotating models can show drastic changes in the surface abundances. Our calculations are consistent with the results of Brott et al., both concerning the timescales, and the number fractions. Small differences can be



a) Difference between Ledoux and Schwarzschild criterion. Different symbols are used to compare between different rotation rates: non-rotating (plus-symbols), $\Omega = 0.2\Omega_{crit}$ (triangles), and $\Omega = 0.4\Omega_{crit}$ (squares)

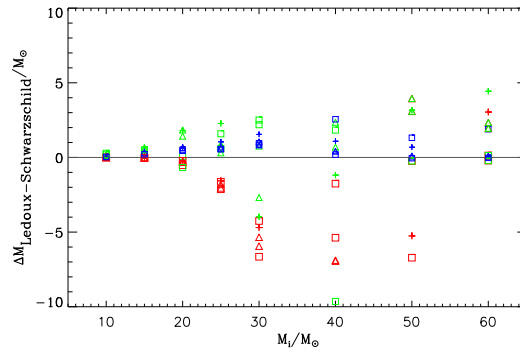


b) Difference between rotating ($\Omega = 0.4\Omega_{crit}$) and non-rotating models. Different symbols are used to compare between models including magnetic fields in the Spruit-Tayler description (triangles) and without (squares)

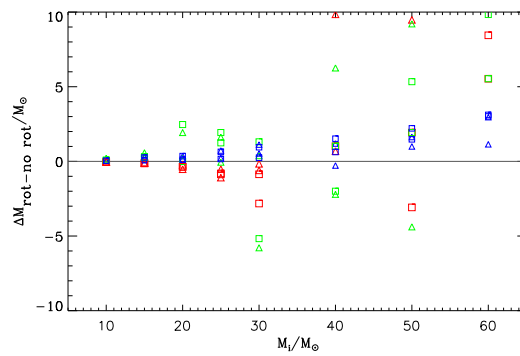


c) Difference between models including, and without magnetic fields. Different symbols are used to compare between different rotation rates: $\Omega = 0.2\Omega_{crit}$ (triangles) and $\Omega = 0.4\Omega_{crit}$ (squares).

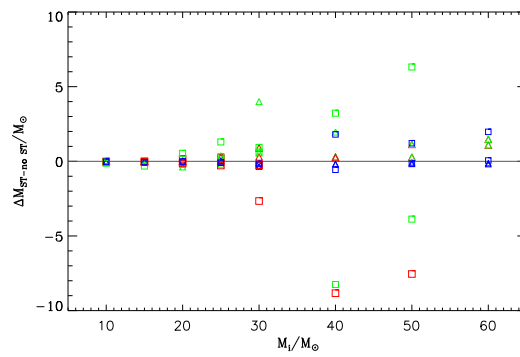
Figure 5.4: Differences in core masses (M_{He} , M_{CO}) and final mass, M_f , resulting from different descriptions of specific processes. Models of the standard grids with MW and LMC abundances are shown on the left and right, respectively.



a) Difference between Ledoux and Schwarzschild criterion. As Fig. 5.4a.



b) Difference between rotating and non-rotating models. As Fig. 5.4b.



c) Difference between models including magnetic fields and without. As Fig. 5.4c.

Figure 5.5: As Fig. 5.4, but for lowZ.

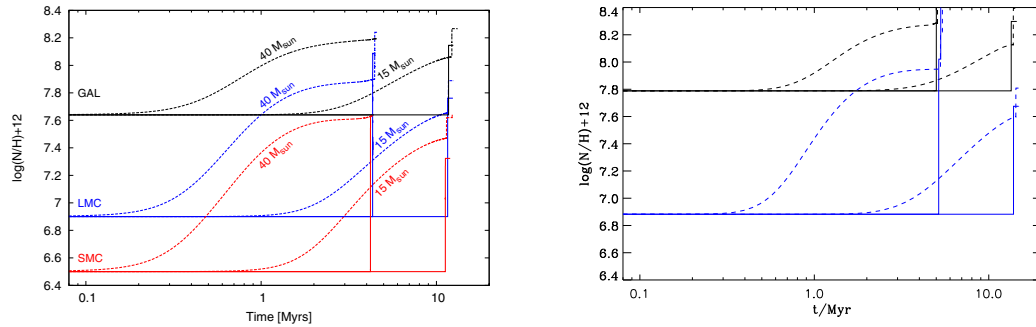


Figure 5.6: Comparison of the surface nitrogen enrichment of the models calculated by Brott et al. (2011), (left), and our models (right). Models at MW (black), and LMC metallicity (blue) are shown. Non-rotating models (solid) do not show any surface enrichment on the MS, while the surface nitrogen abundance increases for rotating models (dashed), where the initial rotational velocities are $v_{rot} \approx 270\text{km/s}$ for Brott et al., and $\Omega = 0.4\Omega_{crit}$ for our calculations. Our results and the calculations by Brott et al. agree in an order of magnitude comparison, both concerning number fractions and timescales.

explained by slightly different rotation rates and other minor differences in the models, similar to what has been discussed in Sec. 3.4.2. A more detailed analysis of the surface abundances on the MS is beyond the scope of this thesis.

In contrast to the changes in surface abundances, rotation decreases the luminosity for most of our models. This is the second of the two opposite effects mentioned above. This decrease is related to the reduced effective gravity (because of rotation), which leads to a reduced effective mass coordinate for the whole star. The reduction is by a constant factor for solid body rotation (with Spruit-Tayler dynamo), and even stronger for inner regions without the Spruit-Tayler dynamo, as rotation rates increase towards inner regions, as shown in Fig. 5.8. The effective mass enters partly in the derivation of the relation $L \sim M^\alpha$, such that a decrease also affects the luminosity. This effect is more pronounced for lower rotation rates, where mixing plays a lesser role.

In all cases, however, the MS becomes extended, as more material is available to be burnt.

All rotational effects become more important for lower metallicity, but overall affect the evolutionary tracks weakly. An exception are models that evolve quasi-chemically-homogeneously, which we will discuss later in more detail. However, this might change if advective angular momentum transport is included, as argued in Sec. 3.4.1. The main effect in our calculations are the changes in the surface abundances. The low importance of rotation, and also the dominance of the effect

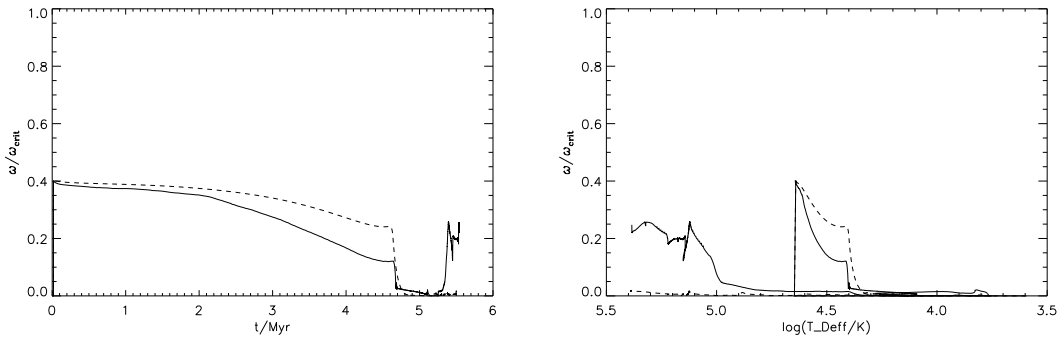


Figure 5.7: Comparison of the evolution of the angular velocity of a $40M_{\odot}$ model at MW metallicity with (dashed) and without (solid) magnetic fields in the Spruit-Tayler description. If magnetic fields are active, the star keeps a higher rotation rate. In general, the rotation slows down already on the MS.

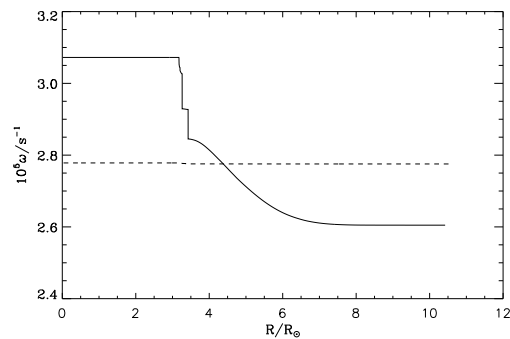


Figure 5.8: Comparison of the internal run of rotation with (dashed) and without (solid) magnetic fields for a $40M_{\odot}$ model with MW metallicity.

decreasing the luminosity, can be explained by the slowdown already on the MS, which is shown in Fig. 5.7. At MW and LMC metallicity, it occurs even faster for higher initial masses as the mass loss rates are higher. Only for lower metallicities or reduced mass loss rates, the star can keep the rotation rates sufficiently high.

The general effect of rotation on the progenitor properties is to increase the core masses while the final mass is decreased, as one can see from Figs. 5.4b and 5.5b. The increase in core masses can be explained by more efficient mixing through the radiative envelope by the different rotational instabilities. Higher core masses and higher rotation rates both favour higher mass loss rates, thus reducing the final mass. However, the effect is very small at MW and LMC metallicity, and can be seen clearly only at lowZ.

Internal magnetic fields can enforce solid body rotation, as shown in Fig. 5.8. As less angular momentum is redistributed to the core, this keeps the surface rotation rates on the MS higher, as can be seen for the dotted line in Fig. 5.7.

Thus, magnetic fields can increase the effects of rotation, and lead to increased core masses, and reduced final masses. As expected, the higher the rotation, the larger this effect.

5.2.2 Convective Boundary Criterion

From the HRDs in Figs. 5.1 to 5.3, we can see that the choice of the convective boundary criterion does not change the MS evolution, as already discussed in Sec. 3.3.1. However, it can affect the post main sequence evolution drastically.

Models that are calculated using the Schwarzschild criterion are brighter on the post main sequence as can be seen for the $15 \dots 30M_{\odot}$ models of the default grid at MW metallicity in Fig. 5.1. Models using the Ledoux criterion, on the other hand, are fainter, at least for MW and LMC metallicities. Even though, they more likely end their life in the blue, and also for lowZ experience higher mass loss. The initial mass limit for the formation of WR stars is shifted to lower masses, as can be seen for the $30M_{\odot}$ model at MW metallicity in Fig. 5.1.

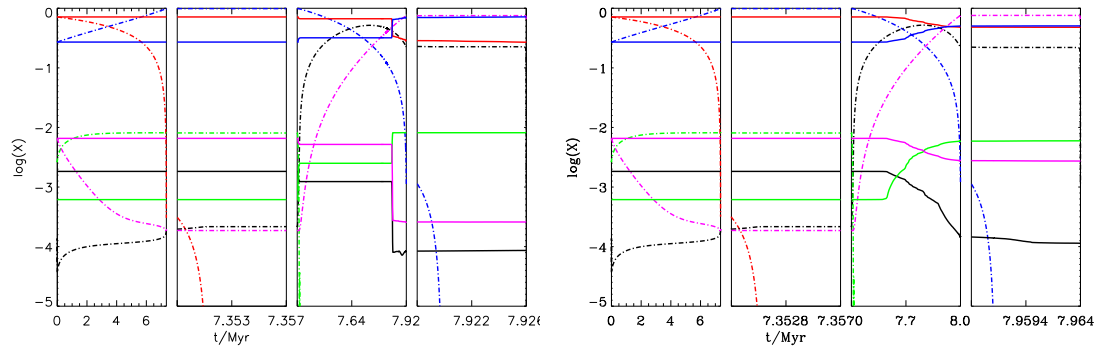
Indeed, for LMC as well as MW metallicity, the most important uncertainty comes from the treatment of the convective boundary criterion, as can be inferred from Fig. 5.4!

To understand the origin of this difference, we take a more detailed look on the structure of these two models, shown in Fig. 5.9. Already during shell hydrogen burning, the shell-convection drastically changes the structure in the outer envelope. The two models separate after the hook, when core helium burning sets in. For the model calculated using the Ledoux criterion, the envelope convection² during central helium burning reaches deep stellar layers, resulting in a dredge up, consistent with the results of Kaiser et al. (2020), and brings up processed material to the surface. In contrast, envelope convection is restricted to a surface layer for the Schwarzschild case.

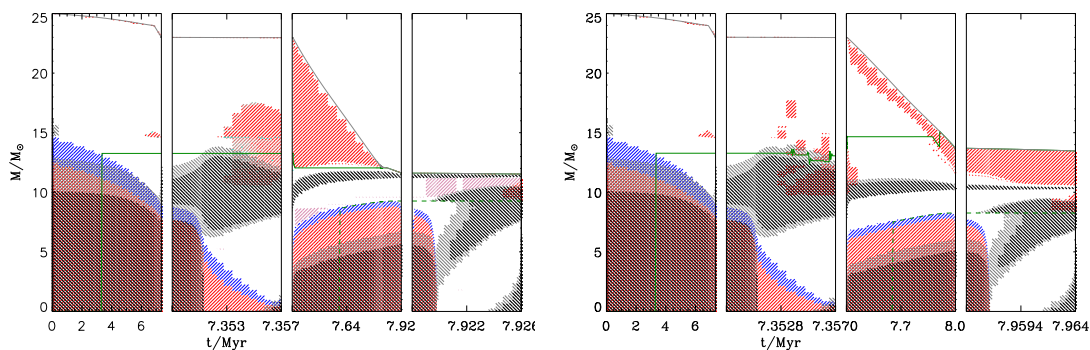
Nevertheless, the helium core mass is higher when central helium burning sets in for the model calculated using the Schwarzschild criterion, thus resulting in a higher luminosity.

In general, a higher luminosity should lead to a higher mass loss, and thus lower final masses. However, in this case the mass loss in late RSG phases is of great importance. This can be seen best for the models at lowZ. In contrast to higher metallicities, where a noticeable increase of mass loss occurs when crossing the

²The existence of envelope convection during these later phases was discussed in Sec. 3.2.2. The main reason are changes of the opacity in the envelope.



a) Evolution of surface (solid) and central (dashed) abundances. The elements plotted are **hydrogen**, **helium**, carbon, **nitrogen**, and **oxygen**. We can clearly see the dredge-up in the Ledoux case when core helium burning stars ($t \approx 7.357$ Myr) as a jump in the surface abundances, especially for carbon, nitrogen, and oxygen.



b) Kippenhahn diagrams comparing these models. Regions are indicated using different colors, as in 3.2. The outer convective zone during shell hydrogen burning is different for the two criteria, and the core mass increases in the Ledoux case, when central helium burning sets in.

Figure 5.9: Comparison of the evolution of a $25M_{\odot}$ model at solar metallicity, calculated with the Ledoux (left) and the Schwarzschild criterion (right).

bi-stability jump, at low metallicity, the rates provided by Vink, de Koter, and Lamers are very small. The only rate that is independent of metallicity is the one provided by de Jager, and thus determines almost all mass loss³. Depending if we use the Ledoux or the Schwarzschild criterion, the post MS evolution occurs on different timescales, as can be seen for a $40M_{\odot}$ in Fig. 5.10. The de Jager rates set in at a different point in time, as can be seen from the HRD, and shown directly in Fig. 5.11. The mass loss lasts for $\mathcal{O}(10^4)$ years when we use the Ledoux criterion, whereas it lasts for $\mathcal{O}(10^5)$ years when the Schwarzschild criterion is applied. The difference in the timescale of de Jager, Nieuwenhuijzen, and van der Hucht (1988) mass loss can fully account for the difference in final mass of $\Delta M_f \approx 10$.

³However, as argued in Sec. 2.6, it might be overestimated.

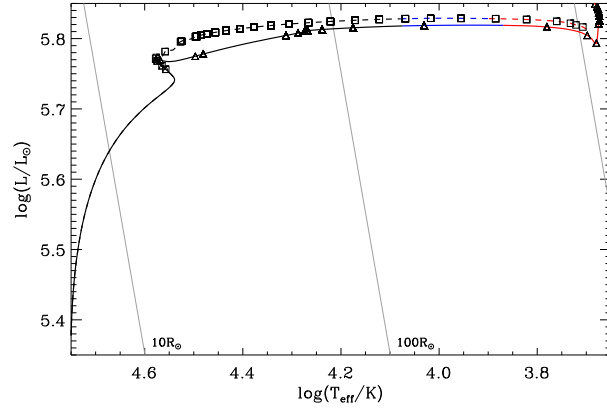


Figure 5.10: Comparison-HRD of a $40M_{\odot}$ non-rotating model at lowZ calculated using the Ledoux criterion (solid) and the Schwarzschild criterion (dashed). The Line is colored depending on the mass loss scheme: Vink, de Koter, and Lamers to de Jager, Nieuwenhuijzen, and van der Hucht and the transition region. After the main sequence we display symbols every 1000 yr.

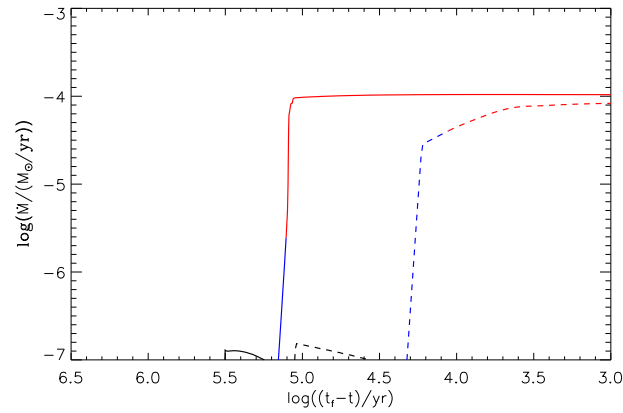


Figure 5.11: Comparison of the mass loss rates of the same $40M_{\odot}$ at lowZ as in Fig. 5.10. The model calculated using the Ledoux criterion (solid) spends much more time in the RSG regime where the de Jager rates apply than the model calculated using the Schwarzschild criterion (dashed).

We can do a more quantitative analysis of this difference using Figs. 5.4a and 5.5a, with the following result. Applying the Ledoux criterion reduces the final mass drastically, while it increases the core masses. For models that end as WR stars, also the helium core mass can be reduced, together with the total mass.

As rotational mixing is very efficient for stars at low metallicity, the difference between the Ledoux and the Schwarzschild criterion becomes smaller for rotating stars. Other effects become more important, such as mechanical mass loss in this

case. As the ST dynamo keeps the rotation rates higher, this further decreases the difference.

5.3 Specific Effects

Within the different grids, we study the influence of uncertainties in the overshooting parameter, mass loss rates, and the rotational mixing efficiency. A comparison of the evolutionary tracks of all grids is shown in Figs. 5.12 to 5.14. As the HRDs would become convoluted if also an increased mixing efficiency was accounted for, we show the latter effect separately in Fig. 5.17. For all grids, we do a more quantitative analysis similar to the systematic effects, shown in Figs. 5.15, 5.16, and 5.18. We start with a brief comparison of the different metallicities, before we continue with the effects mentioned above.

5.3.1 Metallicity

The most important effect of metallicity is the reduction of mass loss rates. This leads to a shift of the initial masses required to form WR stars, towards higher values. In the extreme case of lowZ, most of the models considered end their life as RSGs. Only the higher mass stars with $M_i \gtrsim 50M_{\odot}$ can evolve back to the blue and become BSGs, but no WR stars are formed. As explained already, the mass loss rates provided by de Jager, Nieuwenhuijzen, and van der Hucht (1988) become more important, as they are the only ones not depending on metallicity. The effect of a metallicity scaling will be discussed later in this section, together with the other grids set up for “manipulating” the wind.

In addition, models at lower metallicity are more compact. This, in conjunction with their lower mass loss rates (less loss of angular momentum), enables keeping higher rotation rates, such that rotation becomes a more important parameter. Another critical difference for lowZ is the lack of catalysts. These are necessary for burning via the CNO cycle, such that models at this metallicity have a pp-chain being active in their center (during the MS) instead.

5.3.2 Overshooting

From the HRDs in Figs. 5.12b to 5.14b, we can see that a higher overshooting value causes the MS to be brighter and more extended. It further increases the

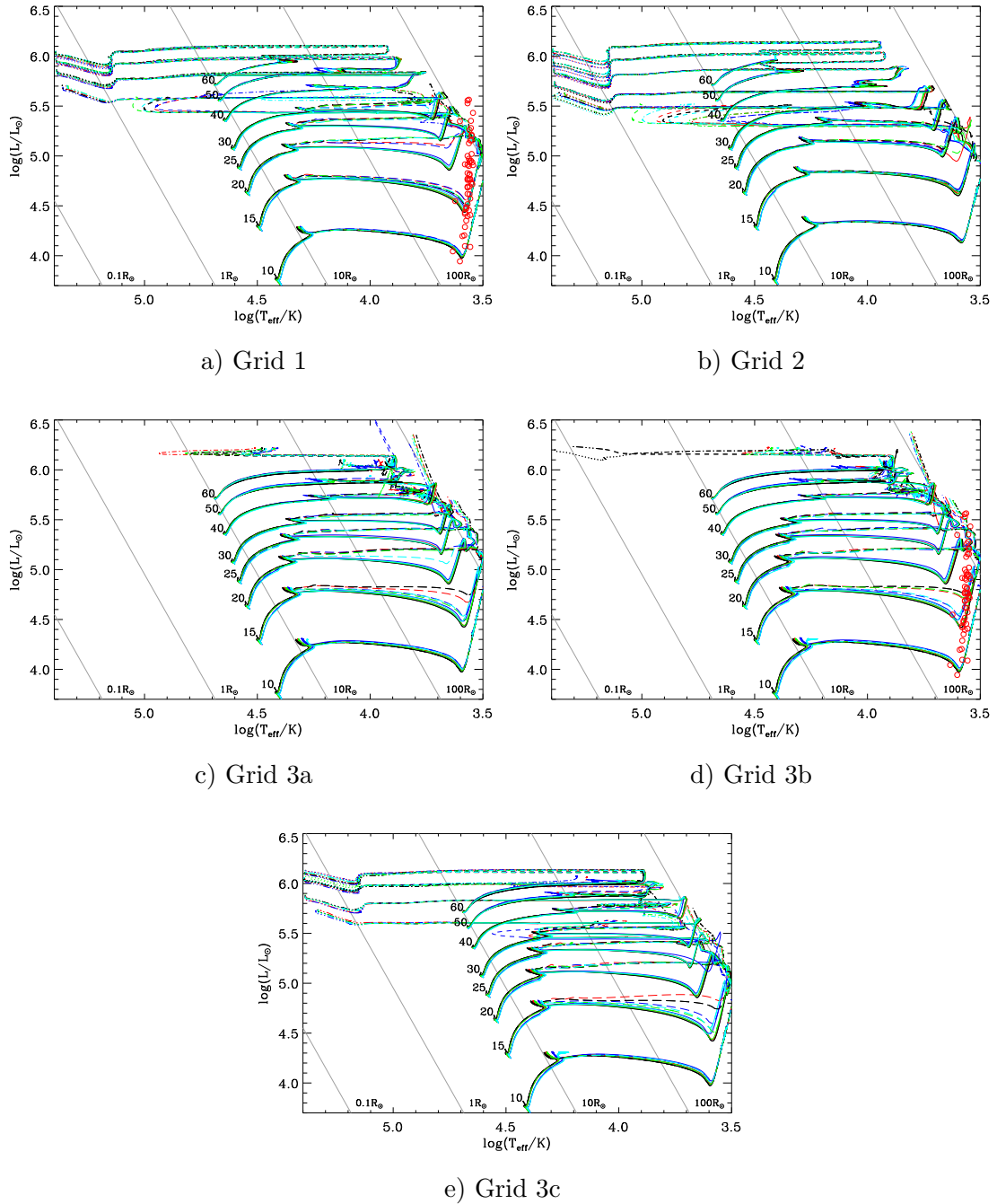


Figure 5.12: Hertzsprung-Russell diagrams of all models with MW metallicity. Colors and linestyles indicate different parameters, as in Fig. 5.1. See text for further discussion.

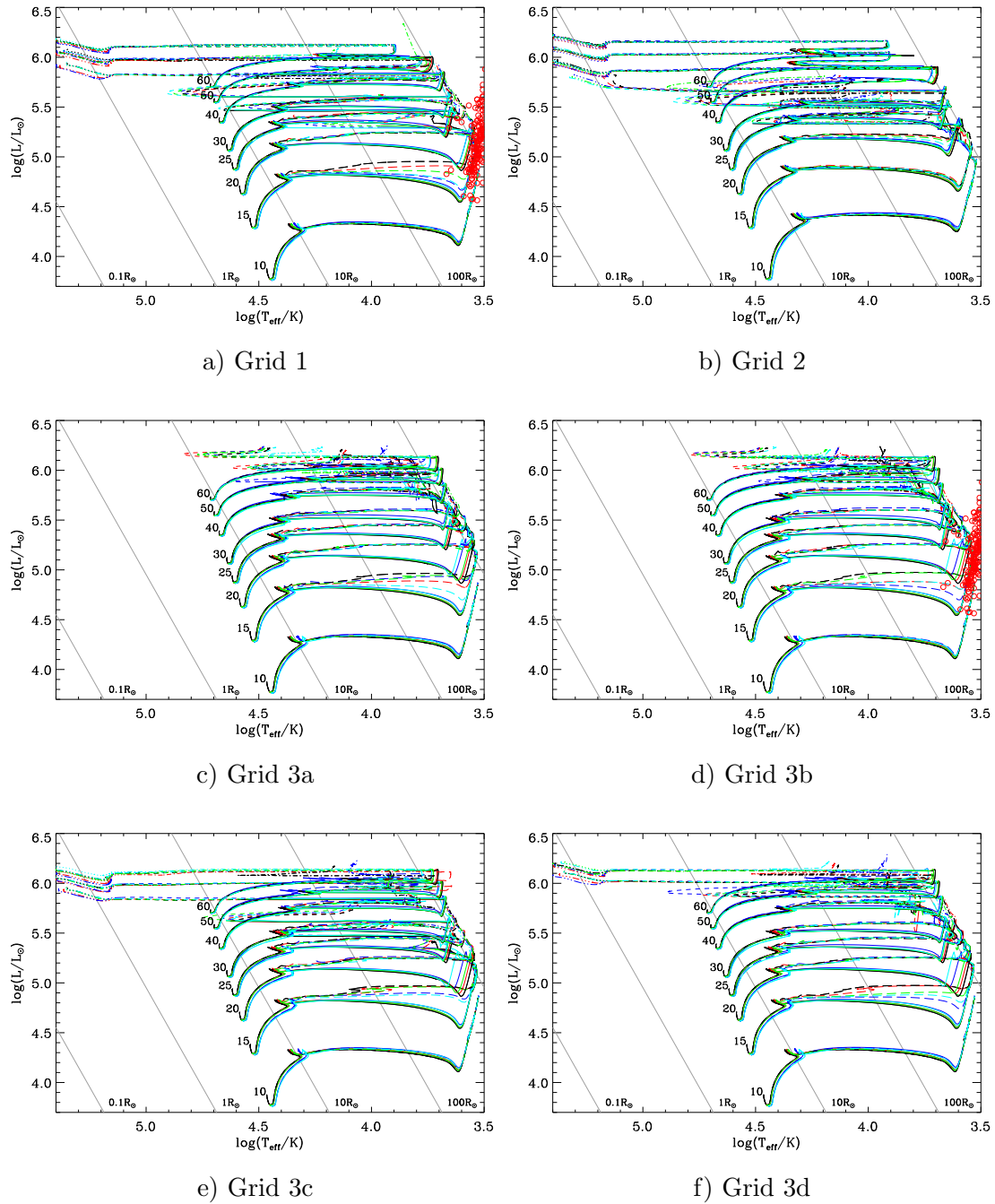


Figure 5.13: As Fig. 5.12, but for LMC metallicity. RSGs from the LMC (Massey and Olsen 2003) are indicated as red circles.

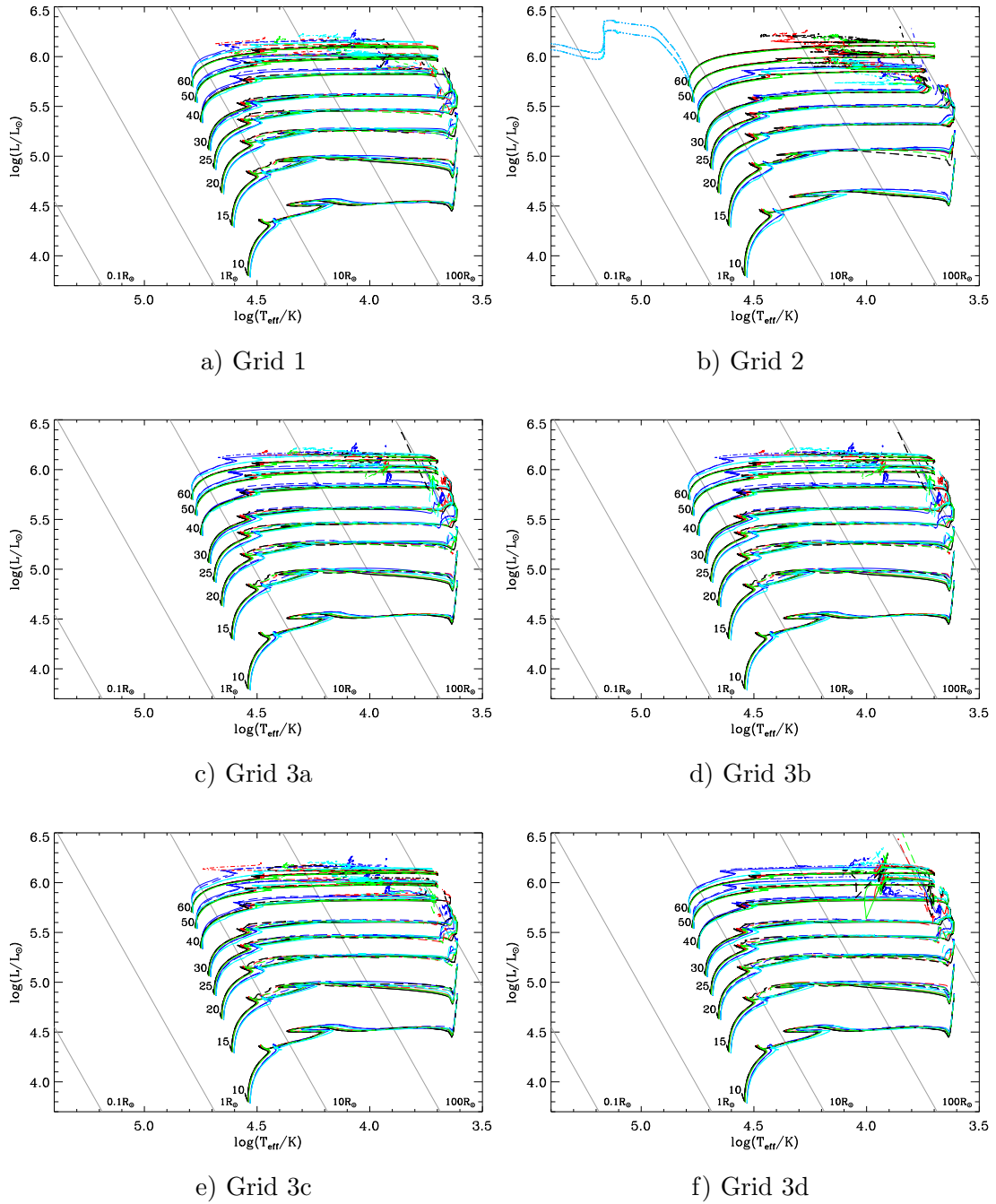


Figure 5.14: As Fig. 5.12, but for lowZ.

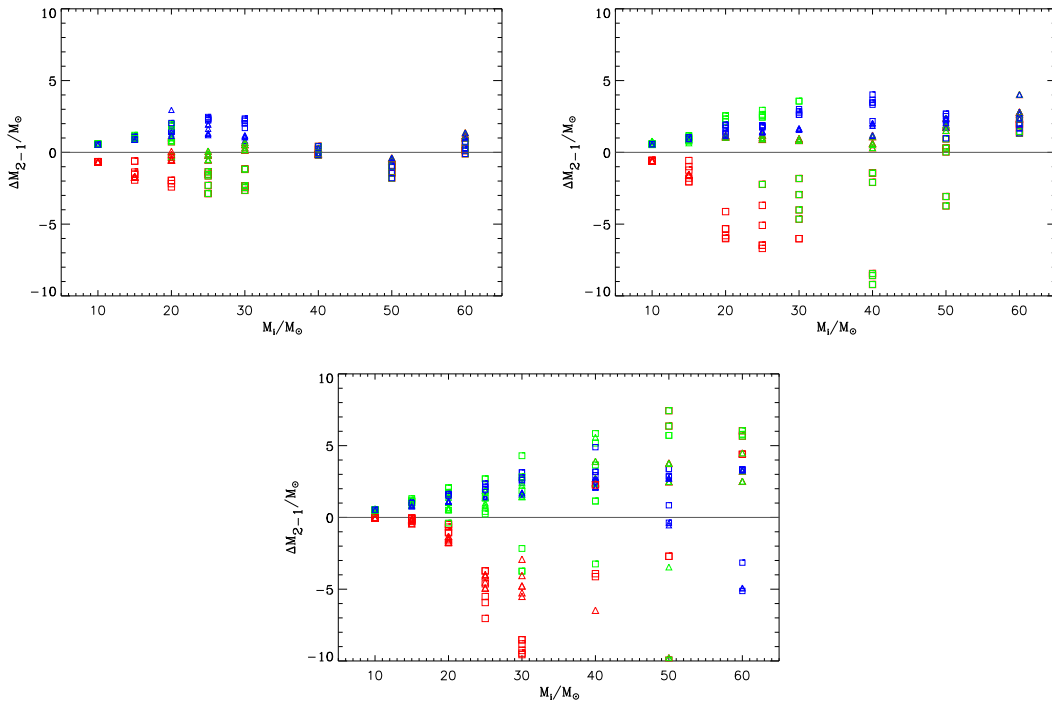


Figure 5.15: Differences in core masses (M_{He} , M_{CO}) and final masses, M_f , for the grid with increased overshooting (grid 2) and the standard grid (grid 1) at MW metallicity (upper left), LMC metallicity (upper right), and lowZ (lower). We distinguish between models calculated using the Ledoux (triangles), and the Schwarzschild criterion (squares). Larger overshooting increases the core masses, while it decreases the final mass.

MS lifetime. During the later evolution, a higher value can also lead to an evolution towards the blue, either to the BSG regime of even towards WR stars.

This can be explained by analysing the core and final masses, shown in Fig. 5.15. As a direct effect, larger overshooting increases the core mass by $\approx 1 \dots 3M_{\odot}$ at MW metallicity, and up to $\Delta M_{CO} \approx 5M_{\odot}$ and $\Delta M_{He} \approx 8M_{\odot}$ at lowZ. This has two indirect effects. At first, it increases the mass loss rates, and thus reduces the final mass. And second, it reduces the envelope mass, as the core mass is increased. In combination with increased mass, the reduced envelope mass makes it much easier to remove the envelope, and explains the drastic shift of the WR limit towards lower masses. While in our standard grid at MW metallicity, WR stars form for $M_i \gtrsim 30M_{\odot}$, for increased overshooting, they form already for $M_i \gtrsim 25M_{\odot}$ (compare Figs. 5.12a and 5.12b). For WR stars, the final mass depends only very weakly on the parameters chosen and on the earlier evolutionary history. This can be explained by the special behaviour of their mass loss rates,

at least for Galactic metallicities. While Eqn. (2.93) predicts a dependence on their luminosity, Schaerer and Maeder (1992) find that the luminosity is directly connected to their mass via

$$\log \frac{L}{L_{\odot}} = 3.4949 + 1.7267 \log \frac{M}{M_{\odot}} \quad (5.1)$$

from fits to their models. In combination, the mass loss rate depends on the mass. Thus, WR stars with initially higher mass lose more mass, such that the final masses become independent of the earlier evolutionary history. We can see this behaviour of the final mass for higher metallicities and higher initial masses. This is similar to the result for helium stars calculated by Woosley, Heger, and Weaver (2002).

WRs also lost at least their hydrogen rich envelope, such that the helium core mass and the final mass coincide. For most WR stars, they even become WC stars, such that the same is true for the carbon core mass. In combination, this causes the differences in core and final masses to become negligible, if the models end as WR stars in both grids.

For lowZ, two models even show QCHE due to the efficient mixing. These stars skip the RSG regime, and their final structure is very different from the other models.

5.3.3 Mass loss

As already explained, we changed the mass loss prescription towards more realistic values in several steps. In the following, we begin our discussion with a description of the effects at MW and LMC metallicity, as at lowZ the whole mass loss originates from the RSG phase alone, where the de Jager rates apply.

For grids 3a and 3b, where the total mass loss is reduced, the effects on the evolutionary tracks are extreme. The limit, where WR stars form, is shifted towards much higher initial masses, and almost all models end their life as RSGs. Only very few $60M_{\odot}$ models evolve back towards the blue. The final masses are larger, as can be seen in Fig. 5.16. As less mass is lost, the core masses can become larger as well.

The effect of the reduced jump temperature is much smaller. In general, this decreases the mass loss rates even further, and thus amplifies the effect. An exception are some $60M_{\odot}$ models at MW metallicity, which evolve towards the WR phase only in this case, while they ended as BSGs with unchanged jump

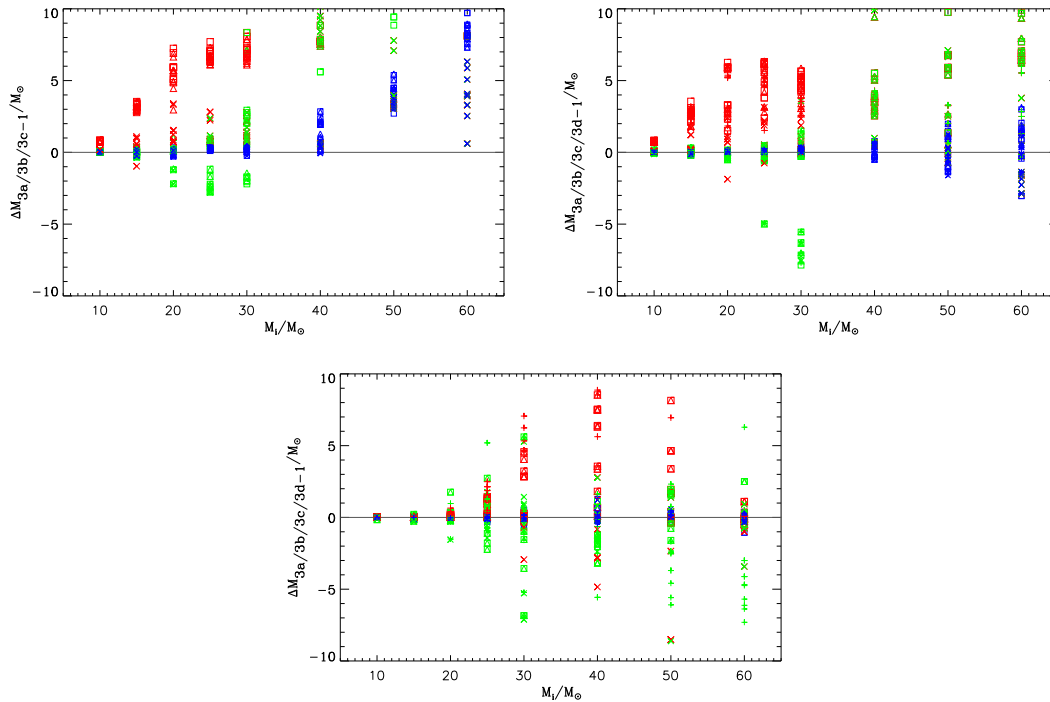


Figure 5.16: As Fig. 5.15, but for the mass differences between grids with reduced mass loss rates (grid 3a(triangles)/b(squares)/c(x-symbols)/d(plus-symbols, only for LMC metallicity and lowZ)) and the standard grid. At MW and LMC metallicity, reduced mass loss leads to higher remnant masses. At lowZ, the situation is more complicated.

temperature (compare Figs. 5.12c and 5.12d). This might be explained by the second time they cross the bi-stability jump on the way back. However, the difference is very small for these models.

When only the Vink mass loss is scaled down, the changes compared to the standard grid are much smaller. Nevertheless, these models show the same systematic increase in core and final masses.

As, together with the mass, also angular momentum is lost, reduced mass loss rates can prevent the slowdown of rotation on the MS, not only at lowZ, but also at LMC metallicity. These models show more pronounced effects of rotation, and can even reach critical rotation and implicit mass loss.

At lowZ, the evolutionary tracks do not change significantly in all cases, as the overall mass loss is very low. However, as argued already, the de Jager mass loss rates play a major role. Especially for higher mass stars, the mass being lost in the RSG regime allows them to move back towards the blue. If this is prevented by including a metallicity scaling, they can evolve close to the Eddington limit,

probably related to an LBV phase. The behaviour and especially the mass loss during these phases are highly unknown. For our models, they end their life as RSGs, with a total mass loss for the highest mass models of only $\Delta M \lesssim 1 \dots 3M_{\odot}$. However, there exist no constraints from observations or theory, whether such a metallicity scaling should be included. This introduces the largest uncertainty at lowZ, and can be seen best for the higher mass models.

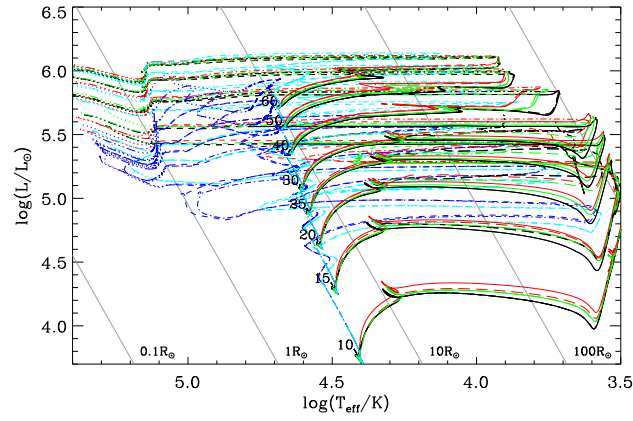
The complex behaviour of the helium core masses at lowZ, displayed in Fig. 5.16, and in general the decrease of specific helium core masses, also at other metallicities, can be explained by slight differences in the envelope convection during later phases. This is similar to the differences between the Ledoux and Schwarzschild criterion, discussed in Sec. 5.2.2.

5.3.4 Mixing

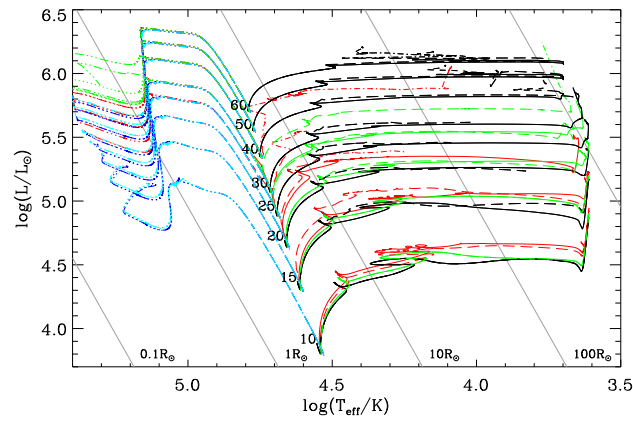
As expected, an increased mixing efficiency makes QCHE much more likely. As these tracks are very different compared to “classical” ones, and give rise to complicate tracks in the HRD, we show the latter enlarged in Fig. 5.17. Note that the tracks of non-rotating models are unchanged from the default grid.

In contrast to the default grid, all rotating models show an increased luminosity due to the efficient mixing. For most of the rapidly rotating models with $\Omega = 0.4\Omega_{crit}$, this even leads to quasi chemically homogeneous evolution. These models evolve towards higher luminosities, at roughly constant radii. As the surface abundances increase in parallel with the central ones, they eventually become WR stars, without evolving through the RSG regime. Thus, even $10M_{\odot}$ stars can form WRs, independent of the metallicity! As this is in contradiction to observations, the real uncertainty, at least for lower masses, is most likely lower than our extreme assumption.

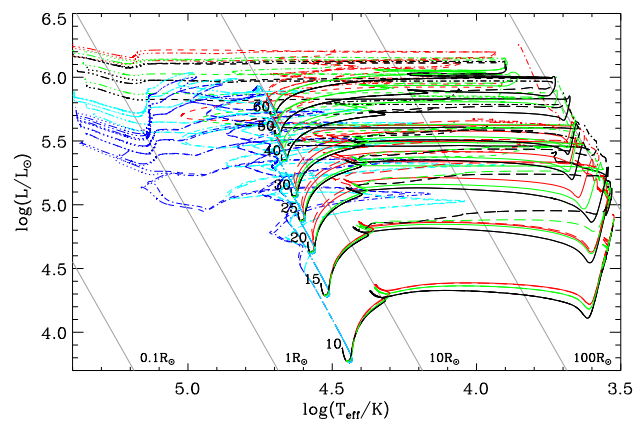
Our evolutionary tracks are roughly consistent with the tracks presented by Köhler et al. (2015). The latter have been calculated for rapidly rotating very massive ($M_i \geq 60M_{\odot}$) models at LMC metallicity and “normal” mixing efficiencies. Thus, we can only compare the main features. Both show the same luminosity and temperature evolution during most of their evolution. One difference is that our models do not expand and evolve towards the red at any point, while the models by Köhler et al. evolve to lower temperatures just before they become WR stars. In our earlier models, however, we could see a similar decrease in effective temperatures for a small fraction of their lifetime, depending



a) MW metallicity



b) LMC metallicity



c) lowZ

Figure 5.17: Hertzsprung-Russell diagrams for all models with increased rotational mixing efficiency, at different metallicities. Colors and linestyles indicate different parameters, as in Fig. 5.1. See text for further discussion.

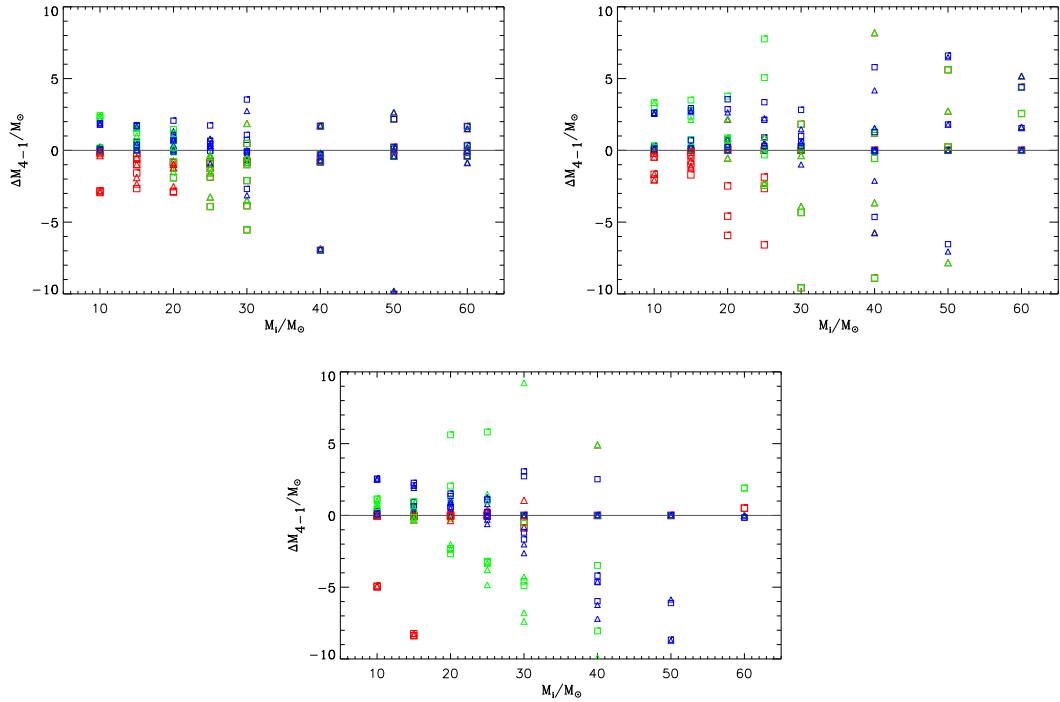


Figure 5.18: As Fig. 5.15, but for differences between increased rotational mixing efficiency (grid 4), and the standard grid. Models evolving quasi chemically homogeneously show a very different behaviour.

on the exact settings that decide how to deal with critical rotation (especially the wind setting).

Returning to our grids, a detailed comparison of the core and final masses, as resulting from enhanced vs. standard mixing, is provided in Fig. 5.18. As a direct effect, the efficient mixing increases the core masses. However, the lower initial mass limit for WR stars can cause a reduction of core and final masses. As rotation plays a major role at lower metallicity, this can be seen best for lowZ.

As for WR stars that formed the classical way, the final mass of WR stars that formed via QCHE is independent of the previous evolution. However, the final value is different compared to classical WRs. These models have drastically decreased core and final masses, also for higher masses at MW and LMC metallicity, where also in the standard grid WR stars form.

Thus, insecure mixing coefficients add a strong uncertainty, especially for lower mass models, that would end their life as RSGs otherwise, and for lowZ, where rotation rates remain higher.

6 Remnant Analysis

6.1 Remnant Masses

In the following, we will analyse the remnant masses resulting from our calculations. We use the two formalisms described in Secs. 3.5.3 and 3.5.4 to link the progenitor properties to the remnant mass. Besides discussing the individual effects, we compare our results with other calculations.

There are various studies with the intention of finding a relation between remnant and initial stellar mass. We will focus on the calculations performed by Heger and Woosley (2002) and Woosley, Heger, and Weaver (2002) who provide relations for zero metallicity¹ and for MW metallicity, respectively. In addition, theoretical considerations by Renzini and Ciotti (1993) are shown, which should also hold for MW metallicity. Even though Renzini and Ciotti use a very simple approximation, this function is used in several studies analysing microlensing observations, including Riffeser, Seitz, and Bender (2008), and Thomas et al. (2011).

6.1.1 Remnant Masses at MW Metallicity

The resulting remnant masses at MW metallicity are shown in Fig. 6.1. It is important to notice that the different formalisms provided by Woosley, Heger, and Weaver (2002) and Belczynski et al. (2008) show a reasonable agreement in most cases. Nevertheless, there is a noticeable difference for some masses in the transition from NSs to direct BHs, i.e. for models with $M_i \approx 20 \dots 30 M_\odot$ at MW abundance. There is an even bigger disagreement of remnant masses for the WR stars that form for lower masses $\lesssim 20 M_\odot$, which are a result of QCHE (red and

¹As discussed in Sec. 3.5.3, zero metallicity means here a very low metallicity, where almost no mass loss is present.

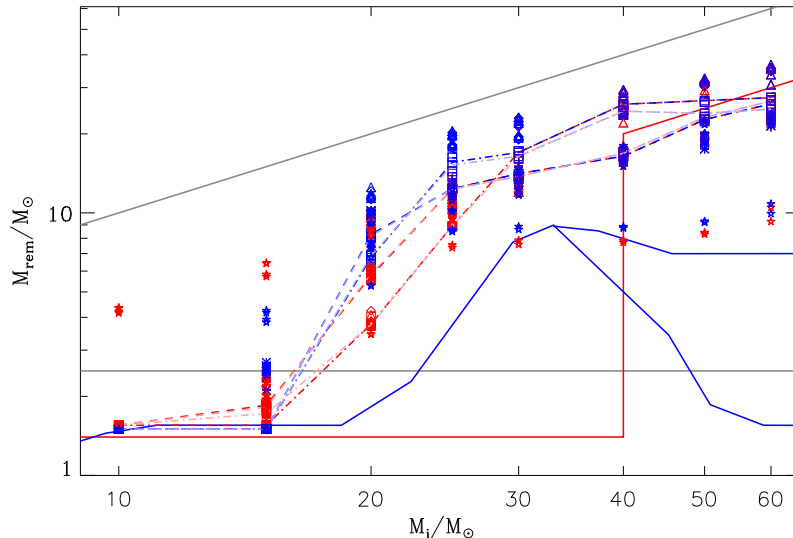


Figure 6.1: Comparison of remnant masses from our calculations at MW metallicity with other studies. Solid lines indicate calculations by Woosley, Heger, and Weaver (2002) (MW metallicity) (two blue lines, differentiating the adopted WR mass loss), and Renzini and Ciotti (1993) (red). Different symbols differentiate between different grids: grid 1 (plus-symbols), 2 (asterisks), 3a (diamonds), 3b (triangles), 3c (squares), and 4 (stars). We show both, the remnant masses calculated using the Woosley formalism (red symbols), and the Belczynski formalism (blue symbols). Indicated by lines are also our current preferential models with reduced Vink mass loss (grid 3c), mild rotation ($\Omega = 0.2\Omega_{crit}$), both with Ledoux (dashed) and Schwarzschild criterion (dashed dotted) applied, and for ST turned on (dark color) and off (bright color). The grey line at the top displays the one-to-one relation, and the lower one at $M_{rem} = 2.5M_{\odot}$ marks the limit between the formation of NSs and BHs. See text for further details.

blue stars at $10M_{\odot}$ and $15M_{\odot}$). As their final structure is very different from other models, it is unclear which formalism would be the better choice.

The different grids as well as different physics introduce an uncertainty in remnant masses. Especially, the grid with increased mixing coefficients shows a different trend compared to all other grids. The remnant masses of WRs that formed via QCHE is $M_{rem} \approx 10M_{\odot}$, independent of the evolutionary history. This is a consequence of the behaviour of core and final masses described in the previous sections (see Sec. 5.3.4).

The other grids show the behaviour expected from the considerations in the previous chapter. Reduced mass loss rates increase the remnant masses. The same is true for increased overshooting at lower initial masses. For higher initial masses, increased overshooting leads to the formation of WR stars, that are slightly lower

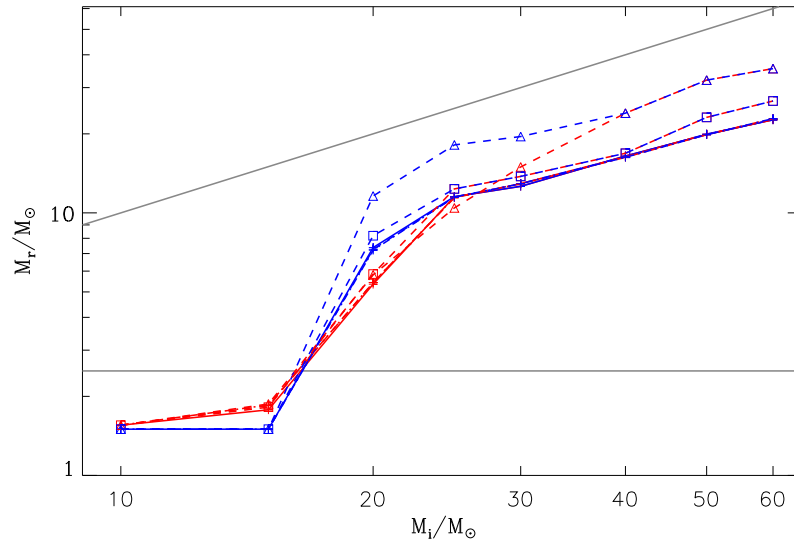


Figure 6.2: Comparison of uncertainties in remnant masses at MW metallicity due to rotation and mass loss. Symbols and colors as in Fig. 6.1. Only a selection of models is displayed for clarity. For the standard grid, non rotating (solid line), mildly rotating ($\Omega = 0.2\Omega_{crit}$, dashed line), and rapidly rotating ($\Omega = 0.4\Omega_{crit}$, dashed dotted) models are shown. Only mildly rotating models are included within the grids with reduced mass loss rates. The displayed models are calculated using the Ledoux criterion, and with the Spruit-Taylor dynamo applied.

in mass, but lead to similar remnant masses as the other models that form WR star via “classical” tracks, at around $M_{rem} \approx 20 \dots 30M_{\odot}$ (compare Sec. 5.3.2).

As already argued, within a single grid the choice of the convective boundary criterion adds a significant uncertainty, as can be seen from the dashed and dotted lines, shown in Fig. 6.1. The ST dynamo only plays a weak role. Also rotation only leads to a very small difference in the remnant mass, as shown in Fig. 6.2. Reducing the Vink mass loss rates, differences are larger, and even more extreme when the total mass loss rates are scaled down. Presumably, the reality is somewhere in between, since also the WR mass loss rates might be overestimated, as argued in Sec. 2.6.

6.1.2 Comparison with Other Studies

Using Fig. 6.1, we can compare our results at MW metallicity with those from other calculations. In almost all cases, we find higher remnant masses than Renzini and Ciotti (1993). The only exception are the most massive WR stars, that agree

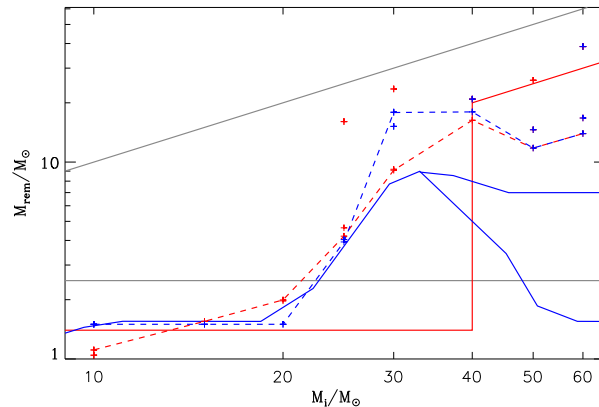


Figure 6.3: Comparison of remnant masses with other studies for non-rotating models with no overshooting at MW metallicity. The WR mass loss is increased by a factor of 10. Solid lines indicate calculations by Woosley, Heger, and Weaver (2002) (MW metallicity) (blue), and Renzini and Ciotti (1993) (red). Models calculated using the Ledoux criterion are connected with a dashed line. The displayed models are able to reproduce the results of Woosley, Heger, and Weaver (2002) at a large extent.

quite well with the approximated BH masses predicted by Renzini and Ciotti, and indeed, much better than with the other studies!

Compared to Woosley, Heger, and Weaver (2002), we find a shift of the lower mass limit to form BHs towards lower initial masses. While we find a lower limit of $M_i \approx 15$, Woosley, Heger, and Weaver find that only stars with $M_i \gtrsim 21M_\odot$ form BHs. In addition, our WR masses are much higher.

There are two main reasons for these differences. The first is that Woosley, Heger, and Weaver did not apply overshooting in their models. Even though they argue it would be necessary to reproduce observations², our comparison (in particular Fig. 6.3 and corresponding text) suggests that they did not apply it in their calculations. The second reason is that in their calculations, the applied WR mass loss rates are not corrected for clumping, and thus too high, thus explaining our larger WR masses.

In Fig. 6.3, we can see that increasing the WR mass loss and neglecting overshooting, our calculations can get very close to the results provided by Woosley, Heger, and Weaver. However, it seems that even in their low mass loss scenario for WR stars, the mass loss is still higher than a factor of 10 compared to the rates we use.

²Though carefully reading their publication, we could not find any definite statement regarding whether they considered overshooting in their calculations or not.

In summary, we conclude that using modern calculations and state-of-the-art physical assumptions, our predictions for remnant masses are considerably larger than those predicted by Woosley, Heger, and Weaver (2002), for a wide range of initial masses.

6.1.3 Remnant Masses at Lower Metallicities

In Fig. 6.4, we compare the remnant masses at all metallicities considered for our calculations. At lower metallicity, the average remnant mass becomes increased. While the effect is small comparing LMC and MW metallicity, it is more pronounced at lowZ.

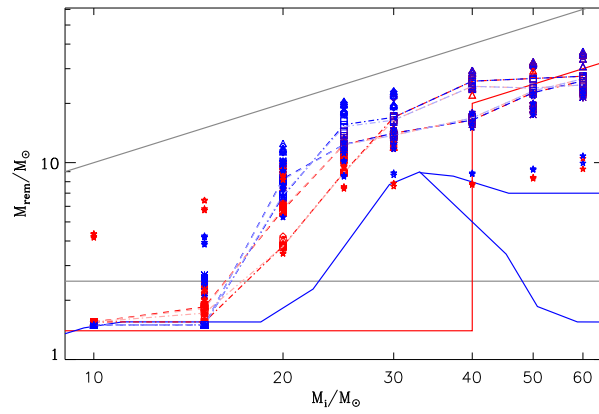
The general systematic effects within the grids are very similar at LMC metallicity when compared to MW metallicity models. From the lines indicated for the current preferential model at lowZ, we can notice that the choice of the convective boundary criterion plays a similar role as for other metallicities. However, the Spruit-Tayler dynamo and thus also rotation may play a larger role at lowZ³. Nevertheless, for most models the effect is still quite small.

A comparison of our remnant masses for lowZ with the calculations by Heger and Woosley (2002) for zero metallicity shows that our calculations coincide very well if calculated using the Woosley formalism, which is also based on the data provided by Heger and Woosley. Even though overshooting increases the core mass for our models, the mass loss (tiny at earlier phases, but significant for RSGs) that is only applied in our case has the opposite effect, explaining the agreement.

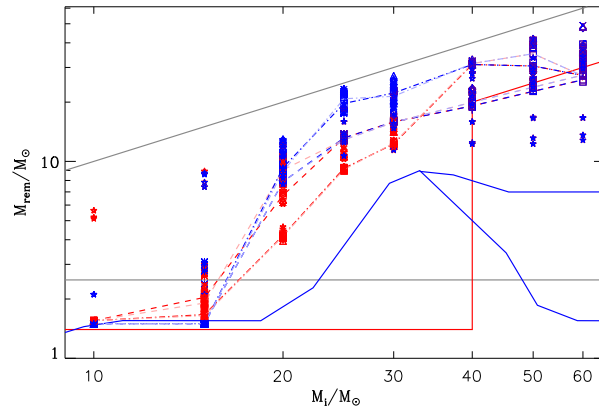
Moreover, there is a significant disagreement between the two formalisms at lowZ! One difference occurs for the models with increased rotational mixing, that end their life as WR stars. Woosley, Heger, and Weaver do not provide any WR regime at very low metallicity, such that we had to use the same description as for RSGs, not taking into account the different final structure. Also for the other models (those with $M_i = 15 \dots 30M_\odot$), there are essential differences in the predicted remnant masses, by a factor up to $\gtrsim 2$.

As explained, our models have several differences to the models calculated by Heger and Woosley, the most important ones being overshooting and mass loss. Thus, our final structure is very different, and the agreement with their data might just be a coincidence. As the mass loss at lowZ occurs during later stages, where

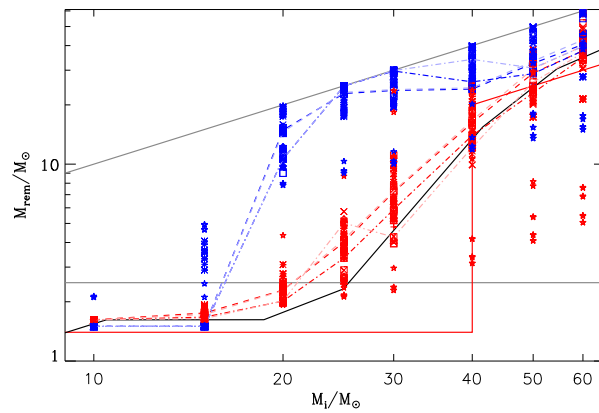
³Even though this is suggested by Fig. 6.4, we cannot provide a definite conclusion, since some $30M_\odot$ and $40M_\odot$ models of grid 3c where we observe a discrepancy have been calculated with slightly different settings (compare Sec. 4.2).



a) MW metallicity.



b) LMC metallicity.



c) lowZ.

Figure 6.4: As Fig. 6.1, but for different metallicities. At lowZ, the calculations by Heger and Woosley (2002) for $Z = 0$ (black solid line) are shown. For LMC metallicity and lowZ, grid 3d (x-symbols) is indicated. See text for further details.

also the CO core forms, the Belczynski formalism might be the more reasonable choice. Nevertheless, a more detailed analysis of the late evolution up to the iron core formation of stars at very low metallicity would be necessary to obtain confidence in this hypothesis.

Concluding, the biggest uncertainty for lowZ results from the differences between the Woosley and the Belczynski formalism! Only for smaller as well as much higher masses, both formalisms predict NSs and direct BHs, respectively, and thus agree again.

6.2 Remnant Types

In addition to analysing the remnant masses, we can explore the regions of metallicities and initial masses, where we expect different remnant types to form. In Fig. 6.5, the most popular result of Heger et al. (2003) is shown. The corresponding smaller range of metallicities and initial masses covered by our grid is indicated in this figure.

In the following, we only use the formalism based on Belczynski et al. (2008) for calculating the remnant masses, unless explicitly stated otherwise. As discussed in the previous chapter, for MW and LMC metallicity the choice of the linking affects the remnant masses and thus also the types only weakly. For lowZ, further analysis would be necessary to provide a valid linking formalism. Based on the remnant mass, the remnant type can be found, after comparing with the limits described in Sec. 3.5.2.

Since we considered in our calculations the effects of various uncertainties, in the resulting final diagrams displaying the remnant type as a function of initial mass and metallicity we find overlap regions, where different kinds of remnants might form. Such a diagram is provided in Fig. 6.6. The transition between the metallicities indicated is a piecewise zeroth order interpolation. The same is true for other masses than the ones for which we calculated models. We extend the grid point to a box with boundaries in the middle between neighbouring models (logarithmic space).

For all calculations, we observe a shift of the limits between different remnant types towards lower masses. This can be explained by overshooting, that was only included in our calculations, as explained in Sec. 6.1.2. Neutron stars can form for masses $\lesssim 15M_{\odot}$. Stars may become BHs with fallback for masses $15 \dots 20M_{\odot}$, and direct BHs for masses $\gtrsim 20M_{\odot}$. Thus, we find an overlap for masses around $15M_{\odot}$,

Fig. 1. from How Massive Single Stars End Their Life
 Heger et al. 2003 ApJ 591 288 doi:10.1086/375341
 http://dx.doi.org/10.1086/375341
 © 2003. The American
 Astronomical Society. All rights reserved. Printed in
 U.S.A.

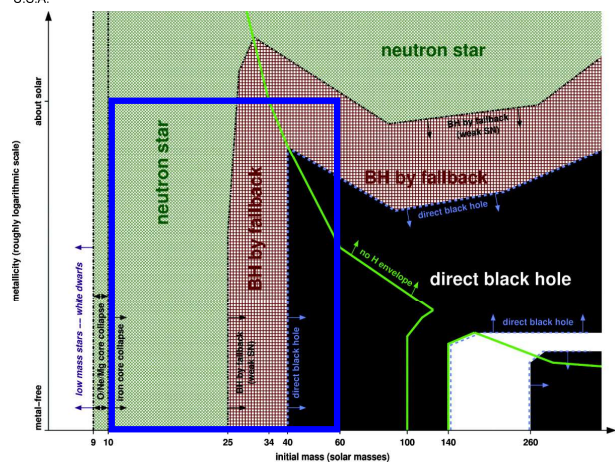


Figure 6.5: Figure from Heger et al. (2003), displaying the remnant types as a function of metallicity and initial mass. The blue box indicates the region of metallicities and initial masses corresponding to our calculations.

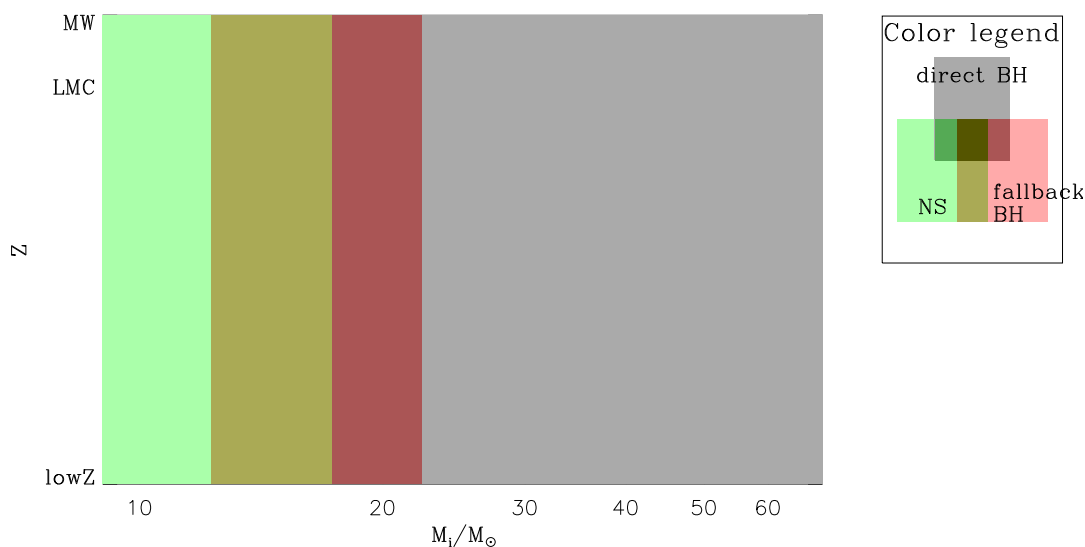


Figure 6.6: A diagram similar to Heger et al. (2003), Fig. 1. Remnant type depending on metallicity and initial mass. Values for other metallicities than indicated are only interpolations (see text). Mixed colors indicate overlap regions for different remnant types, because of uncertainties in the current physical (and numerical) description.

that can form both NSs and fallback BHs, depending on the physical assumptions. Models around $20M_{\odot}$ may form fallback or direct BHs. Nevertheless, the overlap region is comparatively small, and most models agree about the remnant type, even if the evolution, as well as final and core masses are different! As our maximum mass is $60M_{\odot}$, we do not find any pair instability SN, which only occurs for helium cores larger than $65M_{\odot}$ (Sec. 3.5.1)

In order to obtain a diagram with clearly distinct regions for the different remnant types, similar to Heger and Woosley, in Fig. 6.7 we display a diagram using only our current preferential models. These models have been calculated using the Ledoux criterion to define the convective boundary, mild rotation ($\Omega = 0.2\Omega_{crit}$, as indicated by Huang and Gies (2006) from observations), and magnetic fields in the Spruit-Tayler description. The mass loss rates of Vink, de Koter, and Lamers (2001) are reduced, and the bi-stability jump is corrected (our grid 3c). For lowZ, we reduce the de Jager, Nieuwenhuijzen, and van der Hucht (1988) mass loss rates, as described in Sec. 2.6. Again, values for other metallicities and initial masses than calculated are only zeroth order interpolations.

Consistent with Heger et al. (2003), we find that the transition between different remnant types is only weakly metallicity dependent. As Heger et al. argue, this can be explained by the weak dependence of the final core mass on the mass loss rates, that are the main difference between the metallicities. This dependence is even smaller for the carbon core masses compared to the helium core masses.

As our mass loss rates are smaller, our calculations effectively correspond to lower metallicities calculated by Heger and Woosley. In particular, our WR mass loss rates are reduced drastically. In addition, only stars more massive than $M_i = 20 \dots 25M_{\odot}$ form WR stars, which is higher than the limits between different remnant types. Thus, we do not observe strong changes in the remnant type at solar metallicity, in contrast to the results from Heger and Woosley. Instead, our models become direct BHs in almost all cases.

The remnant masses increase at lower metallicity, as can be concluded from the results presented in Chpt. 5.

The situation is different when the Woosley-formalism is used to calculate the remnant masses. While the remnant masses and types are only weakly affected at MW and LMC metallicity, drastic changes are visible for lowZ. This is consistent with our earlier findings concerning the differences between the two formalisms. We find that the remnant mass is decreased compared to higher metallicities in several cases! As stars at low metallicity do not lose their hydrogen rich envelope,

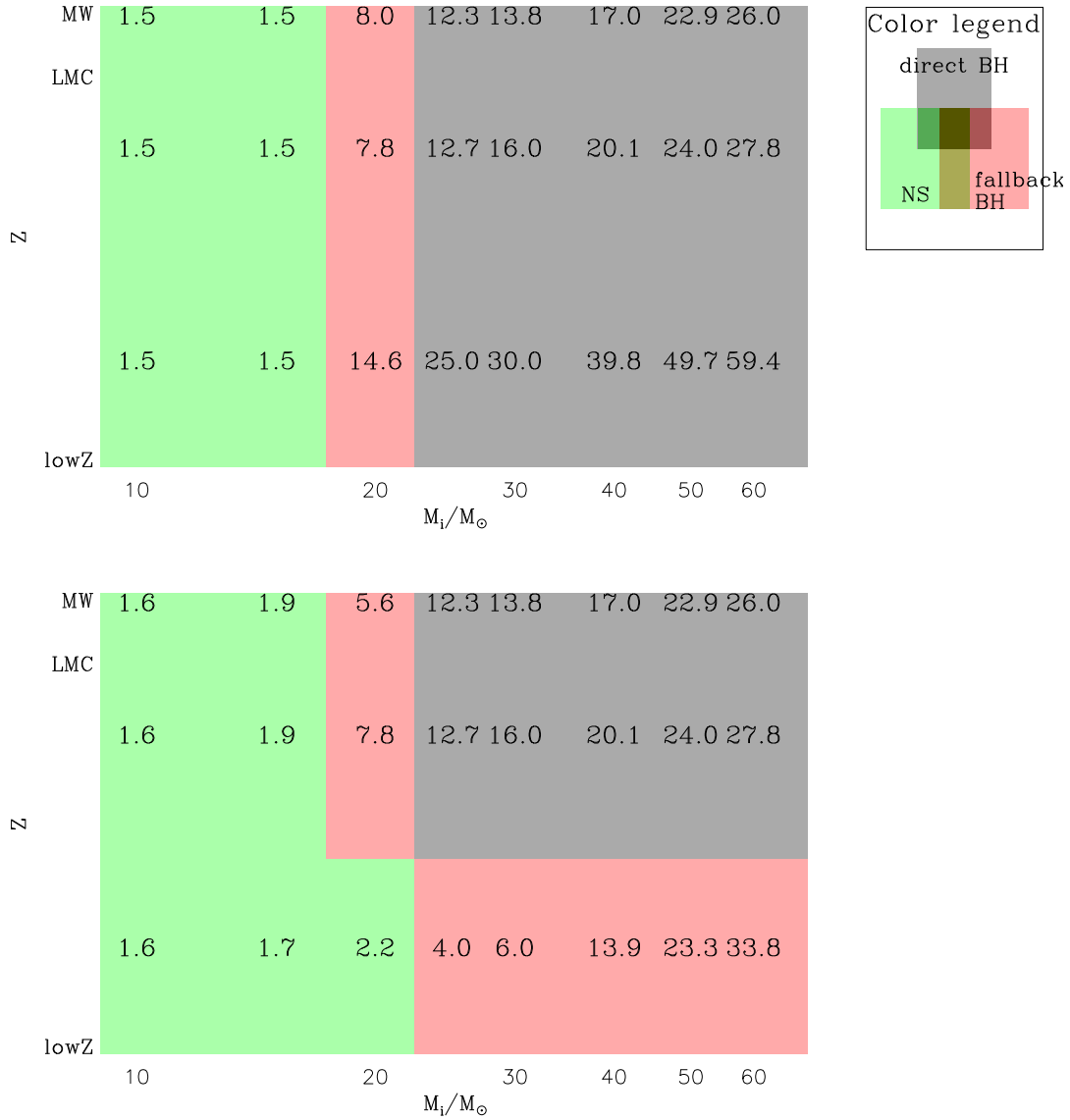


Figure 6.7: As Fig. 6.6, but only for our current preferential models (see text). Numbers indicate the mass of the corresponding remnant, resulting from our calculations. We provide the results both for the formalisms based on Woosley (upper) and Belczynski (lower).

and their final mass is purely determined by the helium core, they never become direct BHs. Instead, fallback BHs are formed.

6.3 Explosion types

In addition to the the remnant types, a comparison of the different explosion types can give a valuable basis for comparisons with observations. In Fig. 6.8, we show the results of Heger and Woosley (2002) for the explosion types, depending on initial mass and metallicity. A similar diagram for our results is shown in Fig. 6.9. Again, this covers a smaller region, and there can be overlaps between different explosion types, as explained in the previous section. In order to allow for a clear distinction, we changed the colors, as shown in the corresponding legend. All regions that are hatched may show no explosion, but a direct collapse (corresponding to the white region in Fig. 6.8).

For lower masses, the stars typically still have a hydrogen-rich envelope when they explode, such that they may explode as SNe type II. However, the rapidly rotating models with increased rotational mixing efficiency evolved towards the WR stage already for low initial masses, such that they explode as type I SN. As explained already, this is most likely not physical, and the real uncertainty in mixing coefficients is probably smaller. Thus, also the uncertainty in the explosion type would be reduced. Higher mass stars at MW and LMC metallicity become WRs, meaning they lost their hydrogen rich envelope. However, all stars more massive than $25M_{\odot}$ do not show any SN explosion but a collapse into a direct black hole.

This becomes clearer, when only looking at the current preferential model, which is shown in Fig. 6.10. Very similar to the original results of Heger and Woosley, we find that all models at lower masses explode as type II SN. There is a thin band of models that explode as type IIL/b, while the others explode as type IIp. As this band is thin, we may just have missed the corresponding initial mass at solar metallicity. The lower mass limit, where models have a direct collapse and thus no SN, is shifted towards lower initial masses. In contrast to Heger and Woosley, we find that for all metallicities, and especially also at MW metallicity, models with $M_i \gtrsim 20M_{\odot}$ have no SN, but a direct collapse. This is most likely related to the differences in overshooting.

The explosion type is determined by the hydrogen-rich envelope, such that it is independent of the calculated remnant mass. The only change we observe using the Woosley-formalism instead of the Belczynski one is that at lowZ fallback BHs form, such that we can observe explosions also at higher masses. As they experience only

Fig. 2. from How Massive Single Stars End Their Life
 Heger et al. 2003 ApJ 591 288 doi:10.1086/375341
 http://dx.doi.org/10.1086/375341
 © 2003, The American
 Astronomical Society. All rights reserved. Printed in
 U.S.A.

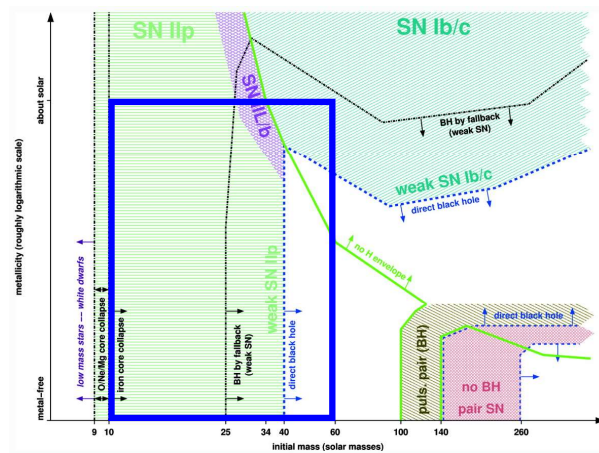


Figure 6.8: Figure from Heger et al. (2003), showing the explosion types as a function of metallicity and initial mass. The blue box indicates the region of metallicities and initial masses corresponding to our grid of evolutionary models.

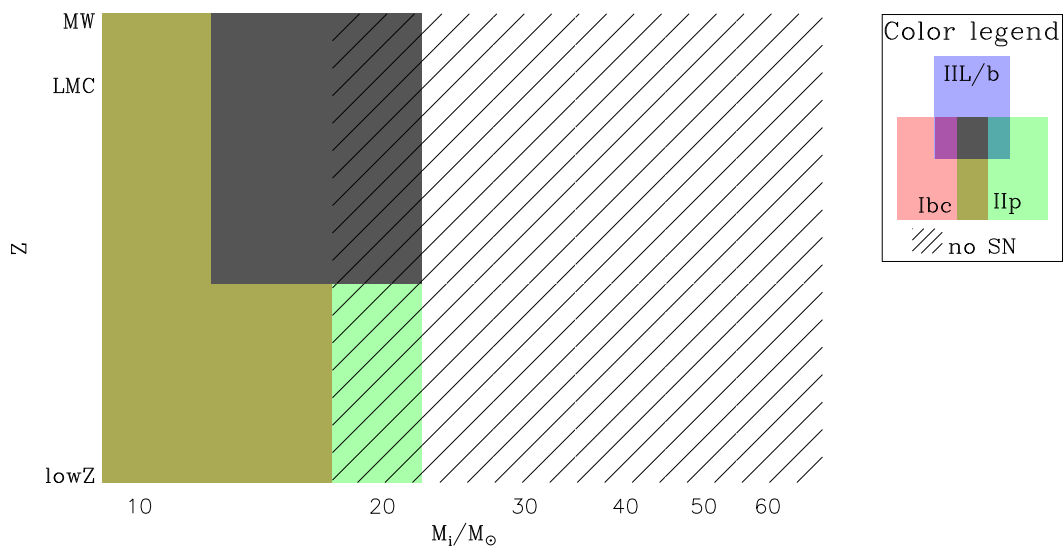


Figure 6.9: A diagram similar to Heger et al. (2003), Fig. 2. Remnant type depending on metallicity and initial mass. Values for other metallicities than indicated are only interpolations. Mixed colors indicate overlap between different explosion types because of uncertainties in the current physical (and numerical) description. The low mass models exploding as type I SN originate from WR stars due to rapid rotation in combination with increased rotational mixing, and are most likely not physical.

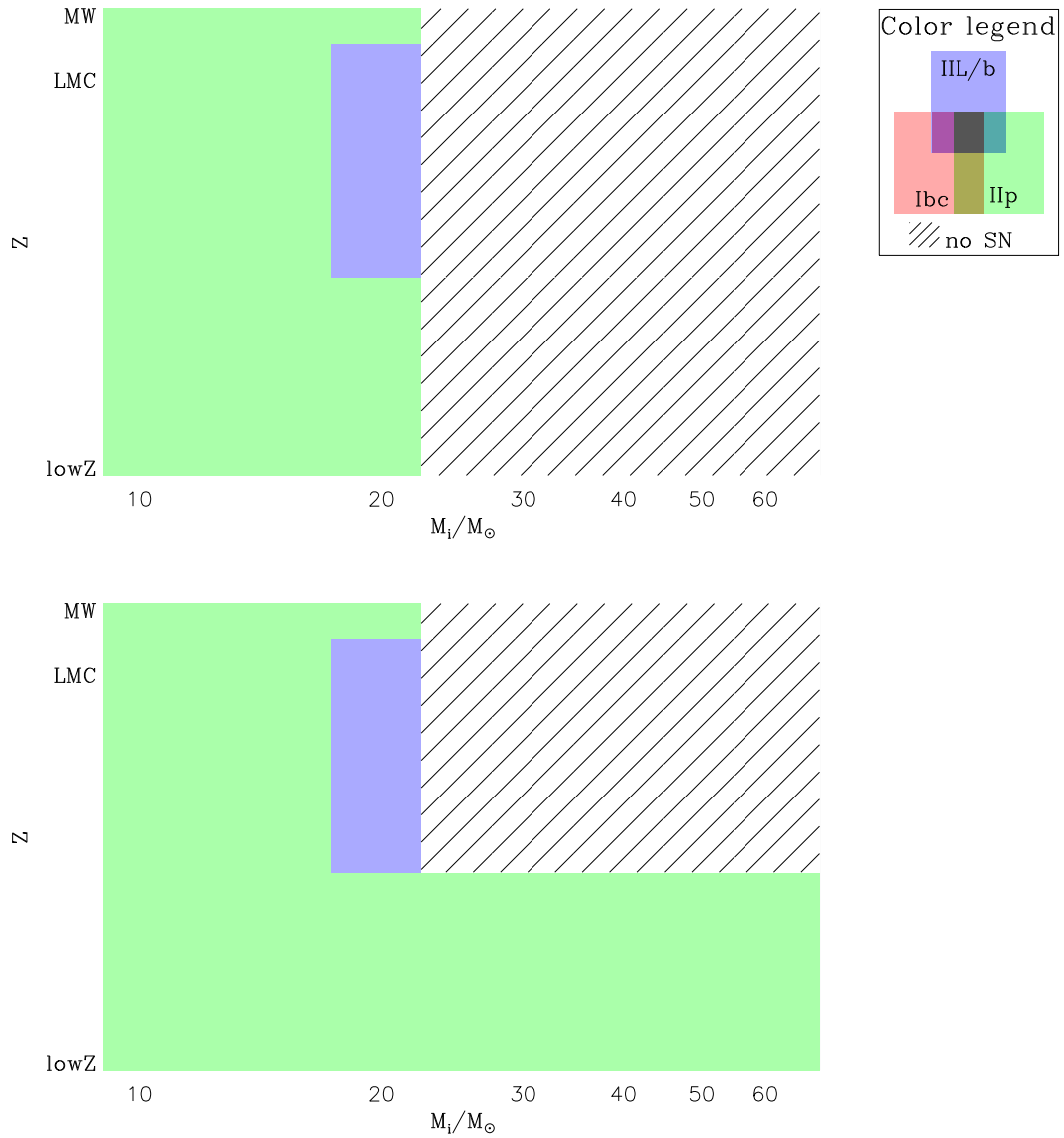


Figure 6.10: As Fig. 6.9, but only for the current preferential model. We provide the results both for the formalisms based on Woosley (upper) and Belczynski (lower).

very weak mass loss⁴, they explode as type IIp SN.

⁴We remind that here we discuss the grid with scaled down RSG mass loss, such that almost no mass loss is present.

6.4 Statistics for Microlensing

One aim of this thesis is to provide predictions that can be used for analysing microlensing observations. The theoretical background is beyond the scope of this thesis, an instructive summary has been provided by Wambsganss (2006) and Riffeser et al. (2006). As microlensing is a gravitational effect, the gravitational mass is observed instead of the baryonic one, and we have to convert the masses via Eqns. (3.3) and (3.4).

The microlensing probability is related to the fraction of mass available in compact remnants. The total mass that is present in remnants can be found by a convolution of the remnant mass relation with the initial mass function (**IMF**). Under the approximation of a single stellar population (**SSP**, valid, e.g., for the bulge of M31 – see below), and as massive stars live shorter than lower mass stars, a “turn-off mass” M_{TO} can be defined. Lower mass stars are still on the MS, while more massive stars evolved further. As the later timescales are short, all stars more massive than the turn-off mass have most likely turned into remnants. Thus, the ratio of dark remnants to luminous stars for a SSP can be approximated via

$$\frac{M_{rem,tot}}{M_{star,tot}} = \frac{\int_{M_{TO}}^{M_{max}} IMF(M_i) M_{rem}(M_i) dM_i}{\int_{M_{min}}^{M_{TO}} IMF(M_i) M_i dM_i}. \quad (6.1)$$

The cut-offs of the integration are defined by the minimum stellar mass M_{min} and the maximum mass of stars M_{max} . We adopt $M_{min} = 0.08M_{\odot}$ as a theoretical lower limit (Cohen 1988). The highest mass is still under debate, and we present solutions based on different values. Most likely, it is $M_{max} \gtrsim 100M_{\odot}$. Both values may also depend on the metallicity. Descriptions for the IMF can be found in various publications (see, e.g., the legend in Fig. 6.12).

The assumption of a single stellar population is reasonable for the bulge of M31, where stars only formed, with a time-independent IMF, in the first 1...2 Gyr, which is short compared to its age of $\mathcal{O}(10)$ Gyr (Stephens et al. 2003, Saglia et al. 2010, Saglia et al. 2018). For other systems, a more careful treatment is required. As ongoing star formation in younger stellar populations drastically changes the value of M_{TO} , one needs to integrate over different turn-off masses (corresponding to different times). Equation (6.1) only provides a lower limit in this case.

To calculate the remnant and luminous masses in Eqn. (6.1), we numerically

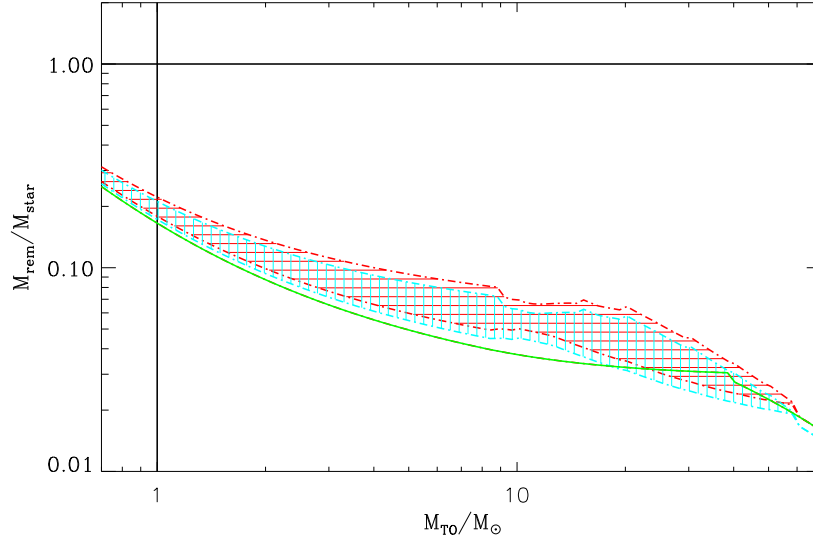


Figure 6.11: Ratio between mass included in compact remnants and visible mass, for a Salpeter (1955) IMF with $M_{\max} = 200M_{\odot}$ at MW metallicity. The **solid** line indicates the result when using the remnant mass relation provided by Renzini and Ciotti (1993). The hatched area represents the possible range of our results without the correction for the gravitational mass (**horizontal hatching**) and including the correction (**vertical hatching**). The changes due to the gravitational correction are very small. The vertical and horizontal lines at $M_{TO} = 1M_{\odot}$ and $M_{rem}/M_{star} = 1$ can be used for a better orientation in the plot. See text.

integrate over our grid using a five-point Newton-Cotes formula. For higher masses beyond the upper mass limit of our grid, we apply the BH-relation $M_{rem} = M_i/2$, based on the reasonable agreement with Renzini and Ciotti (1993) for higher masses. For lower masses, we assume that NSs form for $M_i \geq 8.5M_{\odot}$ (Renzini and Ciotti 1993), and WDs below. A relation for the remnant masses of WDs has also been provided by Renzini and Ciotti (1993).

In Fig. 6.11, we present our result for MW metallicity using the widely used Salpeter (1955) IMF. To obtain the full range of possible values, we include all models contained in our grids, as well as both formalisms to calculate the remnant masses. We restrict the analysis to a physically relevant range, given by the oldest existing populations, which have $M_{TO} \gtrsim 0.7 \dots 1M_{\odot}$, as can be concluded from isochrones based on PARSEC and COLIBRI⁵. The effect of the correction for the gravitational mass on the result is very small, far below the uncertainty range

⁵calculations by Bressan et al. (2012), Chen et al. (2014, 2014), Tang et al. (2014), Marigo et al. (2017), Pastorelli et al. (2019, 2020). The data is available online under <http://stev.oapd.inaf.it/cmd>

resulting from our various assumptions (grids).

As a comparison, the corresponding result for the remnant masses given by Renzini and Ciotti (1993) is shown. Our relation coincides with the result based on Renzini and Ciotti for $M_{TO} \geq 60M_{\odot}$, as we use the same relation for these masses. Also for the lowest turn-off masses considered, they approach each other, as the total remnant mass is dominated by the WDs due to the higher IMF weight for less massive stars.

The impact of our calculations can be clearly seen for intermediate masses $M_{TO} = 1 \dots 20M_{\odot}$. As we mostly predict higher remnant masses than Renzini and Ciotti, the ratio of remnant to stellar mass is increased in most cases. At higher turn-off masses $M_{TO} \approx 20 \dots 60M_{\odot}$, our results predict an uncertainty range around the relation based on Renzini and Ciotti. The general agreement at higher turn-off masses can be explained by the reasonable agreement of our relation and that of Renzini and Ciotti for initial masses $M_i \geq 40M_{\odot}$, that dominate the uncertainty. Indeed, there have been some models that produced slightly lower remnant masses than predicted by Renzini and Ciotti. Here the high mass black holes dominate the uncertainty range, even though the IMF in this range is lower.

We can conclude that our calculations mainly predict a higher total remnant-to-star ratio compared to the relation based on Renzini and Ciotti (1993), except for younger populations with high M_{TO} , where our calculations mainly predict the actual uncertainty range of this relation.

6.4.1 Constraining the IMF

Typically, when analysing microlensing observations, a certain IMF has to be assumed. However, by measuring the total mass of remnants via microlensing, measuring the visible mass directly, and using reliable stellar evolution models, one might obtain meaningful constraints on the IMF, similar to the work by Green (2016) and Niikura et al. (2019), who carried out observations to find a mass-function for primordial BHs.

Including different IMFs in our analysis, we find an overlap for most of them, especially at higher turn-off masses, as shown in Fig. 6.12. Even for the lowest turn-off masses, there is still a large uncertainty range. The problem of finding the IMF is degenerate when applying our (current) remnant mass relation.

To lower the uncertainty range, there is a need for better knowledge about the parameters determining stellar evolution. Especially, the main sources

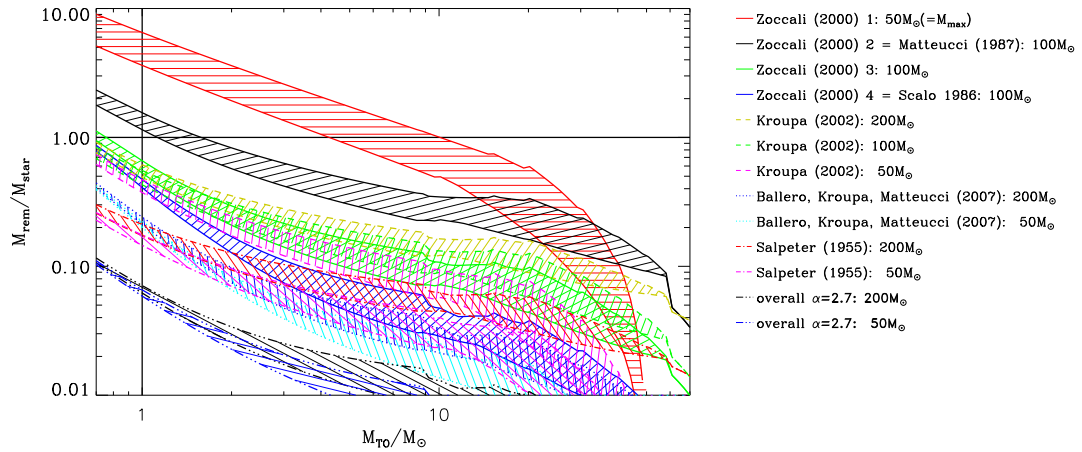


Figure 6.12: Ratio between mass included in compact remnants and visible mass, for different IMFs at MW metallicity. The range of possible values is indicated by the hatched regions.

of uncertainties, namely the choice of the convective boundary criterion, overshooting, and mass loss rates, need to be improved.

In addition to these imponderables in our theoretical considerations, MACHOS⁶ in the Halo would produce additional lensing events, and thus influence the measurement.

Already Riffeser, Seitz, and Bender (2008) concluded from their observed lensing events in the bulge of M31 that at least one event cannot be explained by star self-lensing. While they concluded that such events might be related to MACHOS, an alternative reason is lensing due to remnants instead.

With our remnant mass relations we are able to clearly rule out certain IMFs. For the bulge of M31 (with $M_{TO} \approx 1M_{\odot}$ and $Z \approx Z_{MW}$) Riffeser (2020, priv. comm.) argues that a factor 4...7 higher remnant masses are not seen in microlensing surveys. Especially, the Zoccali et al. (2000) IMF with $M_{\max} = 50M_{\odot}$ (solid line and enclosed region) would predict a very high total remnant mass. Most likely, the remnant mass is lower than the stellar mass, and also the Matteucci and Tornambe (1987) model (solid line and enclosed region) can be excluded.

These results are independent of the assumption of a single stellar population, as they require only an upper estimate of the remnant mass fraction. Thus far, only 56 lensing events have been found in M31 (Lee et al. 2015), such that further observations are necessary for improving the reliability of this result. Observing several thousand lensing events would be required to put tight constraints on the

⁶Massive Compact Halo Objects

shape of the IMF.

6.4.2 Different Metallicities

A similar analysis as for MW metallicities can be also performed for the other metallicities of our model grids. For lower metallicities, the maximum remnant masses, and thus the maximum possible ratio of total remnant to stellar mass, increases, as shown in Fig. 6.13. However, also the region of possible values becomes larger, and may even extend towards lower remnant mass fractions. While this effect is small when comparing our results for MW and LMC metallicity, it becomes obvious when analysing the lowZ data.

The high uncertainty range can be explained by two main reasons. The first is the difference between models with almost no mass loss and models where the mass loss is drastically enhanced by quasi-chemically homogeneous evolution. The second, and even more important source for uncertainties, is the difference between the two formalisms to estimate the remnant mass, as described in Sec. 6.1.3.

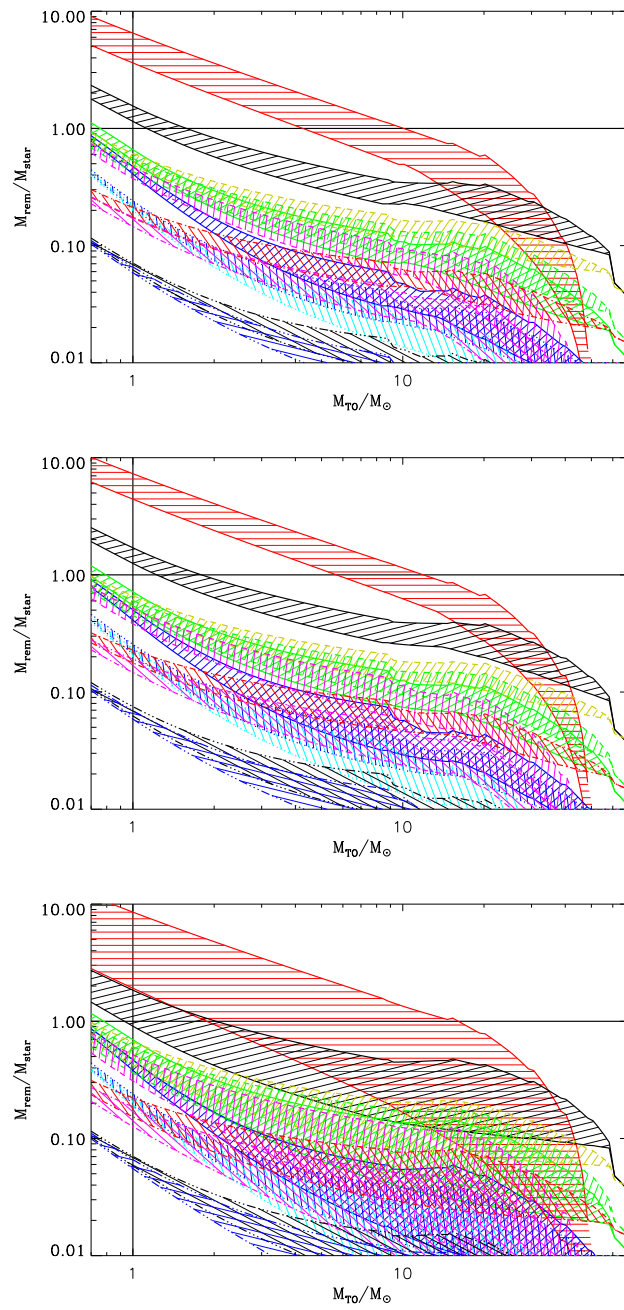


Figure 6.13: As Fig. 6.12, but comparing MW (top), LMC (middle), and lowZ (lower) metallicity.

7 Conclusion and Outlook

The final aim of this work was to find the end products of massive star evolution in dependence of the initial mass and the most important physical uncertainties. To accomplish this goal, we calculated model grids of stellar evolution with the MESA code up to carbon exhaustion. From this point on, we used different formalisms to link the progenitor properties to the corresponding remnant.

In Chpt. 2, we presented the most important physics for such calculations and the involved uncertainties. Most of the processes have to be approximated and formulated in a 1d description. Convection is included following the mixing length theory, where already the choice of the convective boundary criterion is still under debate. To take into account the finite velocity of the convective bubbles, convective overshooting has to be included. Different studies calibrate the overshooting parameter above the convective core, where such calibrations strongly depend on other physical assumptions, especially the applied mass loss rates. Finally, the efficiency parameters for rotational mixing have to be calibrated.

Magnetic fields can be measured in $\mathcal{O}(10)\%$ of massive stars. In MESA, they are implemented in the description of the Spruit-Tayler dynamo, which can reproduce some key findings, but has physical problems, and most likely does not work.

Mass loss rates of massive stars are still under discussion. Different descriptions have to be used, depending on the evolutionary stage. Recent observations and simulations suggest that the rates of Vink, de Koter, and Lamers (2001) may be too high. Especially, the bi-stability jump has to be shifted towards lower effective temperatures, and its role for the mass loss rates might be less important than previously thought. The metallicity scaling of the mass loss rates in the RSG regime is unknown, and adds a huge uncertainty at very low metallicities.

In order to understand how MESA works, and which parameters are important, we explored the impact of specific parameters in Chpt. 3. Four of them were discussed in more detail.

For the existence of the predicted μ -barrier, the smoothing of the composition gradient has to be avoided.

The choice of the overshooting parameter is not only important in the core, but too large values for the extension of the convective region below a shell can lead to significant problems, especially at lower metallicities or lower mass loss rates. Shell-undershooting mixes unprocessed material down into the core, and causes the convective shell to move down, until the core burning might be extinguished.

Finally, stars with a convective envelope during later evolutionary phases may evolve close to the Eddington-limit and become unstable. This can be avoided by increasing the convective efficiency with the help of the MESA module `MLT++`. In combination with the choice of the boundary criterion for the atmospheric pressure, these settings can drastically increase the stability of the calculations (though it might lead to somewhat unphysical solutions, by suppressing envelope inflation).

To explore the differences between MESA and other stellar evolution codes, we compared our simulations with results of Brott et al. (2011) and Ekström et al. (2012) who used the STERN and GENEC code, respectively. We found that the most crucial difference for non-rotating model is the implementation of the mass loss, and especially if the second bi-stability jump is included or not. In addition, the evolution of the $60M_{\odot}$ model close to the hook is highly parameter dependent. Effects of second order can have a huge impact for this model, as they decide if it crosses the second jump already on the main sequence. The actual behaviour could be revealed by analysing the convergence of the model by consecutively varying the timestep controls.

For rotating models, the treatment of angular momentum transport is crucial. While in MESA and STERN it is implemented as a purely diffusive process, Ekström et al. (2012) argue that it needs to be treated as an advective process instead. This can cause drastic differences.

For our main calculations, we set up a grid of stellar evolution models with different initial masses in the range from $10 \dots 60M_{\odot}$, and rotational velocities up to 0.4 of the critical value, as described in Chpt. 4. We calculated models at three metallicities, namely a very low one ($Z = 10^{-5}$), and LMC ($Z = 0.0047$) and MW ($Z = 0.014$) metallicity. In order to study the uncertainties, we varied the choice of the convective boundary criterion, the implementation of magnetic fields, the overshooting value, mass loss rates, and the rotational mixing coefficients.

Rotation can influence the surface abundances on the MS drastically.

Nevertheless, it only has a minor impact on the evolutionary path and on the final mass for MW and LMC metallicity. For most of the models, it decreases the luminosity due to the reduced effective gravity. Mixing processes are efficient enough to increase the luminosity only in a few rapidly rotating models, especially at lower metallicity or if mixing is increased. The low importance of rotation and the dominance of the effect reducing the luminosity can be explained by the slowdown of rotation already on the MS. As internal magnetic fields enforce a solid body rotation, the surface rotational velocity is higher and the effects of rotation increased when the Spruit-Tayler dynamo has been switched on.

In contrast, the choice of the convective boundary criterion adds an important uncertainty due to differences in the envelope convection after core hydrogen exhaustion. Models calculated using the Ledoux criterion undergo a dredge-up, but have smaller core masses compared to the Schwarzschild case. The different structure alters the later timescales, and results in strong differences in the final masses.

In addition, changing the mass loss rates can have drastic effects on the evolution. If the total mass loss is reduced, even at MW metallicity the highest mass stars considered do not become WR stars! Increasing the overshooting has the opposite effect, and shifts the lower mass limit for the formation of WR stars towards lower masses. Nevertheless, both, reduced mass loss rates and increased overshooting, result in increased core masses.

An increase in the rotational mixing efficiency can lead to extreme effects on the evolution. Rapidly rotating models even become WR stars for $M_i = 10M_\odot$ via QCHE independent of the metallicity, which is most likely not physical.

WR stars that formed via QCHE, as well as “classical” ones, show a convergence of final and core masses, as the core is uncovered. In addition, the final and remnant masses depend only weakly on their earlier evolution, due to the specific behaviour of their mass loss rates.

The remnant mass at all metallicities follows the same systematics as the core masses. Regarding the metallicity, the remnant mass is increased for lower values. Also the spread becomes much larger. One reason is the difference between models without almost any mass loss and others, that still undergo mass loss during the RSG phase. The main source for uncertainties at low metallicities, however, is the formalism used to predict the remnant mass!

Comparing our remnant masses with other studies, we find a surprising agreement with the relation by Renzini and Ciotti (1993) for the highest mass

stars, that end as WR stars. For smaller mass stars, we find higher remnant masses. The main differences to the simulations by Woosley, Heger, and Weaver (2002) and Heger and Woosley (2002) is the treatment of overshooting and mass loss, especially in the WR regime. We conclude that using modern calculations and state-of-the-art physical assumptions, our predictions for remnant masses at MW metallicity are considerably larger than those predictions, for a wide range of initial masses.

Subsequently, we have presented diagrams displaying the remnant and explosion types depending on metallicity and initial mass. We provide diagrams including the derived uncertainties, and thus with overlap regions between different types, and alternative diagrams for our current preferential model with clearly distinct regions. The uncertainty regions are relatively narrow, and much smaller than expected from the large number of uncertain parameters.

As for the remnant masses, we find a shift of the different regions towards lower initial masses compared to the results of Heger et al. (2003), due to overshooting. Except for this shift, all our results are very similar to those of Heger et al. (2003). Especially, the remnant type is (almost) independent of the metallicity. This bases on the weak importance of mass loss rates (being the main difference between the metallicities) for the final carbon core masses. WR stars might change this behaviour at higher metallicities, however we apply drastically reduced WR mass loss rates compared to Heger et al., and they only form for higher masses than where the transitions between different types occur. We thus also observe this metallicity-independence at MW metallicity.

Finally, we discussed the total mass fraction of remnants compared to the luminous stellar mass, in dependence of the initial mass function. Knowledge of this relation is especially relevant for interpreting microlensing events. We find a large uncertainty range and overlap between different IMFs. The uncertainty range increases for lower metallicities, mainly due to the uncertainty in the formalism to predict the remnant mass from the progenitor properties. Nevertheless, this diagram can be useful to rule out specific IMFs via present and future observations.

Outlook

The results presented in this work should be permanently revised and updated, if sources for uncertainties can be reduced or improved stellar evolution models are

available. The limits presented by us have to be understood as current, reasonable ranges.

The descriptions for mass loss rates are strongly under discussion, with many recent results, that will probably allow to better constrain the mass loss. Not only the rates for non rotating models have to be improved, but also the behaviour of mass loss with rotation. A possible solution might be two-dimensional models (e.g. the ESTER code, Gagnier et al. 2019), that can treat the impact of rotation with less approximations. The best would be full 3d simulations, which will, however, be not available in the near future.

One of the most important open questions that will most likely remain unsolved in the near future is the description of mass loss during the LBV phase.

As the calibrations of several parameters depend on other physical assumptions, primarily on the applied mass loss description, they may become more reliable in parallel with increased knowledge about mass loss rates.

In order to reduce the uncertainties of the remnant-linking at lower metallicities, further studies of the late evolution until iron core formation are necessary.

In addition to possible improvement, our grid should be extended towards higher and lower initial masses. For the results relevant for microlensing, especially the lower mass range is of great importance, such that we do not need to rely on the relations presented by Renzini and Ciotti, but also find the potential range for remnant masses.

As several microlensing observations are carried out in M31, also an extension of our grids towards higher metallicities could be useful.

Finally, a more detailed analysis of the surface abundances, the impact of the different parameters, and the corresponding uncertainties on the MS, in combination with spectroscopic observations, will allow us to provide further constraints on the physical assumptions and processes.

A Massive Star Evolution with MESA – Set-Up and Technical Aspects

A.1 EOS, Opacities, Nuclear Reaction Rates

The MESA equation of state is a blend of the OPAL (Rogers and Nayfonov 2002), SCVH (Saumon, Chabrier, and van Horn 1995), PTEH (Pols et al. 1995), HELM (Timmes and Swesty 2000), and PC (Potekhin and Chabrier 2010) equations of state.

Radiative opacities are primarily from OPAL (Iglesias and Rogers 1993, 1996), with low-temperature data from Ferguson et al. (2005) and the high-temperature, Compton-scattering dominated regime by Buchler and Yueh (1976). Electron conduction opacities are from Cassisi et al. (2007).

Nuclear reaction rates are from JINA REACLIB (Cyburt et al. 2010) plus additional tabulated weak reaction rates (Fuller, Fowler, and Newman 1985, Oda et al. 1994, Langanke and Martínez-Pinedo 2000). Screening is included via the prescription of Chugunov, Dewitt, and Yakovlev (2007). Thermal neutrino loss rates are from Itoh et al. (1996).

A.2 MESA setup

A.2.1 Installation and first steps

We use MESA version 12115¹ together with MESA SDK version 20190830². For the installation, we followed the description on the MESA webpage³, where all requirements are listed as well. As MESA is programmed in Fortran (partly including 2003 standard), an up-to-date compiler is necessary for the installation, which is distributed within the SDK.

To become familiar with MESA, the tutorial is an excellent starting point, published on the MESA webpage⁴. This does not only teach how to change the settings, but also some basic knowledge about the in-build analysis routines. Settings useful for the calculations of a specific model can be found in the `test_suite` examples. However, settings often have to be adjusted to more physical values.

A.2.2 Starting our project

The `black_hole test_suite` provided a good foundation for our work, because of several reasons: First, it contains the necessary settings and is designed for the calculation of a high mass star, while many other examples are designed to tackle the evolution of low mass stars. Since these evolve differently, only high mass stars with at least $8M_{\odot}$ are relevant for our work. Second, the evolution includes also later phases, which is advantageous compared to the `high_mass test_suite`, from which we started initially. Especially these later phases after the MS require a careful choice of numerical and physical parameters. Third, `black_hole` includes rotation. This is the main advantage over `ppisn` which also fulfills the first two criteria from above.

In addition, we combine settings from inlists provided by Z. Keszthelyi⁵ and by Eva SEXTL (2019, priv. comm.). Our final inlists are provided in App. A.4.

¹All versions are available online under <https://sourceforge.net/projects/mesa/files/releases/>

²Information and releases available online under <http://www.astro.wisc.edu/~townsend/static.php?ref=mesasdk>

³<http://mesa.sourceforge.net/>

⁴<http://mesa.sourceforge.net/starting.html>

⁵available under <https://doi.org/10.5281/zenodo.3250412>

A.2.3 Visualisation and Troubleshooting

A first impression on how the calculation proceeds can be gained using the MESA module `pgstar`. It contains a variety of options and diagrams that might be displayed. These can also be saved as images (typically in the png format, but also pdf is possible) for a later analysis. All options relevant for the creation of diagrams can be changed during the run. However, for a detailed analysis and comparison of different models, more advanced plotting routines are useful. MESA offers routines programmed in python⁶. However, we chose to do our analysis in IDL, also based on existing routines, described in Sec. B.1.

If problems of any kind occur during the calculations, a helpful guide for solving them is provided on the MESA webpage.⁷ For more specific questions about the implementation of physical aspects, we advise to consult the MESA instrument papers (Paxton et al. 2011, 2013, 2015, 2018, 2019). As well, the MESA mailing list archive⁸ contains solutions for various specific problems. In addition, a closer look on the output data and different diagrams can give enlightening hints, at which time the problematic behaviour begins and what the reason might be.

A.3 Settings for Our Calculations with MESA

For different evolutionary stages, the settings have to be adjusted. Different `test_suites` contain scripts that can execute a MESA run with different inlists, depending on the evolutionary stage. For the purpose of modifying the settings, the MESA calculation is interrupted. However, these runs use “restart-models”, which only contain limited information about the complete model. When loading a model, the later run is affected by that interruption. In order to restart without a loss of information, we use “photos” instead, that contain all information necessary for the run.⁹

The different parts of the evolution are combined using a Linux bash script. This script is especially designed to run a grid of models, where all possible parameters can be varied.

We take advantage of the different possibilities to parallelize the calculation. At first, a single instance of MESA can make efficient use of multiple threads,

⁶<http://mesa.sourceforge.net/output.html#python>

⁷<http://mesa.sourceforge.net/troubleshooting.html>

⁸<https://lists.mesastar.org/pipermail/mesa-users/>

⁹A comparison of the MS evolution of models after restart with photo and model at the ZAMS has been provided by Ferraro (2020).

as discussed further in App. A.6. This is done by setting the system variable `OMP_NUM_THREADS`. We chose the optimum number of 16. In addition, several instances of MESA can be executed in parallel¹⁰. MESA has been designed in a thread save way, however one has to take care of the system requirements described in Sec. 4.3!

A.3.1 Structure of Inlists

The inlists are contained within the `inlist/` directory and are split in the following way:

- `inlist` (main inlist) includes the following inlists:
 - `inlist_massive_defaults`
 - `inlist_common`
 - `inlist_Z_abundances`, where Z has to be replaced with `mw`, `lmc`, `lowz`
 - `inlist_massive_stars` (adopted as a general name for simplicity; the original name is `inlist_to_X` with different phases X) includes the following inlists:
 - * `inlist_after_zams_general`, used for all phases from the ZAMS on (as the name suggests)
 - * `inlist_to_X_common`
 - * `inlist_to_X_values`, copied to the directory of the individual run

The inlists written with red color are copied inside the directory of each run, while all other inlists are fixed and stay inside the `inlists/` directory, and thus are used for all runs.

The execution is split into different evolutionary stages:

- pre-MS (`inlist_to_zams`),
- MS (`inlist_to_he_zams`),
- until central helium exhaustion (`inlist_to_he_tams`), and
- until central carbon exhaustion (`inlist_to_c_burn`)

¹⁰Discussions on the optimal use of multiple threads can also be found on the MESA mailing list.

and corresponding inlists with appendices `_common` and `_values` (replacing the `X` from the previous list).

Each of the inlists `inlist_to_X_common` contains a stopping condition. When all models finished the calculation of a certain phase, the last photos are used for a restart, where the phase-specific inlists are exchanged with those for the next phase. After central carbon exhaustion, the script continues with some basic data analysis. As the calculation proceeds automatically, all inlists should be provided before starting a run.

A.3.2 Setup and Execution

For running a grid of models within our approach, the following has to be prepared:

1. The abundance can be chosen by using the corresponding inlist (see above).
2. All other inlists may also be adjusted if necessary.
3. The inlists used for different parts of the evolution, `inlist_to_X_values`, have to be manipulated. Placeholders can be inserted, which should be varied during the run. `<<PLACEHOLDER>>` is replaced by the different values.
4. The list of values for the placeholders is provided in `models.dat` and `pms_models.dat`. Placeholders are given in the first line of the two files (same order in both files). As, e.g., rotation is activated only after the pre-MS, `models.dat` can contain more placeholders. In the following lines, the values are specified. We note that an empty line at the end has to be inserted.
5. The parallelisation has to be adjusted inside
 - `run_parallel`: `OMP_NUM_THREADS` (threads used by a single MESA instance) and
 - `run_all_mesa`: `parallel_runs` (number of MESA instances executed in parallel).
6. The execution is started by `run_parallel`.

In addition to the routines necessary for the run, we created additional routines for easy clean-up, storage reduction and data analysis. For sake of brevity, we will not discuss these in more detail.

A.4 Inlists

As described in Sec. A.3.1, we use different inlists for our MESA calculations.

Each inlist is divided into three sections. The first section `star_job` contains mainly settings that are necessary to set up the model and initialise the run. It is followed by the `controls` section, which contains the majority of the physical and numerical parameters. The third section is responsible for manipulating the visualisation with `pgstar` (as long as it is activated in the first section), and omitted in our inlists.

The `inlist_massive_default` is distributed together with the MESA version. In the following, we will provide all other inlists.

A.4.1 Abundances

MW

```
&star_job
```

```
!***** initial Abundances *****
```

```
initial_zfracs = 8 ! Asplund 2009 corrected (see chem/public/chem_def)
```

```
initial_h1 = 0.715
```

```
initial_h2 = 0
```

```
initial_he3 = 0
```

```
initial_he4 = 0.271
```

```
/ !# end of starjob namelist
```

```
&controls
```

```
!***** initial Mass/initial_z etc. *****
```

```
initial_z = 0.014 ! Pryzbilla
```

```
Zbase = 0.014
```

```
initial_y = 0.271
```

```
/ !# end of controls namelist
```

LMC`&star_job``!***** initial Abundances *****``initial_zfracs = 0 ! define them in controls``initial_h1 = 0.7391``initial_h2 = 0``initial_he3 = 0``initial_he4 = 0.2562``/ !# end of star_job namelist``&controls``!***** initial Mass/initial_z etc. *****``initial_z = 0.0047``Zbase = 0.0047``initial_y = 0.2562``z_fraction_Be = 0``z_fraction_B = 0``z_fraction_C = 0.1022``z_fraction_N = 0.0168``z_fraction_O = 0.5428 ! + 1 at last digit for sum``z_fraction_F = 0``z_fraction_Ne = 0.0835``z_fraction_Na = 0.0021``z_fraction_Mg = 0.0408``z_fraction_Al = 0.0038``z_fraction_Si = 0.0672``z_fraction_P = 0.0004``z_fraction_S = 0.0266``z_fraction_Cl = 0.0007``z_fraction_Ar = 0.0037``z_fraction_K = 0.0003`

```
z_fraction_Ca = 0.0049
z_fraction_Sc = 0
z_fraction_Ti = 0.0002
z_fraction_V = 0
z_fraction_Cr = 0.0014
z_fraction_Mn = 0.0008
z_fraction_Fe = 0.0952
z_fraction_Co = 0.0003
z_fraction_Ni = 0.006
z_fraction_Cu = 0.0001
z_fraction_Zn = 0.0002

/ !# end of controls namelist

lowZ

&star_job

!***** initial Abundances *****

initial_zfracs = 8 ! Asplund 2009 corrected (see chem/public/chem_def)
initial_h1 = 0.75229
initial_h2 = 0
initial_he3 = 0
initial_he4 = 0.2477

/ !# end of starjob namelist
&controls

!***** initial Mass/initial_z etc. *****

initial_z = 1.d-5
Zbase = 1.d-5
initial_y = 0.2477

/ !# end of controls namelist
```

A.4.2 inlist_common

```
&star_job
```

```
eos_file_prefix = 'mesa'
```

```
kappa_file_prefix = 'gs98' ! inlist_massive_defaults
```

```
/ !# end of star_job namelist
```

```
&controls
```

```
use_eps_mdot = .false.
```

```
dedt_eqn_r_scale = 0d0 ! <= 0 means use old scheme
```

```
!radiation pressure at boundary
```

```
Pextra_factor = 2 ! important near eddington limit
```

```
!***** EOS *****
```

```
use_eosDT2 = .true. !default
```

```
use_eosELM = .true. !default
```

```
!***** SOLVER *****
```

```
use_gold_tolerances = .true. !default
```

```
scale_max_correction = 0.2d0
```

```
ignore_species_in_max_correction = .true.
```

```
smooth_convective_bdy = .false. ! avoid numerical changes in composition.
```

```
!***** ROTATION / MIXING *****
```

```
use_Ledoux_criterion = .true.
```

```
alpha_semiconvection = 0.1
```

```
semiconvection_option = 'Langer_85'
```

```
num_cells_for_smooth_gradL_composition_term = 0

! + 'D_DSI' = dynamical shear instability
! + 'D_SH' = Solberg-Hoiland
! + 'D_SSI' = secular shear instability
! + 'D_ES' = Eddington-Sweet circulation
! + 'D_GSF' = Goldreich-Schubert-Fricke
! + 'D_ST' = Spruit-Tayler dynamo

!## Diffusion coefficients for chemical mixing
D_DSI_factor = 0      ! only late pre-SN phases
D_SSI_factor = 1
D_SH_factor = 1
D_GSF_factor = 1
D_ES_factor = 1
D_ST_factor = 0 ! no transport of elements due to magnetic fields

!## Diffusion coefficients for angular momentum transport set
am_nu_visc_factor = 0      ! timescale > hubble time
am_nu_ST_factor = 1       ! magnetic field
am_nu_factor = 1
am_D_mix_factor = 0.0333333d0
am_gradmu_factor = 0.05 ! default

mixing_length_alpha = 1.5
MLT_option = 'Mihalas'

recalc_mixing_info_each_substep = .true.

!***** MESH *****

mesh_delta_coeff = 0.6
mesh_delta_coeff_for_highT = 0.6

max_dq = 1d-3 ! -3 from zsolt, so at least 1000 cells.
```

```
! avoid over-resolving composition changes
min_dq_for_xa = 1d-4

logT_max_for_standard_mesh_delta_coeff = 9.0
logT_min_for_highT_mesh_delta_coeff = 9.5

! from zsolt, important for avoiding problems near Eddington limit
max_q_for_k_const_mass = 0.98
min_q_for_k_const_mass = 0.98

!***** MLT++ *****

! important for avoiding problems near Eddington limit
gradT_excess_age_fraction = 0.95
gradT_excess_max_change = 0.001

!***** TIMESTEP *****

varcontrol_target = 7d-4 !3d-4 !7d-4

delta_lgRho_cntr_limit = 1.2d-2
delta_lgT_cntr_limit = 2.0d-3
dX_nuc_drop_limit_at_high_T = 2d-3

delta_lgR_limit = 0.05
delta_HR_limit = 0.05
delta_HR_hard_limit = 0.1

relax_hard_limits_after_retry = .false.

delta_lgL_nuc_limit = 0.2

delta_lg_XH_cntr_max = 0.0
delta_lg_XH_cntr_min = -6.0
delta_lg_XH_cntr_limit = 0.01d0
```

```
delta_lg_XHe_cntr_max = 0.0
delta_lg_XHe_cntr_min = -6.0
delta_lg_XHe_cntr_limit = 0.01d0

delta_lg_XC_cntr_max = 0.0d0
delta_lg_XC_cntr_min = -6.0d0
delta_lg_XC_cntr_limit = 0.01d0

!***** WIND *****

cool_wind_RGB_scheme = 'Dutch'
cool_wind_AGB_scheme = 'Dutch'

hot_wind_scheme = 'Dutch'

use_other_wind = .true.

Dutch_scaling_factor = 1.0
Vink_scaling_factor = 1.0
x_ctrl(20) = -1 ! Jump temperature, use Vink prescription for <= 0

x_ctrl(21) = 0 ! exponent for metallicity scaling of de Jager rates

cool_wind_full_on_T = 0.8d4
hot_wind_full_on_T = 1.2d4

max_mdot_redo_cnt = 100
surf_w_div_w_crit_limit = 0.96d0
surf_w_div_w_crit_tol = 0.05d0
mdot_revise_factor = 1.2d0

!***** OVERSHOOTING *****

! offset
overshoot_f0_above_nonburn_core = 0.01
```

```
overshoot_f0_above_nonburn_shell = 0.01
overshoot_f0_below_nonburn_shell = 0.01
```

```
overshoot_f0_above_burn_h_core = 0.01
overshoot_f0_above_burn_h_shell = 0.01
overshoot_f0_below_burn_h_shell = 0.01
```

```
overshoot_f0_above_burn_he_core = 0.01
overshoot_f0_above_burn_he_shell = 0.01
overshoot_f0_below_burn_he_shell = 0.01
```

```
overshoot_f0_above_burn_z_core = 0.01
overshoot_f0_above_burn_z_shell = 0.01
overshoot_f0_below_burn_z_shell = 0.01
```

```
! exponential
```

```
overshoot_f_above_nonburn_core = 0.0
overshoot_f_above_nonburn_shell = 0.0
overshoot_f_below_nonburn_shell = 0.0
```

```
overshoot_f_above_burn_h_core = 0.0
overshoot_f_above_burn_h_shell = 0.0
overshoot_f_below_burn_h_shell = 0.0
```

```
overshoot_f_above_burn_he_core = 0.0
overshoot_f_above_burn_he_shell = 0.0
overshoot_f_below_burn_he_shell = 0.0
```

```
overshoot_f_above_burn_z_core = 0.0
overshoot_f_above_burn_z_shell = 0.0
overshoot_f_below_burn_z_shell = 0.0
```

```
! step
```

```
step_overshoot_f_above_nonburn_core = 0.345
step_overshoot_f_above_nonburn_shell = 0.!345
step_overshoot_f_below_nonburn_shell = 0.!345
```

```
step_overshoot_f_above_burn_h_core = 0.345
step_overshoot_f_above_burn_h_shell = 0.!345
step_overshoot_f_below_burn_h_shell = 0.!345

step_overshoot_f_above_burn_he_core = 0.345
step_overshoot_f_above_burn_he_shell = 0.!345
step_overshoot_f_below_burn_he_shell = 0.!345

step_overshoot_f_above_burn_z_core = 0.345
step_overshoot_f_above_burn_z_shell = 0.!345
step_overshoot_f_below_burn_z_shell = 0.!345

! helps with off center ignition in progenitor
!2nd scale length for exponential overshooting
overshoot_f2_below_burn_z = 0.10
overshoot_D2_below_burn_z = 1d10 !initial diffusion coefficient

!***** STOPPING CONDITION *****

when_to_stop_rtol = 1d-3
when_to_stop_atol = 1d-3

!***** OUTPUT *****

profile_interval = 10
max_num_profile_models = 10000

history_interval = 1

terminal_interval = 100
write_header_frequency = 500
photo_interval = 5000

! definitions of core boundaries
he_core_boundary_h1_fraction = 0.5
```

```
c_core_boundary_he4_fraction = 0.5
o_core_boundary_c12_fraction = 0.5
si_core_boundary_o16_fraction = 0.5
fe_core_boundary_si28_fraction = 0.33
```

```
/ !# end of controls namelist
```

A.4.3 Phase-Specific

Pre-MS

common

```
&star_job
```

```
create_pre_main_sequence_model = .true.
```

```
write_profile_when_terminate = .false. !default
```

```
set_uniform_initial_composition = .true.
```

```
!***** ROTATION ACTIVATION *****
```

```
! no rotation before zams
```

```
change_rotation_flag = .true.
```

```
new_rotation_flag = .false.
```

```
/ !# end of starjob namelist
```

```
&controls
```

```
max_number_backups = 0
```

```
max_number_retries = 0
```

```
max_model_number = 5000
```

```
!***** TIMESTEP *****
```

```
varcontrol_target = 7d-4
```

```
x_integer_ctrl(1) = -1 ! no varcontrol increase
```

```
x_integer_ctrl(3) = -1 ! no varcontrol increase

!***** STOPPING CONDITION *****

Lnuc_div_L_upper_limit = 0.9

!***** OUTPUT *****

warn_when_large_rel_run_E_err = 1d99 ! off until reach zams

x_logical_ctrl(1) = .false. ! do varcontrol debugging
x_integer_ctrl(5) = 0 ! minimum counter for varcontrol debugging

/ !# end of controls namelist

values

&star_job

/ !# end of starjob namelist
&controls

!***** INITIAL MODEL *****

initial_mass = <<MASS>>

!***** OTHER *****

use_Ledoux_criterion = .<<LEDOUX>>.
alpha_semiconvection = 0.1

/ !# end of controls namelist

MS

common

&star_job
```

```
set_initial_cumulative_energy_error = .true.
new_cumulative_energy_error = 0d0

!***** ROTATION ACTIVATION *****

! activate rotation from now on
new_rotation_flag = .true.
change_rotation_flag = .true.

! rotational velocity in km sec-1
!new_surface_rotation_v = 0
!relax_surface_rotation_v = .true.

! omega in units of critical rotation
new_omega_div_omega_crit = 0.0
relax_omega_div_omega_crit = .true.

! use this many steps to change value
num_steps_to_relax_rotation = 100

/ !# end of star_job namelist
&controls

!***** STOPPING CONDITION *****

xa_central_lower_limit_species(1) = 'h1'
xa_central_lower_limit(1) = 1d-3

/ !# end of controls namelist

values

&star_job

!***** ROTATION ACTIVATION *****
```

```
!new_surface_rotation_v = <<VROT>>
new_omega_div_omega_crit = 0.<<OMEGA>>

/ !# end of star_job namelist
&controls

!***** OTHER *****

use_Ledoux_criterion = .<<LEDOUX>>.
alpha_semiconvection = 0.1

am_nu_ST_factor = <<ST>>

/ !# end of controls namelist

Until Central Helium Exhaustion

common

&star_job

/ !# end of star_job namelist
&controls

!***** STOPPING CONDITION *****

xa_central_lower_limit_species(1) = 'he4'
xa_central_lower_limit(1) = 1d-3

/ !# end of controls namelist

values

&star_job

/ !# end of star_job namelist
&controls
```

```
!***** OTHER *****
```

```
use_Ledoux_criterion = .<<LEDOUX>>.
```

```
alpha_semiconvection = 0.1
```

```
am_nu_ST_factor = <<ST>>
```

```
/ !# end of controls namelist
```

Until Central Carbon Exhaustion

```
common
```

```
&star_job
```

```
/ !# end of star_job namelist
```

```
&controls
```

```
!***** STOPPING CONDITION *****
```

```
xa_central_lower_limit_species(1) = 'c12'
```

```
xa_central_lower_limit(1) = 1d-3
```

```
/ !# end of controls namelist
```

```
values
```

```
&star_job
```

```
/ !# end of star_job namelist
```

```
&controls
```

```
!***** OTHER *****
```

```
use_Ledoux_criterion = .<<LEDOUX>>.
```

```
alpha_semiconvection = 0.1
```

```
am_nu_ST_factor = <<ST>>
```

```
/ !# end of controls namelist

inlist_after_zams_general

&star_job

logT_for_conv_vel_flag = 8.5d0

/ ! end of star_job namelist
&controls

max_number_backups = -1 !300 ! no limit
max_number_retries = -1 !3000 ! bo limit
max_model_number = 20000

!***** INITIAL MODEL *****

! set inside abundace and to_zams inlist.

!***** SOLVER *****

gold_iter_for_resid_tol3 = 10
gold_tol_residual_norm3 = 1d-6
gold_tol_max_residual3 = 1d-3

ignore_too_large_correction = .true.

!***** STRUCTURE EQUATIONS *****

use_dedt_form_of_energy_eqn = .true.
min_energy_for_dedt_form_of_energy_eqn = 1d13
min_cell_energy_fraction_for_dedt_form = 1d-10

!***** TIMESTEP *****

limit_for_rel_error_in_energy_conservation = 1d-4
```

```

x_integer_ctrl(1) = 0 ! initialise counter for varcontrol increase
x_integer_ctrl(2) = 1000 ! number of steps when to reduce
x_ctrl(1) = 5e-5 ! maximum dHR when to start counter
x_ctrl(2) = 5 ! increase factor
x_integer_ctrl(3) = 0 ! initialise counter for varcontrol increase 2
x_integer_ctrl(4) = 1500 ! number of steps when to reduce 2
x_ctrl(3) = 1.3e-4 ! maximum dHR when to start counter 2
x_ctrl(4) = 5 ! increase factor 2

!***** WIND *****

max_tries_for_implicit_wind = 0 ! 20
iwind_tolerance = 1d-3
iwind_lambda = 1 ! 0.5d0
max_T_center_for_any_mass_loss = 1.1d9

!***** OUTPUT *****

warn_when_large_rel_run_E_err = 1d99 ! off

x_logical_ctrl(1) = .false. ! do varcontrol debugging
x_integer_ctrl(5) = 0 ! minimum counter for varcontrol debugging

/ ! end of controls namelist

```

A.4.4 Different Grids

For calculating the different grids we had to alter the `inlist_common`. In the following, we will provide the changes.

Grid 2

default:

- `step_overshoot_f_above_nonburn_core = 0.345`
- `step_overshoot_f_above_burn_h_core = 0.345`

- `step_overshoot_f_above_burn_he_core = 0.345`

- `step_overshoot_f_above_burn_z_core = 0.345`

adjusted:

- `step_overshoot_f_above_nonburn_core = 0.51`

- `step_overshoot_f_above_burn_h_core = 0.51`

- `step_overshoot_f_above_burn_he_core = 0.51`

- `step_overshoot_f_above_burn_z_core = 0.51`

Grid 3a

default:

- `Dutch_scaling_factor = 1.0`

adjusted:

- `Dutch_scaling_factor = 0.4`

Grid 3b

default:

- `Dutch_scaling_factor = 1.0`

- `x_ctrl(20) = -1`

adjusted:

- `Dutch_scaling_factor = 0.4`

- `x_ctrl(20) = 20d3`

Grid 3c

default:

- `Vink_scaling_factor = 1.0`

- `x_ctrl(20) = -1`

adjusted:

- `Vink_scaling_factor = 0.4`

- `x_ctrl(20) = 20d3`

Grid 3d

default:

- `Vink_scaling_factor = 1.0`
- `x_ctrl(20) = -1`
- `x_ctrl(21) = 0`

adjusted:

- `Vink_scaling_factor = 0.4`
- `x_ctrl(20) = 20d3`
- `x_ctrl(21) = 0.7`

A.4.5 Adjustments for Avoiding Problems

As discussed in Sec. 4.3, we sometimes had to change the settings to avoid problems.

A first step was to comment out the following lines:

- `delta_lg_XH_cntr_max = 0.0`
- `delta_lg_XH_cntr_min = -6.0`
- `delta_lg_XH_cntr_limit = 0.01d0`
- `delta_lg_XHe_cntr_max = 0.0`
- `delta_lg_XHe_cntr_min = -6.0`
- `delta_lg_XHe_cntr_limit = 0.01d0`
- `delta_lg_XC_cntr_max = 0.0d0`
- `delta_lg_XC_cntr_min = -6.0d0`
- `delta_lg_XC_cntr_limit = 0.01d0`

As a second possibility, we adjusted the MLT option from

- `MLT_option = 'Mihalas'`

to

- `MLT_option = 'ML1'`

Finally, we could adjust the MLT++ settings by commenting out

- `gradT_excess_max_change = 0.001`

A.5 Mass Loss

A.5.1 Hooks

MESA offers the possibility to use hooks to manipulate the program without the need of manipulating and compiling the whole code. They can be introduced at different parts during the evolution. All hooks are defined in the file `run_star_extras.f90`, and have to be compiled¹¹ once before the program execution.

A main part of this thesis was to manipulate the wind routine, which we did using a hook. It is based on the Dutch wind scheme, however we introduced more free parameters:

- The `Vink_scaling_factor` is now also available when the Dutch scheme is applied.
- `x_ctrl(20)` adjusts the temperature (in K) of the first jump. If it is ≤ 0 , the jump-temperature is calculated using Eqn. 2.87.
- `x_ctrl(21)` is the exponent α for the metallicity scaling $\sim (Z/Z_{\odot})^{\alpha}$ of the de Jager, Nieuwenhuijzen, and van der Hucht (1988) rates.

In the early phases of our work, we also created other hooks, for debugging and as workarounds for some problems we have been able to fix later on. All hooks except the modified wind were deactivated in the final calculations (compare also the provided inlists).

A.5.2 Implicit Mass Loss at Critical Rotation

For many models at low metallicity that evolve close to critical rotation, we found that the implicit mass loss was the best solution to keep the rotation subcritical.

¹¹Using the commands `clean` and `mk`

If the rotation exceeds a specific value `surf_w_div_w_crit_limit`, the implicit mass loss is applied.

It increases the mass loss by `mdot_revise_factor`, until a value slightly smaller than the above limit for the rotational speed is reached. It saves the last values of \dot{M} , when the rotation has been critical (subcritical) as \dot{M}_{small} (\dot{M}_{large}), and checks if they lie within the tolerance

$$\left| \frac{\dot{M}_{large} - \dot{M}_{small}}{\dot{M}_{large}} \right| < tol, \quad (\text{A.1})$$

with tolerance defined by the parameter `surf_w_div_w_crit_tol`.

If the difference is larger than the tolerance, bisections are performed, until the value lies within the tolerance. If

$$\Omega < \Omega_{limit} \quad (\text{A.2})$$

$$\wedge \left| \frac{\dot{M} - \dot{M}_{small}}{\dot{M}} \right| < tol \quad (\text{A.3})$$

the mass loss \dot{M} is applied.

The sum of mass loss increases and bisections must not exceed `max_mdot_redo_cnt`, otherwise the calculation is retried with smaller timesteps.

However, this condition can lead to severe problems if used in combination with the general implicit wind (`max_tries_for_implicit_wind` \neq 0). The general implicit wind alters the mass loss rate, already before the first change due to critical rotation. It is not the explicit value any longer. As the conditions for terminating the routine and not modifying the mass loss are different, this might lead to a problematic situation, if the general implicit wind is slightly lower than the explicit value, and thus the rotation rate too high:

1. The general implicit wind returns a value $\dot{M} \neq M_{explicit}$, but $\Omega < \Omega_{limit}$
2. As $\Omega < \Omega_{limit}$, $\dot{M}_{large} = \dot{M}$ is set.
3. As $\dot{M} \neq M_{explicit}$, the implicit mass loss for critical rotation alters \dot{M} . It retains the explicit mass loss $\dot{M} = \dot{M}_{explicit}$. However, this adjustment causes $\Omega > \Omega_{limit}$, and $\dot{M}_{small} = \dot{M}$ is set.
4. The implicit wind for critical rotation is again calculated.

5. By coincidence, condition (A.1) is fulfilled. In the following steps, the wind is not adjusted. As the wind is not adjusted, Ω stays larger than Ω_{limit} . Condition (A.2) thus cannot be fulfilled, and the calculations continues.
6. In all the following tries, the situation does not change.
7. After the maximum of tries, MESA retries with a smaller timestep.

In some cases, several retries occur, finally causing too small timesteps. The simplest way to avoid this behaviour is to force the wind calculation to start with the explicit value.

General implicit wind must not be used together with implicit rotational enhancement!

A.6 Runtime analysis

MESA is partly multi-threaded as described by Paxton et al. (2011, their section 6.8) and Paxton et al. (2013, their section B.9). It uses algorithms that are thread-safe, such that the results are independent of the number of threads used. We expect that the runtime decreases roughly linear (in log-log space) for increasing number of threads assigned to the execution. The number of threads can be set by using the system variable `OMP_NUM_THREADS`.

To obtain an impression of the optimum number of threads, we performed an analysis of models with different masses and rotational velocities. From the rotating $60M_{\odot}$ model shown in Fig. A.1, we can derive an optimum thread number of 16. The trend is similar, independent of the rotational velocity and the initial mass.

The runtime decreases by a factor of 2 for every increase of the number of threads by a factor of 3 to 10. Different evolutionary stages lead to different slopes. Especially, the pre MS seems to be more efficient using synchronisation than later evolutionary stages. Compared to Paxton et al. (2013), the decrease in runtime is on the same order of magnitude, but slightly less steep. This can be explained by the different MESA version, differences in the specific models, and different hardware.

The runtime decreases for up to 16 threads, which is the number we finally used for all later runs. For even more threads, this trend reverses and the runtime increases again. This can be explained by bottlenecks in memory, reading, and

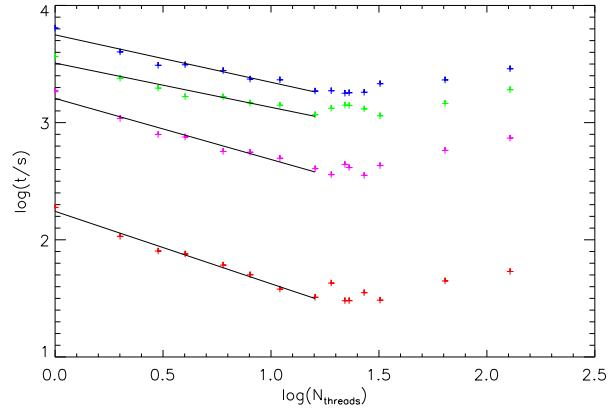


Figure A.1: Runtime analysis for a rotating ($\Omega = 0.4\Omega_{crit}$) $60M_{\odot}$ model. The four different phases: **pre MS**, **MS**, **until central He exhaustion**, and **until central C exhaustion** are shown. The slope was calculated by a fit for up to 16 threads and varies between -0.37 and -0.62 , depending on the evolutionary stage.

writing. Non-efficient synchronisation could be another issue. More detailed studies would be required to find the exact reason.

B IDL

B.1 Analysis of a Single Model

Before analysing the data, we convert them into IDL structures. This drastically simplifies the following analysis, and accelerates the execution. The conversion consists of two steps

- `read_all_mesa` reads all data from the model and profile files.
- `find_zones` calculates additional properties. Especially, it defines the (connected) zones for different mixing processes and burning strengths relevant for the Kippenhahn diagram, but also specific times, such as the ZAMS or the beginning of different burning stages.

These routines are based on the work of K. Zaidi (a summer student in the working-group of J. Puls).

Together with Ferraro (2020), we programmed many routines to create specific diagrams. The most important ones are

- `abundance_evolution(_multi_linear)` creates a plot displaying the evolution of central and surface abundances. The `_multi_linear` version has different time axes for different evolutionary phases.
- `hrd` creates a Hertzsprung-Russel-diagram.
- `kippenhahn(_multi_linear)`: creates a Kippenhahn diagram.

In addition, we prepared debugging routines for several parameters, such as Γ_e , \dot{M} , and v_{rot} . To simplify plotting of specific parameters, Ferraro (2020) prepared `hpp` and `ppp`.

For the analysis of specific models and comparisons presented in the thesis, we programmed routines only designed for this specific purpose.

B.2 Grid Analysis

To speed up the analysis of the different grids, we read the most important data into a new IDL structure. It is split into progenitor properties, and the main evolutionary data:

- `grid_analysis`
- `grid_analysis_evolution`

For the analysis, we prepared several routines to create specific diagrams:

- `comp_hrds`: HRD comparing the evolution of all models,
- `core_and_final_masses`: effect of specific parameters on core and final masses,
- `all_remnants`: comparison of remnant masses,
- `heger2003`: plots similar to those of Heger et al. (2003) displaying the remnant or explosion type depending on metallicity and initial mass,
- `all_remnants_mrem_div_mstar`: plot of M_{rem}/M_{star} , relevant for microlensing.

Bibliography

- Abbott, B. P., et al. 2017. “GW170817: Observation of Gravitational Waves from a Binary Neutron Star Inspiral”. *Phys.Rev.L* 119, no. 16, 161101 (): 161101.
- Abbott, B. P., et al. 2016. “Observation of Gravitational Waves from a Binary Black Hole Merger”. *Phys.Rev.L* 116, no. 6, 061102 (): 061102.
- Aerts, C. 2019. “Probing the interior physics of stars through asteroseismology”. Preprint.
- Alecian, E., et al. 2019. “Fossil magnetic fields in intermediate-mass and massive stars”. In *EAS Publications Series*, 82:345–355. EAS Publications Series.
- Asplund, M., N. Grevesse, and A. J. Sauval. 2005. “The Solar Chemical Composition”. In *Cosmic Abundances as Records of Stellar Evolution and Nucleosynthesis*, ed. by III Barnes Thomas G. and Frank N. Bash, 336:25. Astronomical Society of the Pacific Conference Series.
- Asplund, Martin, et al. 2009. “The Chemical Composition of the Sun”. *ARAA* 47, no. 1 (): 481–522.
- Bagnulo, S., et al. 2020. “A search for strong magnetic fields in massive and very massive stars in the Magellanic Clouds”. *A&A* 635, A163 (): A163.
- Ballero, S. K., P. Kroupa, and F. Matteucci. 2007. “Testing the universal stellar IMF on the metallicity distribution in the bulges of the Milky Way and M 31”. *A&A* 467, no. 1 (): 117–121.
- Belczynski, Krzysztof, et al. 2008. “Compact Object Modeling with the StarTrack Population Synthesis Code”. *ApJS* 174, no. 1 (): 223–260.
- Belczynski, Krzysztof, et al. 2010. “On the Maximum Mass of Stellar Black Holes”. *ApJ* 714, no. 2 (): 1217–1226.

-
- Björklund, R., et al. 2020. “New predictions for radiation-driven, steady-state mass-loss and wind-momentum from hot, massive stars II. A grid of O-type stars in the Galaxy and the Magellanic Clouds”. *arXiv e-prints*, arXiv:2008.06066 (): arXiv:2008.06066.
- Bjorkman, J. E., and J. P. Cassinelli. 1993. “Equatorial Disk Formation around Rotating Stars Due to Ram Pressure Confinement by the Stellar Wind”. *ApJ* 409 (): 429.
- Böhm-Vitense, E. 1958. “Über die Wasserstoffkonvektionszone in Sternen verschiedener Effektivtemperaturen und Leuchtkräfte. Mit 5 Textabbildungen”. *ZfA* 46 (): 108.
- Braithwaite, Jonathan, and Henk C. Spruit. 2017. “Magnetic fields in non-convective regions of stars”. *Royal Society Open Science* 4, no. 2, 160271 (): 160271.
- Bressan, Alessandro, et al. 2012. “PARSEC: stellar tracks and isochrones with the PAdova and TRieste Stellar Evolution Code”. *MNRAS* 427, no. 1 (): 127–145.
- Bromm, Volker, Rolf P. Kudritzki, and Abraham Loeb. 2001. “Generic Spectrum and Ionization Efficiency of a Heavy Initial Mass Function for the First Stars”. *ApJ* 552, no. 2 (): 464–472.
- Brott, I., et al. 2011. “Rotating massive main-sequence stars. I. Grids of evolutionary models and isochrones”. *A&A* 530, A115 (): A115.
- Buchler, J. R., and W. R. Yueh. 1976. “Compton scattering opacities in a partially degenerate electron plasma at high temperatures”. *ApJ* 210 (): 440–446.
- Cantiello, Matteo, and Jonathan Braithwaite. 2019. “Envelope Convection, Surface Magnetism, and Spots in A and Late B-type Stars”. *ApJ* 883, no. 1, 106 (): 106.
- Cassisi, S., et al. 2007. “Updated Electron-Conduction Opacities: The Impact on Low-Mass Stellar Models”. *ApJ* 661 (): 1094–1104.
- Castor, J. I., D. C. Abbott, and R. I. Klein. 1975. “Radiation-driven winds in Of stars.” *ApJ* 195 (): 157–174.
- Castor, John L. 1974. “On the force associated with absorption of spectral line radiation”. *MNRAS* 169 (): 279–306.
- Castro, N., et al. 2014. “The spectroscopic Hertzsprung-Russell diagram of Galactic massive stars”. *A&A* 570, L13 (): L13.

- Chaboyer, B., and J. -P. Zahn. 1992. “Effect of horizontal turbulent diffusion on transport by meridional circulation.” *A&A* 253 (): 173–177.
- Chamel, N., et al. 2013. “On the maximum mass of Neutron Stars”. *International Journal of Modern Physics E* 22, no. 07 (): 1330018.
- Chandrasekhar, S. 1931. “The Maximum Mass of Ideal White Dwarfs”. *ApJ* 74 (): 81.
- Chandrasekhar, Subrahmanyan. 1961. *Hydrodynamic and hydromagnetic stability*.
- Charbonnel, Corinne, and Suzanne Talon. 2005. “Influence of Gravity Waves on the Internal Rotation and Li Abundance of Solar-Type Stars”. *Science* 309, no. 5744 (): 2189–2191.
- Chatzopoulos, E., and J. Craig Wheeler. 2012. “Effects of Rotation on the Minimum Mass of Primordial Progenitors of Pair-instability Supernovae”. *ApJ* 748, no. 1, 42 (): 42.
- Chen, Ke-6g, Alexander Heger, and Ann S. Almgren. 2013. “Numerical approaches for multidimensional simulations of stellar explosions”. *Astronomy and Computing* 3 (): 70–78.
- Chen, Yang, et al. 2014. “Improving PARSEC models for very low mass stars”. *MNRAS* 444, no. 3 (): 2525–2543.
- Choi, Jieun, et al. 2016. “Mesa Isochrones and Stellar Tracks (MIST). I. Solar-scaled Models”. *ApJ* 823, no. 2, 102 (): 102.
- Chugunov, A. I., H. E. Dewitt, and D. G. Yakovlev. 2007. “Coulomb tunneling for fusion reactions in dense matter: Path integral MonteCarlo versus mean field”. *Phys.Rev.D* 76, no. 2, 025028 (): 025028.
- Claret, Antonio, and Guillermo Torres. 2019. “The Dependence of Convective Core Overshooting on Stellar Mass: Reality Check and Additional Evidence”. *ApJ* 876, no. 2, 134 (): 134.
- Cohen, Martin. 1988. *In darkness born. The story of star formation*.
- Cox, J. P., and R. T. Giuli. 1968. *Principles of stellar structure Vol. 2 - Applications to Stars*.
- Crowther, Paul A. 2008. “Properties of Wolf-Rayet Stars”. In *Massive Stars as Cosmic Engines*, ed. by F. Bresolin, P. A. Crowther, and J. Puls, 250:47–62. IAU Symposium.

- Cyburt, R. H., et al. 2010. “The JINA REACLIB Database: Its Recent Updates and Impact on Type-I X-ray Bursts”. *ApJS* 189 (): 240–252.
- de Jager, C., H. Nieuwenhuijzen, and K. A. van der Hucht. 1988. “Mass loss rates in the Hertzsprung-Russell diagram.” *A&AS* 72 (): 259–289.
- de Koter, A. 2008. “Observational Constraints on Mass Loss and Evolution of Massive Stars”. In *Mass Loss from Stars and the Evolution of Stellar Clusters*, ed. by A. de Koter, L. J. Smith, and Laurens B. F. M. Waters, 388:87. Astronomical Society of the Pacific Conference Series.
- Denissenkov, Pavel A., and Marc Pinsonneault. 2007. “A Revised Prescription for the Tayler-Spruit Dynamo: Magnetic Angular Momentum Transport in Stars”. *ApJ* 655, no. 2 (): 1157–1165.
- Dominik, C. 1990. “Dust Driven Mass Lost in the HRD.” *Reviews in Modern Astronomy* 3 (): 199–208.
- ud-Doula, Asif, and Stanley P. Owocki. 2002. “Dynamical Simulations of Magnetically Channeled Line-driven Stellar Winds. I. Isothermal, Nonrotating, Radially Driven Flow”. *ApJ* 576, no. 1 (): 413–428.
- ud-Doula, Asif, Stanley P. Owocki, and Richard H. D. Townsend. 2008. “Dynamical simulations of magnetically channelled line-driven stellar winds - II. The effects of field-aligned rotation”. *MNRAS* 385, no. 1 (): 97–108.
- . 2009. “Dynamical simulations of magnetically channelled line-driven stellar winds - III. Angular momentum loss and rotational spin-down”. *MNRAS* 392, no. 3 (): 1022–1033.
- Duncan, Robert C., and Christopher Thompson. 1992. “Formation of Very Strongly Magnetized Neutron Stars: Implications for Gamma-Ray Bursts”. *ApJL* 392 (): L9.
- Eddington, A. S. 1926. *The Internal Constitution of the Stars*.
- Eggenberger, P., A. Maeder, and G. Meynet. 2005. “Stellar evolution with rotation and magnetic fields. IV. The solar rotation profile”. *A&A* 440, no. 1 (): L9–L12.
- Ekström, S., et al. 2012. “Grids of stellar models with rotation. I. Models from 0.8 to 120 M_{\odot} at solar metallicity ($Z = 0.014$)”. *A&A* 537, A146 (): A146.
- Ekström, S., et al. 2020. “Open problems in high-mass stellar evolution”. In *Proceedings of the conference Stars and their Variability Observed from Space*, ed. by C. Neiner et al., 223–228.

- Eldridge, J. J., and J. S. Vink. 2006. “Implications of the metallicity dependence of Wolf-Rayet winds”. *A&A* 452, no. 1 (): 295–301.
- Esquivel, A., and A. C. Raga. 2007. “Radiation-driven collapse of autogravitating neutral clumps”. *MNRAS* 377, no. 1 (): 383–390.
- Euler, M. 1757. “Principes généraux du mouvement des fluides”. <http://eulerarchive.maa.org/docs/originals/E226.pdf>, *Mémoires de l'académie des sciences de Berlin* 11: 274–315.
- Farrell, Eoin J., et al. 2020. “The uncertain masses of progenitors of core-collapse supernovae and direct-collapse black holes”. *MNRAS* 494, no. 1 (): L53–L58.
- Feldmeier, A. 1993. “Zeitabhängige Struktur und Energietransfer der Winde heißer, massereicher Sterne”. PhD thesis, Ludwig-Maximilians-Universität.
- Ferguson, J. W., et al. 2005. “Low-Temperature Opacities”. *ApJ* 623 (): 585–596.
- Ferrario, Lilia, and D. T. Wickramasinghe. 2005. “Magnetic fields and rotation in white dwarfs and neutron stars”. *MNRAS* 356, no. 2 (): 615–620.
- Ferrario, Lilia, et al. 2009. “The origin of magnetism on the upper main sequence”. *MNRAS* 400, no. 1 (): L71–L74.
- Ferraro, Alex. 2020. “Massive Binary evolution with MESA: Interactions on the Main Sequence”. MA thesis, LMU München.
- Fields, C. E., and S. M. Couch. 2020. “On The Development of Multidimensional Progenitor Models For Core-collapse Supernovae”. *arXiv e-prints*, arXiv:2008.04266 (): arXiv:2008.04266.
- Fricke, K. 1968. “Instabilität stationärer Rotation in Sternen”. *ZfA* 68 (): 317.
- Friend, David B., and David C. Abbott. 1986. “The Theory of Radiatively Driven Stellar Winds. III. Wind Models with Finite Disk Correction and Rotation”. *ApJ* 311 (): 701.
- Fuller, G. M., W. A. Fowler, and M. J. Newman. 1985. “Stellar weak interaction rates for intermediate-mass nuclei. IV - Interpolation procedures for rapidly varying lepton capture rates using effective log (ft)-values”. *ApJ* 293 (): 1–16.
- Gagnier, D., et al. 2019. “Critical angular velocity and anisotropic mass loss of rotating stars with radiation-driven winds”. *A&A* 625, A88 (): A88.
- Girart, Josep M., et al. 2009. “Magnetic Fields in the Formation of Massive Stars”. *Science* 324 (5933): 1408–1411.

-
- Glebbeek, E., et al. 2009. “The evolution of runaway stellar collision products”. *A&A* 497, no. 1 (): 255–264.
- Goldreich, Peter, and Gerald Schubert. 1967. “Differential Rotation in Stars”. *ApJ* 150 (): 571.
- Green, Anne M. 2016. “Microlensing and dynamical constraints on primordial black hole dark matter with an extended mass function”. *Phys.Rev.D* 94, no. 6, 063530 (): 063530.
- Groh, J. H., et al. 2019. “Grids of stellar models with rotation. IV. Models from 1.7 to 120 M_{\odot} at a metallicity $Z = 0.0004$ ”. *A&A* 627, A24 (): A24.
- Groh, Jose H., et al. 2014. “The evolution of massive stars and their spectra - I. A non-rotating 60 M_{\odot} star from the zero-age main sequence to the pre-supernova stage”. *A&A* 564:A30.
- Grunhut, J. H., G. A. Wade, and MiMeS Collaboration. 2012. “The incidence of magnetic fields in massive stars: An overview of the MiMeS survey component”. *A&A* 547:A10.
- Hale, George E. 1908. “On the Probable Existence of a Magnetic Field in Sun-Spots”. *ApJ* 28 (): 315.
- Heger, A., N. Langer, and S. E. Woosley. 2000. “Presupernova Evolution of Rotating Massive Stars. I. Numerical Method and Evolution of the Internal Stellar Structure”. *ApJ* 528, no. 1 (): 368–396.
- Heger, A., and S. E. Woosley. 2002. “The Nucleosynthetic Signature of Population III”. *ApJ* 567, no. 1 (): 532–543.
- Heger, A., S. E. Woosley, and H. C. Spruit. 2005. “Presupernova Evolution of Differentially Rotating Massive Stars Including Magnetic Fields”. *ApJ* 626, no. 1 (): 350–363.
- Heger, A., et al. 2003. “How Massive Single Stars End Their Life”. *ApJ* 591, no. 1 (): 288–300.
- Higgins, Erin R., and Jorick S. Vink. 2020. “A theoretical investigation of the Humphreys-Davidson limit at high and low metallicity”. *arXiv e-prints*, arXiv:2002.07204 (): arXiv:2002.07204.
- Hirschi, R., A. Maeder, and G. Meynet. 2004. “Dynamical Shear Instability”. In *Stellar Rotation*, ed. by Andre Maeder and Philippe Eenens, 215:510. IAU Symposium.

- Huang, W., and D. R. Gies. 2006. “Stellar Rotation in Young Clusters. I. Evolution of Projected Rotational Velocity Distributions”. *ApJ* 648, no. 1 (): 580–590.
- Hubrig, S. 2008. “Magnetic fields in massive stars”. In *Revista Mexicana de Astronomia y Astrofisica Conference Series*, 33:26–28. *Revista Mexicana de Astronomia y Astrofisica Conference Series*.
- Humphreys, Roberta M., and Kris Davidson. 1994. “The Luminous Blue Variables: Astrophysical Geysers”. *PASP* 106 (): 1025.
- Iglesias, C. A., and F. J. Rogers. 1993. “Radiative opacities for carbon- and oxygen-rich mixtures”. *ApJ* 412 (): 752–760.
- . 1996. “Updated Opal Opacities”. *ApJ* 464 (): 943.
- Itoh, N., et al. 1996. “Neutrino Energy Loss in Stellar Interiors. VII. Pair, Photo-, Plasma, Bremsstrahlung, and Recombination Neutrino Processes”. *ApJS* 102 (): 411.
- Josselin, E., and B. Plez. 2007. “Atmospheric dynamics and the mass loss process in red supergiant stars”. *A&A* 469, no. 2 (): 671–680.
- Kaiser, Etienne A., et al. 2020. “Relative Importance of Convective Uncertainties in Massive Stars”. *MNRAS* ().
- Keszthelyi, Zsolt. 2015. “The Impact of Mass Loss on the Early Evolution of Massive Stars”. M.Sc. Thesis, LMU München.
- Keszthelyi, Z., et al. 2020. “The effects of surface fossil magnetic fields on massive star evolution - II. Implementation of magnetic braking in MESA and implications for the evolution of surface rotation in OB stars”. *MNRAS* 493, no. 1 (): 518–535.
- Kippenhahn, R. 1974. “Circulation and Mixing”. In *Late Stages of Stellar Evolution*, ed. by R. J. Tayler and J. E. Hesser, 66:20. IAU Symposium.
- Kippenhahn, R., G. Ruschenplatt, and H. -C. Thomas. 1980. “The time scale of thermohaline mixing in stars”. *A&A* 91, no. 1 (): 175–180.
- Kippenhahn, R., and H. -C. Thomas. 1970. “A Simple Method for the Solution of the Stellar Structure Equations Including Rotation and Tidal Forces”. In *IAU Colloq. 4: Stellar Rotation*, ed. by Arne Slettebak, 20.
- Kippenhahn, Rudolf, Alfred Weigert, and Achim Weiss. 2012. *Stellar Structure and Evolution*.

-
- Köhler, K., et al. 2015. “The evolution of rotating very massive stars with LMC composition”. *A&A* 573, A71 (): A71.
- Kroupa, Pavel. 2002. “The Initial Mass Function of Stars: Evidence for Uniformity in Variable Systems”. *Science* 295, no. 5552 (): 82–91.
- Lamers, Henny J. G. L. M., Theodore P. Snow, and Douglas M. Lindholm. 1995. “Terminal Velocities and the Bistability of Stellar Winds”. *ApJ* 455 (): 269.
- Landau, L. D., and E. M. Lifshitz. 1987. *Fluid Mechanics*. 2nd English Edition. Vol. 6. Pergamon Press.
- Langanke, K., and G. Martínez-Pinedo. 2000. “Shell-model calculations of stellar weak interaction rates: II. Weak rates for nuclei in the mass range $A = 45 - 65$ in supernovae environments”. *Nuclear Physics A* 673 (): 481–508.
- Langer, N. 1998. “Coupled mass and angular momentum loss of massive main sequence stars”. *A&A* 329 (): 551–558.
- Langer, N., M. F. El Eid, and K. J. Fricke. 1985. “Evolution of massive stars with semiconvective diffusion”. *A&A* 145, no. 1 (): 179–191.
- Langer, N., K. J. Fricke, and D. Sugimoto. 1983. “Semiconvective diffusion and energy transport”. *A&A* 126, no. 1 (): 207.
- Lee, C. -H., et al. 2015. “Microlensing events from the 11-year Observations of the Wendelstein Calar Alto Pixellensing Project”. *ApJ* 806, no. 2, 161 (): 161.
- Leitherer, Claus, Carmelle Robert, and Laurent Drissen. 1992. “Deposition of Mass, Momentum, and Energy by Massive Stars into the Interstellar Medium”. *ApJ* 401 (): 596.
- Levesque, Emily M., et al. 2005. “The Effective Temperature Scale of Galactic Red Supergiants: Cool, but Not As Cool As We Thought”. *ApJ* 628, no. 2 (): 973–985.
- Levesque, Emily M., et al. 2006. “The Effective Temperatures and Physical Properties of Magellanic Cloud Red Supergiants: The Effects of Metallicity”. *ApJ* 645, no. 2 (): 1102–1117.
- Li, Yan, Xing-hao Chen, and Hai-liang Chen. 2019. “Overshooting in the Core Helium-burning Stage of a $30 M_{\odot}$ Star Using the $k\text{-}\omega$ Model”. *ApJ* 870, no. 2, 77 (): 77.

- Liu, Junhao, et al. 2020. “Magnetic Fields in the Early Stages of Massive Star Formation as Revealed by ALMA”. *The Astrophysical Journal* 895, no. 2 (): 142.
- Lucy, L. B., and P. M. Solomon. 1970. “Mass Loss by Hot Stars”. *ApJ* 159 (): 879.
- MacDonald, James, and D. J. Mullan. 2004. “Magnetic fields in massive stars: dynamics and origin”. *Monthly Notices of the Royal Astronomical Society* 348, no. 2 (): 702–716.
- Maeder, A., and G. Meynet. 2003. “Stellar evolution with rotation and magnetic fields. I. The relative importance of rotational and magnetic effects”. *A&A* 411 (): 543–552.
- . 2004. “Stellar evolution with rotation and magnetic fields. II. General equations for the transport by Tayler-Spruit dynamo”. *A&A* 422 (): 225–237.
- . 2005. “Stellar evolution with rotation and magnetic fields. III. The interplay of circulation and dynamo”. *A&A* 440, no. 3 (): 1041–1049.
- . 2000. “Stellar evolution with rotation. VI. The Eddington and Omega -limits, the rotational mass loss for OB and LBV stars”. *A&A* 361 (): 159–166.
- Maeder, André. 2009. *Physics, Formation and Evolution of Rotating Stars*. Springer, Berlin, Heidelberg.
- Marigo, Paola, et al. 2017. “A New Generation of PARSEC-COLIBRI Stellar Isochrones Including the TP-AGB Phase”. *ApJ* 835, no. 1, 77 (): 77.
- Markova, N., and J. Puls. 2008. “Bright OB stars in the Galaxy. IV. Stellar and wind parameters of early to late B supergiants”. *A&A* 478, no. 3 (): 823–842.
- Martins, F., and A. Palacios. 2013. “A comparison of evolutionary tracks for single Galactic massive stars”. *A&A* 560, A16 (): A16.
- Massey, Philip, and Kate Anne Evans. 2016. “The Red Supergiant Content of M31*”. *ApJ* 826, no. 2, 224 (): 224.
- Massey, Philip, and K. A. G. Olsen. 2003. “The Evolution of Massive Stars. I. Red Supergiants in the Magellanic Clouds”. *AJ* 126, no. 6 (): 2867–2886.
- Matteucci, F., and A. Tornambe. 1987. “Chemical evolution of elliptical galaxies”. *A&A* 185, no. 1 (): 51–60.
- Mauron, N., and E. Josselin. 2011. “The mass-loss rates of red supergiants and the de Jager prescription”. *A&A* 526, A156 (): A156.

- Meynet, G., and A. Maeder. 1997. “Stellar evolution with rotation. I. The computational method and the inhibiting effect of the μ -gradient.” *A&A* 321 (): 465–476.
- . 2003. “Stellar evolution with rotation. X. Wolf-Rayet star populations at solar metallicity”. *A&A* 404 (): 975–990.
- Meynet, Georges, and André Maeder. 2017. “Supernovae from Rotating Stars”. In *Handbook of Supernovae*, ed. by Athem W. Alsabti and Paul Murdin, 601.
- Mihalas, Dimitri. 1978. *Stellar atmospheres*.
- Najarro, F., et al. 2008. “Tracking the Clumping in OB Stars from UV to radio”. In *Clumping in Hot-Star Winds*, ed. by Wolf-Rainer Hamann, Achim Feldmeier, and Lidia M. Oskinova, 43.
- Nieuwenhuijzen, H., and C. de Jager. 1990. “Parametrization of stellar rates of mass loss as functions of the fundamental stellar parameters M, L, and R.” *A&A* 231 (): 134–136.
- Nieva, M. -F., and N. Przybilla. 2012. “Present-day cosmic abundances. A comprehensive study of nearby early B-type stars and implications for stellar and Galactic evolution and interstellar dust models”. *A&A* 539, A143 (): A143.
- Niikura, Hiroko, et al. 2019. “Microlensing constraints on primordial black holes with Subaru/HSC Andromeda observations”. *Nature Astronomy* 3 (): 524–534.
- Nugis, T., and H. J. G. L. M. Lamers. 2000. “Mass-loss rates of Wolf-Rayet stars as a function of stellar parameters”. *A&A* 360 (): 227–244.
- Oda, T., et al. 1994. “Rate Tables for the Weak Processes of sd-Shell Nuclei in Stellar Matter”. *Atomic Data and Nuclear Data Tables* 56 (): 231–403.
- Owocki, S. P., J. I. Castor, and G. B. Rybicki. 1988. “Time-dependent Models of Radiatively Driven Stellar Winds. I. Nonlinear Evolution of Instabilities for a Pure Absorption Model”. *Astrophysical Journal* 335:914–930.
- Owocki, S. P., S. R. Cranmer, and K. G. Gayley. 1996. “Inhibition FO Wind Compressed Disk Formation by Nonradial Line-Forces in Rotating Hot-Star Winds”. *ApJL* 472 (): L115.
- Palau, A., et al. 2020. “Fragmentation of molecular clouds: the role of magnetic field”. In *Contributions to the XIV.0 Scientific Meeting (virtual) of the Spanish Astronomical Society*, 172.

-
- Pastorelli, Giada, et al. 2020. “Constraining the thermally pulsing asymptotic giant branch phase with resolved stellar populations in the Large Magellanic Cloud”. *MNRAS* 498, no. 3 (): 3283–3301.
- Pastorelli, Giada, et al. 2019. “Constraining the thermally pulsing asymptotic giant branch phase with resolved stellar populations in the Small Magellanic Cloud”. *MNRAS* 485, no. 4 (): 5666–5692.
- Pauldrach, A. W. A., and J. Puls. 1990. “Radiation-driven winds of hot luminous stars. VIII. The bistable wind of the luminous blue variable P Cygni (B1 Ia+).” *A&A* 237 (): 409.
- Pauldrach, A., J. Puls, and R. P. Kudritzki. 1986. “Radiation-driven winds of hot luminous stars. Improvements of the theory and first results.” *A&A* 164 (): 86–100.
- Paxton, Bill, et al. 2019. “Modules for Experiments in Stellar Astrophysics (MESA): Pulsating Variable Stars, Rotation, Convective Boundaries, and Energy Conservation”. *ApJS* 243, no. 1, 10 (): 10.
- Paxton, B., et al. 2011. “Modules for Experiments in Stellar Astrophysics (MESA)”. *ApJS* 192, 3 (): 3.
- Paxton, B., et al. 2015. “Modules for Experiments in Stellar Astrophysics (MESA): Binaries, Pulsations, and Explosions”. *ApJS* 220, 15 (): 15.
- Paxton, B., et al. 2018. “Modules for Experiments in Stellar Astrophysics (MESA): Convective Boundaries, Element Diffusion, and Massive Star Explosions”. *ApJS* 234, 34 (): 34.
- Paxton, B., et al. 2013. “Modules for Experiments in Stellar Astrophysics (MESA): Planets, Oscillations, Rotation, and Massive Stars”. *ApJS* 208, 4 (): 4.
- Petit, V., et al. 2017. “Magnetic massive stars as progenitors of ‘heavy’ stellar-mass black holes”. *MNRAS* 466, no. 1 (): 1052–1060.
- Petit, V., et al. 2012. “Magnetospheres of Massive Stars Across the EM Spectrum”. In *Proceedings of a Scientific Meeting in Honor of Anthony F. J. Moffat*, ed. by L. Drissen et al., 465:48. Astronomical Society of the Pacific Conference Series.
- Petrov, Blagovest, Jorick S. Vink, and Götz Gräfenor. 2014. “On the H α behaviour of blue supergiants: rise and fall over the bi-stability jump”. *A&A* 565, A62 (): A62.

-
- . 2016. “Two bi-stability jumps in theoretical wind models for massive stars and the implications for luminous blue variable supernovae”. *MNRAS* 458, no. 2 (): 1999–2011.
- Petrovic, J., et al. 2005. “Which massive stars are gamma-ray burst progenitors?” *A&A* 435, no. 1 (): 247–259.
- Pols, O. R., et al. 1995. “Approximate input physics for stellar modelling”. *MNRAS* 274 (): 964–974.
- Poniatowski, L.G., et al. 2012. “Wind models of dynamically inflated classical Wolf-Rayet stars”. Preprint.
- Potekhin, A. Y., and G. Chabrier. 2010. “Thermodynamic Functions of Dense Plasmas: Analytic Approximations for Astrophysical Applications”. *Contributions to Plasma Physics* 50 (): 82–87.
- Prandtl, L. 1925. “7. Bericht über Untersuchungen zur ausgebildeten Turbulenz”. *Zeitschrift Angewandte Mathematik und Mechanik* 5, no. 2 (): 136–139.
- Przybilla, N., et al. 2013. “Hot stars and cosmic abundances”. In *EAS Publications Series*, ed. by G. Alecian et al., 63:13–23. EAS Publications Series.
- Puls, J., U. Springmann, and M. Lennon. 2000. “Radiation driven winds of hot luminous stars. XIV. Line statistics and radiative driving”. *A&AS* 141 (): 23–64.
- Puls, Joachim, Jorick S. Vink, and Francisco Najarro. 2008. “Mass loss from hot massive stars”. *A&A Rev.* 16, no. 3 (): 209–325.
- Reimers, D. 1975. “Circumstellar absorption lines and mass loss from red giants.” *Memoires of the Societe Royale des Sciences de Liege* 8 (): 369–382.
- . 1977. “On the absolute scale of mass-loss in red giants. I. Circumstellar absorption lines in the spectrum of the visual companion of alpha ¹Her.” *A&A* 61 (): 217–224.
- Renzini, Alvio, and Luca Ciotti. 1993. “Transverse Dissections of the Fundamental Planes of Elliptical Galaxies and Clusters of Galaxies”. *ApJL* 416 (): L49.
- Rezzolla, Luciano, Elias R. Most, and Lukas R. Weih. 2018. “Using Gravitational-wave Observations and Quasi-universal Relations to Constrain the Maximum Mass of Neutron Stars”. *The Astrophysical Journal* 852, no. 2 (): L25.
- Riffeser, A., S. Seitz, and R. Bender. 2008. “The M31 Microlensing Event WeCAPP-GL1/POINT-AGAPE-S3: Evidence for a MACHO Component in the Dark Halo of M31?” *ApJ* 684, no. 2 (): 1093–1109.

-
- Riffeser, A., et al. 2006. “Microlensing toward Crowded Fields: Theory and Applications to M31”. *ApJS* 163, no. 2 (): 225–269.
- Rogers, F. J., and A. Nayfonov. 2002. “Updated and Expanded OPAL Equation-of-State Tables: Implications for Helioseismology”. *ApJ* 576, no. 2 (): 1064–1074.
- Saglia, R. P., et al. 2018. “Stellar populations of the central region of M 31”. *A&A* 618, A156 (): A156.
- Saglia, R. P., et al. 2010. “The old and heavy bulge of M 31 . I. Kinematics and stellar populations”. *A&A* 509, A61 (): A61.
- Sakon, Itsuki, et al. 2010. “Dust formation by massive stars studied by infrared observations with AKARI/IRC and Subaru/COMICS”. In *Astronomical Society of India Conference Series*, 1:49–55. Astronomical Society of India Conference Series.
- Salaris, Maurizio, and Santi Cassisi. 2017. “Chemical element transport in stellar evolution models”. *Royal Society Open Science* 4, no. 8, 170192 (): 170192.
- Salpeter, Edwin E. 1955. “The Luminosity Function and Stellar Evolution.” *ApJ* 121 (): 161.
- Sana, H., et al. 2012. “Binary Interaction Dominates the Evolution of Massive Stars”. *Science* 337, no. 6093 (): 444.
- Saumon, D., G. Chabrier, and H. M. van Horn. 1995. “An Equation of State for Low-Mass Stars and Giant Planets”. *ApJS* 99 (): 713.
- Schaerer, D., and A. Maeder. 1992. “Basic relations between physical parameters of Wolf-Rayet stars”. *A&A* 263, no. 1 (): 129–136.
- Schaller, G., et al. 1992. “New grids of stellar models from 0.8 to 120 M_⊙ at Z=0.020 and Z=0.001”. *A&AS* 96 (): 269.
- Schneider, F. R. N., et al. 2020. “Long-term evolution of a magnetic massive merger product”. *MNRAS* 495, no. 3 (): 2796–2812.
- Schneider, Fabian R. N., et al. 2019. “Stellar mergers as the origin of magnetic massive stars”. *Nature* 574, no. 7777 (): 211–214.
- Schootemeijer, A., et al. 2019. “Constraining mixing in massive stars in the Small Magellanic Cloud”. *A&A* 625, A132 (): A132.
- Schröder, K. -P., and M. Cuntz. 2005. “A New Version of Reimers’ Law of Mass Loss Based on a Physical Approach”. *ApJL* 630, no. 1 (): L73–L76.

-
- Sobolev, V. V. 1947. *Moving envelopes of stars*. Leningrad: Leningrad State University (Englische Übersetzung: Cambridge: Harvard University Press, 1960).
- Spera, Mario, Michela Mapelli, and Alessandro Bressan. 2015. “The mass spectrum of compact remnants from the PARSEC stellar evolution tracks”. *MNRAS* 451, no. 4 (): 4086–4103.
- Spruit, H. C. 1999. “Differential rotation and magnetic fields in stellar interiors”. *A&A* 349 (): 189–202.
- . 2006. “Magnetic instability in a differentially rotating star”. *arXiv e-prints*, astro-ph/0607164 (): astro-ph/0607164.
- Stephens, Andrew W., et al. 2003. “The Stellar Content of the Bulge of M31”. *The Astronomical Journal* 125, no. 5 (): 2473–2493.
- Suijs, M. P. L., et al. 2008. “White dwarf spins from low-mass stellar evolution models”. *A&A* 481, no. 3 (): L87–L90.
- Sundqvist, J. O., et al. 2019. “New predictions for radiation-driven, steady-state mass-loss and wind-momentum from hot, massive stars. I. Method and first results”. *A&A* 632, A126 (): A126.
- Sweet, P. A. 1950. “The importance of rotation in stellar evolution”. *MNRAS* 110 (): 548.
- Tang, Jing, et al. 2014. “New PARSEC evolutionary tracks of massive stars at low metallicity: testing canonical stellar evolution in nearby star-forming dwarf galaxies”. *MNRAS* 445, no. 4 (): 4287–4305.
- Thomas, J., et al. 2011. “Dynamical masses of early-type galaxies: a comparison to lensing results and implications for the stellar initial mass function and the distribution of dark matter”. *MNRAS* 415, no. 1 (): 545–562.
- Thompson, Christopher, and Robert C. Duncan. 1995. “The soft gamma repeaters as very strongly magnetized neutron stars - I. Radiative mechanism for outbursts”. *MNRAS* 275, no. 2 (): 255–300.
- Timmes, F. X., and F. Douglas Swesty. 2000. “The Accuracy, Consistency, and Speed of an Electron-Positron Equation of State Based on Table Interpolation of the Helmholtz Free Energy”. *ApJS* 126, no. 2 (): 501–516.
- Timmes, F. X., S. E. Woosley, and Thomas A. Weaver. 1996. “The Neutron Star and Black Hole Initial Mass Function”. *ApJ* 457 (): 834.

- Tremblay, P.-E., et al. 2015. “ON THE EVOLUTION OF MAGNETIC WHITE DWARFS”. *The Astrophysical Journal* 812, no. 1 (): 19.
- Tumlinson, J., J. M. Shull, and A. Venkatesan. 2002. “Cosmological Reionization by the First Stars: Evolving Spectra of Population III”. In *Hot Star Workshop III: The Earliest Phases of Massive Star Birth*, ed. by P. Crowther, 267:433. Astronomical Society of the Pacific Conference Series.
- Turner, David G. 1996. “The Progenitors of Classical Cepheid Variables”. *JRASC* 90 (): 82.
- van Genderen, A. M., and P. S. The. 1984. “Characteristics and Interpretation of the Photometric Variability of Eta-Carinae and its Nebula”. *SSR* 39, no. 3 (): 317–373.
- van Loon, J. Th. 2006. “On the metallicity dependence of the winds from red supergiants and Asymptotic Giant Branch stars”. In *Stellar Evolution at Low Metallicity: Mass Loss, Explosions, Cosmology*, ed. by Henny J. G. L. M. Lamers et al., 353:211. Astronomical Society of the Pacific Conference Series.
- van Loon, J. Th., et al. 2005. “An empirical formula for the mass-loss rates of dust-enshrouded red supergiants and oxygen-rich Asymptotic Giant Branch stars”. *A&A* 438, no. 1 (): 273–289.
- Vink, Jorick S., A. de Koter, and H. J. G. L. M. Lamers. 2001. “Mass-loss predictions for O and B stars as a function of metallicity”. *A&A* 369 (): 574–588.
- Wade, G. A., et al. 2016. “The MiMeS survey of magnetism in massive stars: introduction and overview”. *MNRAS* 456, no. 1 (): 2–22.
- Wade, Gregg A., et al. 2009. “The MiMeS project: magnetism in massive stars”. In *Cosmic Magnetic Fields: From Planets, to Stars and Galaxies*, ed. by Klaus G. Strassmeier, Alexander G. Kosovichev, and John E. Beckman, 259:333–338. IAU Symposium.
- Wade, Gregg A., et al. 2011. “The MiMeS project: overview and current status”. In *Active OB Stars: Structure, Evolution, Mass Loss, and Critical Limits*, ed. by Coralie Neiner et al., 272:118–123. IAU Symposium.
- Wagle, Gururaj A., et al. 2019. “Type IIP Supernova Progenitors and Their Explodability. I. Convective Overshoot, Blue Loops, and Surface Composition”. *ApJ* 886, no. 1, 27 (): 27.
- Wambsganss, Joachim. 2006. “Gravitational Microlensing”. *arXiv e-prints*, astro-ph/0604278 (): astro-ph/0604278.

-
- Woosley, S. E. 2019. “The Evolution of Massive Helium Stars, Including Mass Loss”. *ApJ* 878, no. 1, 49 (): 49.
- Woosley, S. E., A. Heger, and T. A. Weaver. 2002. “The evolution and explosion of massive stars”. *Reviews of Modern Physics* 74, no. 4 (): 1015–1071.
- Woosley, S. E., N. Langer, and T. A. Weaver. 1995. “The Presupernova Evolution and Explosion of Helium Stars That Experience Mass Loss”. *ApJ* 448 (): 315.
- Wu, Tao, and Yan Li. 2019. “High-precision Asteroseismology in a Slowly Pulsating B Star: HD 50230”. *ApJ* 881, no. 1, 86 (): 86.
- Yoshida, Takashi, et al. 2019. “One-, Two-, and Three-dimensional Simulations of Oxygen-shell Burning Just before the Core Collapse of Massive Stars”. *ApJ* 881, no. 1, 16 (): 16.
- Zahn, J. -P. 1992. “Circulation and turbulence in rotating stars.” *A&A* 265 (): 115–132.
- Zahn, J. -P., A. S. Brun, and S. Mathis. 2007. “On magnetic instabilities and dynamo action in stellar radiation zones”. *A&A* 474, no. 1 (): 145–154.
- Zhang, Qizhou. 2020. “Magnetic fields and massive star formation”. In *IAU General Assembly*, 141–141.
- Zoccali, Manuela, et al. 2000. “The Initial Mass Function of the Galactic Bulge down to $\sim 0.15 M_{\text{solar}}$ ”. *ApJ* 530, no. 1 (): 418–428.

Acknowledgements

I owe my greatest gratitude to Jo Puls, for the supervision of this thesis. Thank you for offering the thesis to me, for all the instructive discussions, for all questions, comments and improvements from you. It was a very educational and inspiring time working with you. Your feedback on my scientific work and especially our personal relationship gave me more than I ever could expect from a supervision at university. It was an honour to be your student!

I am also heartily grateful to Arno Riffeser, for being my second supervisor. Your discussions about microlensing and questions to my results throughout the thesis helped me a lot in improving the thesis. Thank you also for the computational time on your machine, that accelerated my calculations in the beginning.

I would like to thank you both, Jo and Arno, for allowing me to go on Wendelstein, and getting an insight into observations and corresponding preparation. It has been a very instructive night up on the mountain, and I really enjoyed the time with all of you.

This thesis wouldn't have been that much fun without Alex Ferraro. Thank you for all the discussions, ideas, and conversations. It has been great working together with you, no matter if next to each other in the same office, or via Zoom. I also want to thank you for the great friendship.

I want also to thank Zsolt Keszthelyi, for enlightening discussions about MESA, and hints about relevant papers.

Also, I have to thank Eva SEXTL for the helpful discussion about MESA and possible pitfalls, such that I could avoid many of them.

I appreciate the interesting conversation with Jon Sundqvist about the necessity of MLT++.

The analysis of the data would have been much more complex, without the good starting point regarding the IDL routines provided by Kumail Zaidi.

The completion of the project always relied on working computers. A special advantage were the new machines, that drastically increased the computational

performance of my model calculations. Thank you Keith Butler, Rudi Gabler, and Tadziu Hoffmann for setting up the new machines, and for keeping the systems running all the time, such that I could run all my simulations.

I would like to offer my special thanks to Bill Paxton and the MESA developers for making MESA available. In addition, the open discussion on the mailing list provided great help for many problems. This thanks has to be extended to all mailing list users.

For the financial, as well as ideal and spiritual support I want to express my sincere thanks to the Cusanuswerk e.V. for granting me their scholarship. This allowed me to focus on my studies, but also to establish new contacts and friendships.

I am also grateful to Alex, Jo, Arno, and Anja Seegebrecht for proofreading my thesis. Thank you for all the constructive feedback that helped to improve my thesis.

Finally, I must express my profound gratitude to my parents Florian and Martina and my sister Johanna. Thank you for all the encouragement and support throughout my studies.

Eidesstattliche Erklärung

Hiermit erkläre ich, die vorliegende Arbeit selbständig verfasst zu haben und keine anderen als die in der Arbeit angegebenen Quellen und Hilfsmittel benutzt zu haben.

München, den 2. November, 2020

Frederick Groth